Hydrodynamics of a Cold Model of a Dual Fluidized Bed Gasification Plant

Mook Tzeng Lim

A thesis submitted in fulfillment of the requirements for the Degree of
Doctor of Philosophy in Chemical and Process Engineering
in the University of Canterbury

Christchurch, New Zealand
February 2012

A Man is the sum of his actions, of what he has done, of what he can do, nothing else.

-Mahatma Gandhi

Contents

List of Figures

List of Tables

Acknowledgements

Thanks to

to my principal supervisor, Professor Shusheng Pang, and co-supervisor Dr. Justin Nijdam, both of the Department of Chemical & Process Engineering;

to Leigh Richardson: without whom the plant will never get built;

to Tim Moore & Glenn Wilson: without whom the project would never progress;

to friends: without whom the after hours would be longer;

to FRST: for funding of this project;

to University of Canterbury: to deem me as qualified for the Doctoral Scholarship;

and not forgetting,

WaiKuan Ho,

my parents & sister back home: *for everything else*.

Abstract

Biomass energy is increasingly used to reduce the dependence on fossil fuels and reduce the impact of greenhouse gas emissions on global warming. Fluidized bed gasification converts solid biomass into gaseous fuels that can be used for combustion or liquid fuels synthesis. The efficiency of biomass gasification is directly affected by the fluidized bed hydrodynamics. For example, the solids recirculation rate through the system is an important parameter that affects the heat and mass transfer rates. In this study, a cold model of a dual fluidized bed (DFB) biomass gasification plant was designed using scaling laws, and was constructed to investigate the hydrodynamics of industrial DFBs. A DFB consists of a bubbling fluidized bed (BFB), where biomass is gasified to produce syngas, and a circulating fluidized bed (CFB) where the residues of gasification are combusted. The investigation was divided into Phase I and II. In Phase I, an operational map was developed for the CFB to define operational boundaries for steady state operation of the plant. An empirical model was developed to predict the solids mass flow rate out of the CFB riser, which is an empirical function of the exit opening width, the CFB diameter, and a newly introduced aerodynamic factor. The correlation coefficient, R^2 for the empirical function was 0.8327. The aerodynamic factor accounts for the particle inertia and clustering effects at the exit of the CFB riser. Results from Phase I also showed that increasing the fluidizing velocities increased the solids circulation rate and affected the pressure drop over various points in the CFB plant due to redistribution of solids with the system. A critical assessment was performed on published correlations found in the literature to determine how accurately they predicted the hydrodynamics in the CFB riser. By comparing predicted and experimental results, the correlations were found to be inaccurate for the conditions and configuration of the CFB tested in this study. For example, the solids velocity was not accurately predicted

by published correlations due to unaccounted particle clustering effects. The main issue with the published correlations was a lack of generality, so that the correlations only applied for predicting fluidizing behaviour in the equipment they were developed in. In Phase II, an operational map was developed for the DFB, which incorporated both the CFB and the BFB. Experiments with a binary mixture representing sand and char in an industrial gasifier showed a blocking effect in the connecting chute between the CFB and BFB by the material representing char, which was larger and less dense than the material representing sand. A computational fluid dynamics (CFD) based design tool for modelling the cold model CFB cyclone was developed and validated by comparing the predicted and experimental cyclone pressure drop. The correlation coefficient for the CFD pressure drop prediction was 0.7755. The design tool contained information about the grid resolution and the time step required for modelling the cyclone accurately.

Nomenclature

ΔP_{br} riser bottom section pressure drop, Pa

ΔP_{CB} CFB-BFB pressure difference, Pa

ΔP_{ch} chute pressure drop, Pa

$\Delta P_{g,acc}$ pressure drop due to gas acceleration

ΔP_{ls} loop-seal pressure drop, Pa

$\Delta P_{s,acc}$ pressure drop due to solids acceleration

$\Delta P_{s,sf}$ pressure drop due to solids-wall frictional forces

ΔP_{ur} riser upper section pressure drop, Pa

$\dot{m}_{core}$ riser solids core flow rate, kg/s

$\dot{m}_{so}$ riser solids outflow rate, kg/s

ε void fraction at a riser height H

ε'_{dz} diluted dense zone voidage

ε'_{sd} diluted solid fraction

ε_s radial averaged solid volume fraction at a riser height H of upward flowing solids

ε_∞ void fraction at an infinite height

ε_{dz} dense zone voidage

ε_{sd} dense zone solid fraction

μ_g gas viscosity, Pas

$\overline{\varepsilon}_{s,core}$ radial-averaged solids fraction of the core at an axial height of 2.55 m up the riser from the air distributor plate

ϕ particle shape factor

Φ_d aerodynamic factor

ρ_g gas density, kg/m^3

ρ_s particle density, kg/m^3

a fitting coefficient

a_d decay constant

Ar Archimedes number

C_D drag coefficient

D diameter of riser, m

d_p particle mean volume diameter, μm

D_{ba} cyclone scroll or barrel diameter, m

D_c cyclone diameter, m

d_{eff} effective particle diameter, μm

D_{ex} cyclone gas exit diameter, m

D_{vf} vortex finder diameter, m

De density ratio

f_s solid friction factor

Fl flow number

G^* dimensionless solids circulation

G_s solids circulation rate, kg/s

H height above the riser, m

H_{co} cyclone cone height, m

H_{cy} cyclone cylindrical height, m

H_{dz} dense zone height, m

H_{in} cyclone inlet height, m

H_{vf} vortex finder height, m

k_m Reflux ratio

k_m reflux ratio by van der Meer et al. (2000)

K_∞ elutriation rate, kg/m^{2}s

n_r Richardson-Zaki correction constant

Q_s solids volumetric flow rate, m^3/h

Q_s solids volumetric flow rate

Q_{BFB} BFB airflow rates, m^3/h

Q_{ch} chute airflow rates, m^3/h

Q_{ls} loop-seal airflow rate, m^3/h

Q_{pri} primary airflow rate, m^3/h

Q_{sec} secondary airflow rate, m^3/h

Re_p particle Reynolds number

u_o superficial gas velocity, m/s

u_s solids velocity, m/s

u_t particle terminal velocity in stagnant environment, m/s

u_{mf} minimum fluidization velocity, m/s

w width of riser exit, m

BFB bubbling fluidized bed

CAPE Chemical and Process Engineering Department, University of Canterbury

CFB circulating fluidized bed

CFD computational fluid dynamics

DFB dual fluidized bed

FCC fluid catalytic cracking

IGCC integrated gasification combined cycle

Chapter 1

Introduction

Currently, fossil fuels are the dominant energy source for electricity generation and automobile use. The issue with the utilization of fossil fuels is that these resources are unsustainable, and at the same time emit greenhouse gases that contribute to global warming. Renewable energy is one of the solutions to the aforementioned issue, as it does not emit additional greenhouse gases on balance and reduces the reliance on fossil fuels. Biomass, one of the renewable energy sources, is utilized in many countries for power generation (Apergis & Payne, 2010; European Commission, 2008; European Renewable Energy Council, 2009). Biomass has the flexibility of being able to be converted into gaseous or liquid forms of fuels, with the use of biomass derived liquid fuels in automobiles attracting a lot of interest, as it offsets the consumption of fossil fuels (Luo, 1987; Xu et al., 2009). Currently, biomass contributes 10 to 15% of the world energy requirement (Khan et al., 2009). This amount is expected to increase in the future, especially in regards to the utilization of biomass for liquid fuels (European Climate Foundation, Sveaskog, Södra, and Vattenfall, 2010).

In New Zealand, the Ministry of Economic Development has forecasted that biomass will supply 25% of the country's total primary energy by the year 2040 (New Zealand Ministry of Economic Development, 2010). Biomass energy in New Zealand can be supported by residues from the forest industry which is estimated to produce six million tonnes per year (Pang, 2009). Thus, biomass energy presents itself as an abundant energy source that can be utilized for electricity production and transportation purposes.

1.1 Biomass Energy from Fluidized Bed Gasification

Biomass is a fuel source that includes bio-solid wastes or plants from the forestry and agricultural industries. Energy can be derived from biomass through several processes, such as gasification, fermentation, or anaerobic digestion. Gasification is a thermo-conversion technology that is favorable in medium to large scale industrial facilities, as existing equipment can be retrofitted, without major capital expenditure, to produce a combustible gas.

During gasification, biomass is reacted with gasification agent (air, oxygen, or steam) in a sub-stoichiometric environment at temperatures of 700 to 800 °C to produce char and a mixture of volatile gases (containing H_2, CH_4, CO, and C_xH_y) that has low to medium levels of energy content. The gas can then be used for various applications, such as liquid fuel synthesis from Fishcer-Tropsch (FT) process for use in automobiles (Takeshita & Yamaji, 2008). The gaseous fuels can also be combusted in gas turbines, internal combustion engines or boilers to produce power or heat, and can also be used in fuel cells (Wang et al., 2006).

In biomass gasification, fluidized bed gasifiers are widely employed, particularly for large scale systems. Fluidized beds are used because there is a high solid-to-solid interaction rate in the fluidized bed that makes it well suited for the gasification process (Ståhl & Neergaard, 1998; Wu et al., 2008).

There are various types of fluidized bed gasifiers. A bubbling fluidized bed (BFB) is commonly used as a biomass gasifier at medium scale. Sand is often used as a heat transfer material in a BFB due to its inert nature and high thermal capacity. Steam or air acts as the fluidizing gas agent for the biomass, and is fed continuously into the BFB at ratios that provide optimal energy content in the produced gas. The heat transfer material (also called bed material) remains in the BFB and undergoes intense mixing with the gas and biomass. In a BFB, there is no loss of bed material, as the fluidizing gas velocity is relative low, allowing the bed material to remain in the dense bottom region of the BFB.

A circulating fluidized bed (CFB) gasifier operates with a sufficiently high fluidizing gas velocity, causing the dense bottom bed to expand, transporting particles upwards. Thus, above the dense zone, there is a transport zone, where there co-exists two flow regimes: a central upward flow of solids and gas, and an annular downward solids flow

at the wall (Sternéus et al., 2002). The central upward flow results in an entrainment of bed material (solids) out of the fluidized bed. A feedback loop is used to re-circulate this bed material back into the reactor to replenish the solid inventory. This feedback loop consists of a cyclone separator that separates the entrained solids in the gas stream, and a loop-seal that circulates bed material from the cyclone back to the reactor.

A relatively new technology is the dual fluidized bed (DFB) gasifier, a configuration which couples a circulating fluidized bed with a bubbling fluidized bed (Löffler et al., 2003; Kaiser et al., 2003). The two fluidized beds are connected using a non-mechanical valve. The advantage of this configuration is that the CFB can supply heat through combustion of char to drive steam gasification of biomass in the BFB in order to produce gas with high calorific value and high hydrogen content.

1.2 Background Information on CAPE DFB Gasification Plant

A 100 kW DFB gasification system was built in the Department of Chemical and Process Engineering (CAPE), University of Canterbury, and the design concept was based on an industrial scale 8 MW_{th} plant in Güssing, Austria (Löffler et al., 2003; Kaiser et al., 2003). The DFB system in CAPE has undergone experimental runs since 2006 to characterize the gasification efficiency (Bull, 2008). The process flow description of the DFB is presented in detail in Chapter 3.

In an effort to optimize the performance of the CAPE gasification plant, a project was initiated to investigate the hydrodynamics of the DFB system. Factors for consideration included the pressure drop, solids distribution and solids mass flow rates within the system. The quantification of the solids mass flow is important as the solids contain the heat required for sustaining the combustion or gasification process.

1.3 Investigating the Hydrodynamics of Circulating Fluidized Bed Risers

Investigating the hydrodynamics of the fluidized bed is unsafe under typical operating conditions in an actual gasifier where the operating temperature is between 700 to 900 °C. Besides that, some industrial scale fluidized bed gasifiers have riser heights of more than 10 m (Yang et al., 2005). Under these conditions, the solid distribution and solid mass flow rates are not easily measured, unless expensive, dedicated or automated instruments (such as a suction pyrometer) are used.

To allow for the experiments to be performed safely at a more manageable scale, the hydrodynamics of fluidized beds have been traditionally investigated in cold models. This allows the fluidized bed to be operated at ambient temperatures in a lab scale setting. The experimental results from the cold models can provide an understanding useful for the design and optimization of the industrial version of the system. In order for the results from the cold model of the fluidized bed to be applicable when the system is scaled up to the industrial scale, dynamic similarity laws have to be applied. Achieving dynamic similarity would mean certain dimensionless numbers between the cold model and the industrial plant are equal. These dimensionless numbers form the scaling laws for the fluidized bed, which have been reported in the literature (Glicksman et al., 1993; Farrell, 1996; Foscolo et al., 2007; Bricout & Louge, 2004). In this work, a cold model of the gasification plant was designed and constructed to allow the hydrodynamics to be investigated under ambient conditions, in order to provide a better platform for optimizing the performance of the CAPE gasifier. The industrial gasification plant from Güssing, Austria, was used as a template for the cold model, with scaling laws used for the scale down.

Because of the complexity of the hydrodynamics in the DFB system, the project is divided into two phases: Phase I and Phase II. Phase I consists of the experimental investigation and modelling of the hydrodynamics of the CFB riser. The experimental work in Phase I concentrates on the solid fraction distribution, solid mass flow rates and pressure drop values in the CFB riser. Particular focus is given to derive a model that relates the flow rates of solids out of the riser with the flow condition in the riser. The

aforementioned model has not been presented before in literature (Harris et al., 2003; Yan et al., 2003; Mabrouk et al., 2008). Phase II consists of experimental work on the BFB integrated with the CFB riser. The hydrodynamics of a binary mixture is also investigated in Phase II to simulate the biomass char and the bed materials in a practical DFB gasifier.

1.4 Mathematical Modelling of Circulating Fluidized Bed Risers

Mathematical hydrodynamic models of CFB risers can be used as a design tool for a CFB gasification plant, with the advantage of reduced time and cost during the optimization stage compared with an experimental approach to design (Pugsley & Berruti, 1996; Gómez-Barea & Leckner, 2010). Such mathematical models are able to predict the hydrodynamic properties of the plant, such as the solid concentration profile, the solid mass flow rate, and pressure drop.

The hydrodynamic models for CFB risers are often empirical correlations with constants that have been fitted to achieve good agreement between model and measured results. Thus, these models are often only applicable for predicting hydrodynamics in the particular equipment they were developed for (Senior & Brereton, 1992; Schoenfelder et al., 1996). In this work, various hydrodynamic models published in the literature are critically assessed to determine their validity for predicting the hydrodynamics in the cold model of the present work. This is achieved by comparing the prediction of the models with the experimental measurements.

1.5 Hydrodynamics of a Dual Fluidized Bed with Singular and Binary Mixtures

In Phase II of the project, the dual fluidized bed (DFB) consists of the BFB integrated with the CFB. Two additional operating variables are added to the plant: the fluidizing airflow into the BFB and the connecting chute (between the CFB riser and the BFB). The

effects of these two additional parameters are investigated in relation to the steady state operation of the DFB system. An operational map is also developed to denote the different regions of operation. Such an operational map has not been investigated widely in the literature (Kehlenbeck et al., 2001; Goo et al., 2008; Charitos et al., 2010).

The above mentioned experiments are performed initially with only bed material representing sand in an industrial gasifier. The experimental work then focuses on a binary mixture, with a secondary solid material used in the cold model to represent char under high temperature conditions in the gasification plant.

1.6 Computational Fluid Dynamics Modelling of Cold Model CFB Cyclone Separator

Cyclone separators are the most commonly used device in industry for removing particulates from gas flow. These devices are commonly found in various applications of fluidized beds, including fluid catalytic cracking (FCC), circulating fluidized bed combustion (CFBC) and integrated gasification combined cycles (IGCC) (Utikar et al., 2010).

A high separation efficiency of the cyclone is important to maintain the solids mass flow rate around the plant for steady state operation. In addition, operational issues associated with the cyclone separator, such as the wall erosion, can be investigated. Wall erosion has been encountered in the cyclone separator of the pilot-scale CAPE gasification plant. On two separate occasions after a long series of experiments, the CFB cyclone suffered severe erosion near the inlet region (McKinnon, 2009). The eroded region is shown in Fig. 1.1. The erosion of the cyclone separator prompted an investigation carried out in this work to determine how the operating life of the cyclone separator could be lengthened. A design tool has been developed that can be used to predict the flow patterns and particle tracks in a cyclone. This design tool is based on a Computational Fluid Dynamics (CFD) approach. CFD uses mathematical equations and numerical algorithms to model fluid flows in applications such as cyclones (Chung, 2002; Utikar et al., 2010).

In this study, the CFD based design tool is first developed by using CFD to simulate a

cyclone described in literature with a good set of experimentally measured velocity data associated with it. The experimental data is used to validate the CFD modelling approach. The modelling approach is used to validate the CFD modelling approach. The modelling approach developed is then applied to predict flow patterns in the cold model cyclone. Validation of the modelling approach for the cold model is performed by comparing the predicted pressure drop from the CFD model with experimental results from the cold model cyclone. In addition, preliminary investigations are performed to determine particle trajectories within the cyclone and likely particle impact zones on the cyclone wall.

Fig. 1.1: Damaged region due to erosion and wear near the inlet of the cyclone in circulating fluidized bed gasifier of CAPE.

1.7 Summary of Objectives

The increase in utilization of biomass energy encourages a deeper understanding of fluidized bed gasifiers for better design, scale-up and optimization of these processes. The main objective of the present work is to investigate the hydrodynamics of a dual fluidized bed gasifier. The hydrodynamic properties of the CFB (Phase I of the project) are investigated experimentally, in terms of solid fraction distribution, solid mass flow rate, and the pressure drop in the CFB riser. The relation of these parameters with the operating and geometrical parameters is the focus of the investigation. A critical assessment is also made on published hydrodynamic models used to predict hydrodynamic properties of

the CFBs. The focus then moves onto on the DFB (Phase II of the project), with initial experiments on a singular bed material. Investigations on a binary mixture bed material in the DFB are also performed, using a secondary material to represent biomass char. Finally, a design tool is developed for investigation of the performance of the cyclone separator.

1.8 Thesis Outline

Chapter 2 provides a literature review of the work on the hydrodynamics of the CFB and BFB. Moreover, the review highlights the knowledge gaps on the impact of geometrical effects on the solid flow rate. The review also highlights the complexity of a complete, physical mathematical framework to model the gas-solid flow dynamics in a fluidized bed. Furthermore, the review also shows that there is a lack of information in the literature on operational ranges required for steady state operation of a dual fluidized bed, in addition to limited work presented on binary mixtures that represent biomass char and bed material in dual fluidized beds. Chapter 3 gives a brief overview of the scaling laws used to design the cold model plant. Chapter 3 is also focused on the experimental results from Phase I with regards to the hydrodynamic properties. An operational map for a CFB is also provided, and relates to the operational and fluidization regimes of the plant. A significant contribution from Chapter 3 is the development of a model that predicts the solids mass flow rate out of the CFB riser. Chapter 4 then presents the work on a critical assessment of the mathematical models to predict the hydrodynamics of the CFB riser. Various theories and assumptions used in the hydrodynamic models of the riser are presented, followed by a discussion of the discrepancies between the predicted and experimental results, and the validity of the assumptions. Chapter 5 presents results from Phase II of the project, which includes an operational map developed to denote regions of stable operation of the dual fluidized bed system, with only bed material circulating through the system. The effect of the fluidizing airflow into the BFB and the chute on the system is also investigated. This chapter also presents results of the hydrodynamics of a binary mixture within the cold model. Chapter 6 then presents work of a CFD based design tool developed for modelling the cyclone. Chapter 7 is the overall

conclusion of the thesis, where the main findings of the thesis are summarized. Potential further research work related to this thesis is recommended in Chapter 7.

Chapter 2

Literature Review

2.1 Fluidization Regimes and Particle Classification

The fluidized bed reactor contains inert bed material, normally a solid such as sand which is fluidized by gas. The inert material serves as a heat transfer medium to promote reaction within the fluidized bed. The interaction between the inert material and fluidizing gas determines the flow behaviour of the fluidized bed.

The basic fluidization regimes of the fluidized beds are shown in Fig. 2.1 (Grace et al., 1997). From the figure, it can be seen that in general, with an increase in superficial gas velocity, the fluidization regime transits from a fixed bed through to phases of bubbling, slugging, turbulent and fast fluidization flow. In extremely high gas velocities, the fluidized bed transits to pneumatic conveying flow, and most of the bed material will be transported out of the reactor. These regimes have been characterized extensively in literature (Grace et al., 1997; Gibilaro, 2001; Brandani & Zhang, 2006), and are briefly described here.

With the gas velocity lower than a certain limit, known as the minimum fluidization velocity u_{mf}, the cohesive drag force due to the upwards gas flow through the voids in the bed of material. The bed is stationary at these velocities. When the gas velocity reaches the minimum fluidization velocity, the drag force from the gas flow is sufficient to overcome the gravitational force and the cohesive resistance of the particles. Thus, the distance between individual particles increases, which increases the voidage and the particles fluidize. With further increases in velocity, the pressure drop over the bed

remains constant since the drag force exerted on the fluidized particles by the gas flow is essentially balanced by the weight of the bed. This operating condition is called the delayed bubbling bed (Fig. 2.1) and has been denoted by other authors as homogeneous fluidization (Gibilaro, 2001; Brandani & Zhang, 2006).

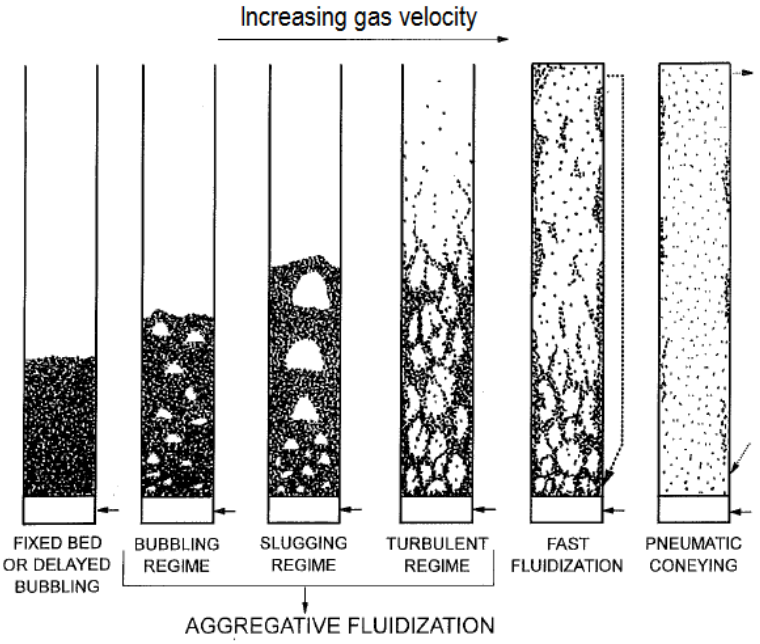

Fig. 2.1: Various fluidization regimes (Grace et al., 1997).

By increasing the velocity further, the bed transits from delayed bubbling to the bubbling regime. Larger distinct voids or bubbles are formed within the bed. The bubbles then move upward, before bursting at the surface of the bed material. Small amount of particles follow in the wake of the bubbles, and as the bubbles erupt through the surface, the particles are ejected upward. The velocity at which bubbling regime starts is called minimum bubbling velocity, and is normally found to be two or four times the minimum fluidization velocity. However, there are also cases where the bubbling regime starts even when the bed has just reached minimum fluidization, and there is no transition regime from the delayed bubbling bed to the bubbling regime (Geldart et al., 1979; Gibilaro, 2001). This will depend on the type of particles being used, as described later in Section 2.2.

If the gas velocity is increased further, the bubble size continues to increase until it is close to the diameter of the reactor, forming slugs of gas. This is the slugging fluidization regime, and is normally avoided in normal fluidized bed operation. This is

because gas will tend to flow through the slugs instead of flowing through the surrounding particles, hence decreasing the gas and solid contact time. Therefore slugging regime is generally an undesirable feature in a fluidized bed application.

A higher gas velocity entrains more solids and carries the solids upward and out of the fluidized bed. The rate of entrainment depends on the terminal velocity of the particle, u_t , which is the constant velocity of a free falling particle in a stagnant environment. Since the terminal velocity of finer particles is lower, more fine particles will be entrained in the gas at high gas velocities, causing a loss of bed material. At this stage, the solid entrainment will reach a constant value with an increase in fluidized bed height. The solid entrainment rate under this condition is also known as the elutriation rate K_∞, and is normally associated with the proportion of fine particles. The fluidized bed is now undergoing turbulent fluidization as shown in Fig. 2.1. In the turbulent fluidization regime, the bubbles have evolved to a non-distinct shape, and the elutriation rate of particles from the fluidized bed is high. The higher elutriation of particles will cause a higher loss of material in the bed and thus the pressure drop across the bed will decrease with an increase of gas velocity.

With a further increase in gas velocity exceeding the terminal velocity of a large portion of the particles, more particles are entrained into the central gas stream and are conveyed out of the fluidized bed. Some of these entrained particles disperse towards the wall of the fluidized bed and flow downward along the annular wall layers into the bottom section of the fluidized bed. The higher solids entrainment is typical of a circulating fluidized bed (CFB) and the flow regime may extend to the fast fluidization regime (Fig. 2.1).

A continuing increase in the gas velocity beyond the fast fluidization regime will lead to pneumatic flow. The solid volume concentration (or the solid fraction) in this regime is dilute throughout the whole length of the fluidized bed and, in this case, there is no bottom region that is densely concentrated with solids.

Besides the different fluidization regimes mentioned above, fluidization is also affected by the type of particles used for the inert material. The particles used as bed materials are divided into four Geldart particle groups according to the particle density and size, as shown in Fig. 2.2, with the four groups denoted as Group A, B, C and D.

Each group has its own fluidization characteristics according to their particle density and size. Geldart Group A particles are small in particle size (30 to 100 μm) and have particle densities that are typically lower than 1400 kg/m^3. Group A particles exhibit a transition behaviour from delayed bubbling to the bubbling regime, and bubbles will only form when the minimum bubbling velocity is reached. Group B particles have particle sizes that range up to 1.0 mm. This group of particles does not have a transitional phase and will fall into the bubbling regime once minimum fluidization is reached. Group C particles consist of fine powders with particle size less than 30 μm and are difficult to fluidize due to their strong cohesive forces. Group D comprises of coarse particles with particle sizes exceeding 1.0 mm and are also difficult to fluidize (Gibilaro, 2001).

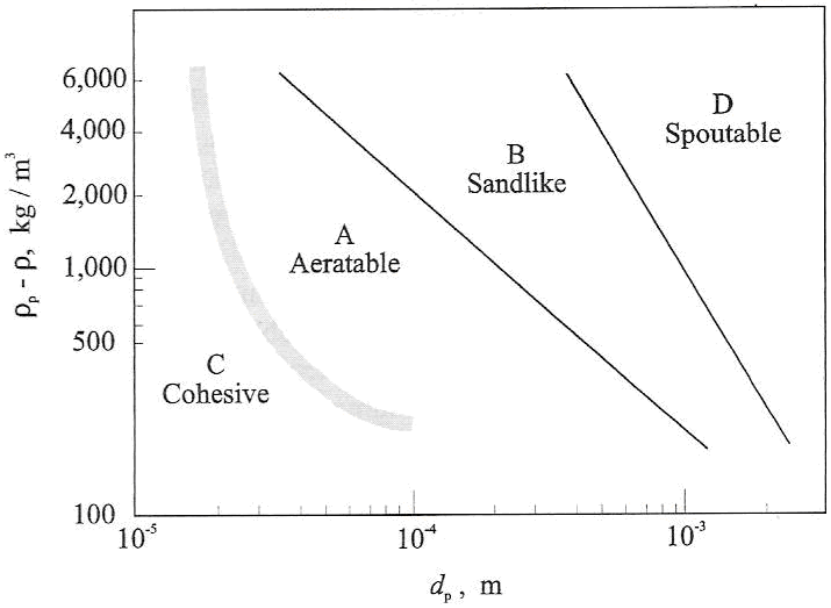

Fig. 2.2: Particle classification according to the Geldart groups (Gibilaro, 2001).

The hydrodynamics of the gas-solid flow in the fluidized bed are described above in a simplified manner, however, recent studies (Davidson, 2000; Mabrouk et al., 2008; Zhu & Zhu, 2008) on various aspects of fluidized beds indicate that the flow characteristics are far more complex. Furthermore, the application of fluidized beds in the field of biomass energy processing (combustion, gasification and pyrolysis) has sustained and renewed the interest to perform further research into the hydrodynamics of fluidized beds (Reh, 1999, 2003). As mentioned in Chapter 1, the hydrodynamics are normally investigated in scaled down, cold model versions of the industrial, high temperature fluidized bed systems. The

cold model plants are normally designed using the scaling laws of fluidized beds.

2.2 Scaling Laws of Fluidized Beds

In order to achieve dynamic similarity between various scales of fluidized beds, scaling laws of the fluidized bed have been proposed by Glicksman et al. (1993). Using the scaling laws, the results of hydrodynamics in a fluidized bed from a small scale apparatus can be applied to large scale systems. Conversely, the application of scaling laws allows the hydrodynamic behaviour of a large scale system to be investigated on a lab scale apparatus as well.

In the proposed scaling laws, nine dimensionless numbers are involved: the Froude number (Fr), the Archimedes number (Ar), Reynolds number (Re), the density ratio, the dimensionless solid circulation rate, the particle sphericity (ϕ), the particle size distribution (PSD), the fluidization index, and the geometry ratio. Kolar & Leckner (2006) used the Glicksman's scaling law to scale down a 12 MW_{th} CFB boiler to one-sixth of its scale for laboratory testing. However, in the scaled-down version, it was not possible to use all of the nine dimensionless numbers, as a change in one of the parameters (such as the density) affected several dimensionless numbers (Kolar & Leckner, 2006). In other words, the dimensionless numbers were not independent of each other. Therefore, a simplified version of the scaling laws has been used to scale down fluidized bed gasification plants, and this simplified version consists of only four dimensionless numbers (Foscolo et al., 2007). Foscolo et al. (2007) described visual observations of solids motion in an industrial fluidized bed and a down-scaled model, which demonstrated dynamic similarity of the two flows, and hence suggested that the four dimensionless scaling parameters were sufficient to achieve dynamic similarity. In addition, the scaled-up plant showed a uniform bed temperature, indicating proper mixing of fuel as observed in the cold model.

Due to the encouraging results that have been reported by Foscolo et al. (2007), the scaling procedure for the fluidized bed in this study has employed a similar simplification procedure. The dimensionless parameters in this study are the Archimedes number, the flow number, the density ratio, and the geometrical ratio, and in addition the

dimensionless solids circulation rate, $G_s/(\rho_s u_s)$ for scaling circulating fluidized beds (Glicksman et al., 1993; Bricout & Louge, 2004).

Having applied the scaling laws to gasification plants, the authors above have proceeded to investigate the hydrodynamics in scaled down versions of the fluidized beds under ambient conditions (Foscolo et al., 2007; Kehlenbeck et al., 2001). Other authors have followed suit, and have concentrated their efforts on investigating the hydrodynamics of the fluidized beds, especially those of the CFB riser (Löffler et al., 2003; Kaiser et al., 2003).

2.3 Experimental Investigation of the Hydrodynamics of CFB Risers

As mentioned earlier in Chapter 1, the project was divided to Phase I and II, with the CFB riser as the focus in Phase I. A typical configuration of the CFB is shown in Fig. 2.3. The review in this section will highlight that there are still issues or areas requiring further investigation to improve the understanding on the hydrodynamics of the CFB riser. These issues include a lack of an operational map for steady state operations of the CFB riser, and a gap in understanding the effect of the exit geometry on the solids mass flow rate from the CFB riser.

2.3.1 Operational Map for a CFB Riser

For operating a CFB plant, if the limits on the operating parameters are known within which steady state operation of the plant is ensured, unwanted shutdowns or instabilities can be avoided. A CFB riser (refer to Fig. 2.3) operating at steady state will typically have sufficient solids outflow rate (solids entrainment rate out of the riser) to ensure good heat transfer rates, and a constant solid inventory (indicated by a constant time trend of pressure drop over various points across the plant) so that it does not run empty. In addition, the non-mechanical valve is crucial for steady state operation of a CFB. The non-mechanical valve, which can be a loop-seal (Fig 2.3) or an inclined chute, functions as a gas seal to prevent fresh gas from mixing with the flue gas or syngas, and also functions as a valve that returns material from the cyclone back to the CFB riser. An

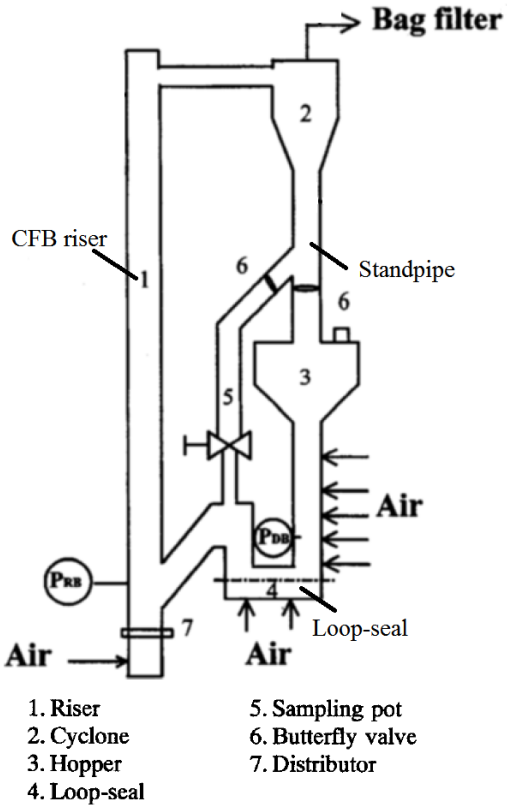

Fig. 2.3: A typical CFB configuration (Kim et al., 1999).

operational map can be used to graphically demarcate areas of steady and unsteady state operation of a CFB, so that suitable operating conditions (for example, fluidizing gas flows) can be chosen to ensure that solids recirculation is sufficient and the non-mechanical valve is operating properly.

However, operational maps for circulating fluidized beds with regards to the loop-seal and fluidizing airflows in the CFB (both primary and secondary airflow) were not found in literature. Usually found in literature were correlations of the loop-seal solid circulation as a function of the pressure drop or vice versa (Monazam et al., 2007; Grieco & Marmo, 2006; Cheng & Basu, 1999). The influence of operating parameters on the loop-seal mass circulation and pressure drop have been documented as well (Monazam et al., 2007; Yang et al., 2009; Charitos et al., 2010). These models are highly empirical, because the correlations were derived from experimental results that varied greatly depending on plant type and loop-seal design configurations, thus limit the applicability of the models. In addition, these studies did not address the loop-seal effect

on the operational regions of the CFB system.

In a study by Yang et al. (2009), a new correlation was proposed to determine the loop-seal solid flow rate which was a function of gas velocities in the loop-seal and in the CFB, and the amount of solids or solid inventory in the system. The correlation showed that the loop-seal solid flow rate increased with increase in fluidizing velocities in the loop-seal and in the CFB, and also with the solid inventory.

Similar work on the loop-seal was presented by Monazam et al. (2007), and a correlation to predict the loop-seal solid flow rate was derived. Monazam et al. (2007)'s correlation was a function of dimensionless numbers, which differs from that of Yang et al. (2009). None of these works provide an operational map that defines steady state operation of the CFB riser in relation to the loop-seal.

Further evidence of the absence of an operational map was shown in other studies. Geldart & Jones (1991) investigated the flow dynamics of different loop-seal configurations, and also characterized the relative velocity between gas and solid in the standpipe section. In their study, the inlet of the loop-seal was connected to a hopper while the discharge was exposed to atmosphere. As the loop-seal was studied independently, the relationship of the loop-seal with other plant operating parameters was not investigated. In a separate study by Kim et al. (2002), a pressure balance model was derived to close the calculation loop of the hydrodynamic mathematical model of a CFB by including the loop-seal. However, the hydrodynamic model required the measured loop-seal solids flow rate and the total solid inventory as input parameters for the calculation. In a study by Cheng & Basu (1999), the solid friction factor was used to predict the pressure drop in the loop-seal. Grieco & Marmo (2006) developed a correlation to predict the pressure drop across the loop-seal and showed close agreement between their predicted results and experimental data.

Other authors mapped the operation conditions of the CFB riser using different approach, not providing an operational map that denotes the boundaries of steady state operation of a CFB riser. The flow regimes of a CFB riser was characterized by Monazam et al. (2005) with respect to the time required to empty the solids out of the riser at different gas velocities. Based on the measured results, the emptying time was plotted against the gas velocities from which three fluidizing regimes (Regions I, II and

III) were observed, as shown in Fig. 2.4. These three regions were the dense phase turbulent flow, fast fluidization flow and dilute, pneumatic conveying regime respectively.

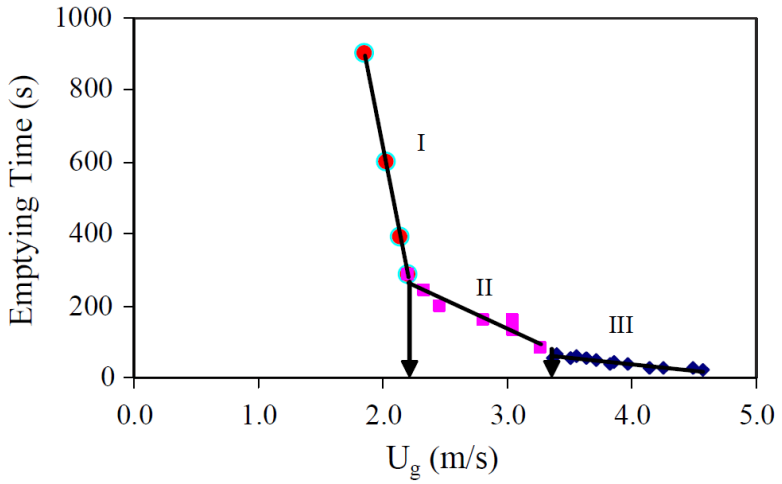

Fig. 2.4: Emptying time for solids in a riser as a function of superficial gas velocity, showing three different flow regimes (Monazam et al., 2005).

To summarize, previous studies on the loop-seal were found to focus on developing correlations to predict the loop-seal solid flow rate and the pressure drop of the loop-seal. The correlations, however, are highly empirical and thus have limits in their applications to a wide spectrum of CFB systems. Other approaches attempted to demarcate different flow regimes of the CFB, but these studies did not demarcate regions of steady state operation of the CFB system. In this study, an operational map that defines the boundaries for steady state operation conditions of the CFB with regards to the different airflows and loop-seal airflows is developed. Further experimental measurements of the hydrodynamics, such as the solid fraction, is performed using the operational map to decide on suitable operating conditions for steady state operation of the plant.

2.3.2 Measurements of Solids Fraction and Solids Mass Flow Rates

Under steady state operation, the bed material will be circulated in the CFB continuously. The continuous circulation of bed material in the CFB causes an axial gradient of the solid volume concentration or solid fraction ($\varepsilon_s = 1 - \varepsilon$) over the height of the CFB riser. The solid volume fraction and its gradient or distribution, along with

the solid flux profile, is an important parameter that determines the solid mass flow rate and the pressure drop and thus the operational performance of the system. Hence, the knowledge of the solid fraction, the solids mass flow rate and pressure drop is of great interest to CFB designers, as it influences the choice of diameter and height of the CFB riser during initial design, and airflow ranges for subsequent operation.

The solid fraction distribution in the radial and axial directions (and also the solid flux) of the CFB riser is sometimes measured in a cold model plant under near ambient conditions to provide an insight into the likely distribution of solids in the high temperature gasification plant, because these measurements are unsafe or require cumbersome instrument set-ups in the high temperature systems. For example, in the study by Yan et al. (2005), a suction probe was traversed in the radial direction to measure the local upward solid flux in the cold model. This procedure was repeated at different heights. Thus, an axial distribution of the solid flux and solid fraction in the riser is obtainable by integrating the radial profiles at each height.

There are fluctuations associated with the measurement of the solid flux using the suction probe. These fluctuations in the CFB riser are caused by the random formation and disintegration of clusters. Clusters are formed within the CFB when the particles aggregate with each other; while particles may also detach from the downward flowing solids in the wall, and become entrained into the upward flowing airflow (Davidson, 2000). The clusters may also originate from the bubbles that erupt violently in the bottom dense bed. Particles are ejected sporadically upwards from the erupting bubbles (Almendros-Ibáñez et al., 2009), leading to fluctuation in the local solid concentrations. These fluctuations are unavoidable and are reflected in variations in the measured solids flux.

Despite these fluctuations, due to the simplicity and reliability of suction probe for measuring the local solid flux as shown by Yan et al. (2005), the suction probe is used in this study to measure the local solid flux measurements. Then, the solids mass flow rates and the solids fraction within the CFB riser are then determined from these measurements.

As mentioned earlier, in a CFB gasifier, heat and mass transfer rates are closely related to the solid mass flow rate which is critical for stable functioning of the CFB.

Specifically, the solid core flow rate $\dot{m}_{core}$ (solids upward mass flow rate within the CFB riser) and the solid outflow rate $\dot{m}_{so}$ (solids mass flow rate out of the CFB riser) should be estimated. The solid outflow rate from the CFB riser can be measured by using a diverting valve which diverts the flow of solids in the standpipe into a measuring vessel (Yan et al., 2005). In this way, the solid outflow rate can be determined from the increase rate of solid accumulating in the measuring vessel, which is reflected by the increase of solid layer level. Another method of measuring the solid outflow rate was suggested by Charitos et al. (2010) who stopped the loop-seal aeration, and measured the increase in bed height in the standpipe within a certain period of time. This method is simple as it does not require additional equipment to be fitted into the system.

From the experiments of Charitos et al. (2010), the CFB entrainment rate or the CFB solid outflow rate was estimated in an empirical manner on a dual fluidized bed system for CO_2 capture. The system used calcium oxide (CaO) as the bed material, which functioned as a sorbent that reacted with CO_2 to produce calcium carbonate. The results presented by Charitos et al. (2010) were from a scaled down cold model, and were used as the basis for the design and operation of the larger dual fluidized bed system. The solids outflow rate was given as a function of the pressure drop of the riser exit, and also the gas velocity. In the current research work, a similar approach as taken by Charitos et al. (2010) is employed, with solids outflow rates from the CFB measured by stopping loop-seal aeration and measuring the increase in bed height in the standpipe.

Besides the work presented above on the solids flow rate, it is also interesting to estimate the solids outflow rate for different CFB exit widths. There have been studies that relate the effect of the exit geometry on the amount solids reflux. These researchers characterized different exit geometries with relation to the ratio of solid outflow rate and downward solid flow rate in the annular walls layers, $\dot{m}_w$ (van der Meer et al., 2000; Richtberg et al., 2005). A brief review of these studies is presented in the next section.

2.3.3 Effect of Exit Geometry on Solids Circulation Rate

The work from Kunii & Levenspiel (1995), who examined the effects of exit geometry in a 9.3 m high CFB, have found that with an abrupt exit configuration in a riser, the axial solid concentration profile would be higher near the top of the CFB. The increase in solid

concentration near the top of the CFB is caused by reflux of particles that flow downward near the wall. It is of interest to quantify this reflux because the particles that re-enter the CFB riser flow downwards in an annular layer at the wall. This downward flow of particles affects the heat transfer to the water-tube heat exchangers that line the walls of a CFB boiler.

The effects of exit geometry was quantified by van der Meer et al. (2000) using a reflux ratio (k_m) which was defined as the ratio of downward solid flow rate in the annular wall to the solid outflow rate. The circulating fluidized bed investigated by van der Meer et al. (2000) was 5.1 m high and had a square cross-section of 140 mm $\times$ 140 mm. The downward solid flow rate was measured by using a capacitance probe at positions of 0.14, 0.64 and 1.14 m below the exit. The solid outflow rate from the CFB was determined by measuring the solid accumulation rate over a certain period of time, by closing a valve in a weighing hopper just after the cyclone. The reflux ratio developed by van der Meer et al. (2000) has been used to characterize different CFB exit configurations and are illustrated in Fig. 2.5.

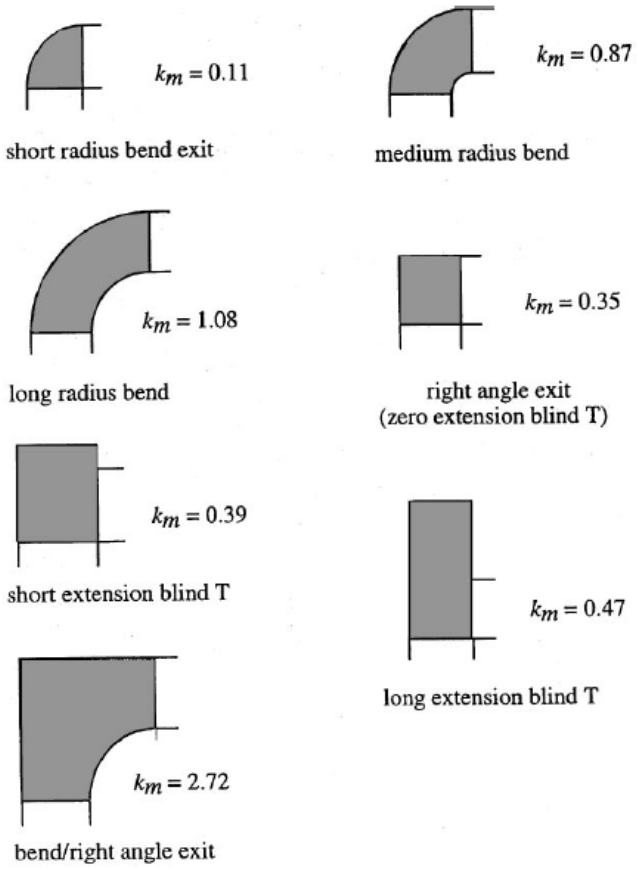

Fig. 2.5: Different exit configurations with respective reflux ratios, k_m (van der Meer et al., 2000).

A reflux ratio that is relevant to the exit geometry of the CFB riser in this thesis was selected from values given by van der Meer et al. (2000). The reflux ratio is compared (in Chapter 4) to experimental values and those predicted from a model developed in Chapter 3. A qualitative assessment on the downward solid flow rate caused by the exit geometry is also performed by using a tube that was fixed to the inside of the walls, to measure the amount of solids flow rate in the annular wall layer (Chapter 3).

2.3.4 Pressure Drop Measurements

The pressure drop of the CFB riser has been measured experimentally using pressure transducers by Löffler et al. (2003); Kaiser et al. (2003); Monazam et al. (2005); Goo et al. (2008); Charitos et al. (2010). Several authors used the pressure drop across a small height increment to infer the solid fraction (Harris et al., 2003; Goo et al., 2008). This method was not pursued in this study, because the solid fraction was determined by

using the suction probe method described above instead.

From the experimental measurements of the pressure drop, a comparison of the measured and predicted pressure drop is made for validation purposes of the model. Modelling of the pressure drop is part of the hydrodynamic modelling work on the CFB riser. A review on the various hydrodynamic models is included in Section 2.4.1, and the review on modelling of the pressure drop is presented in Section 2.4.3.

2.4 Hydrodynamic Modeling of Circulating Fluidized Beds

2.4.1 Prediction of Axial Solid Fraction

The design of fluidized beds would benefit from the use of mathematical models to estimate hydrodynamic properties of the CFB riser, such as the axial solid fraction and the pressure drop. From the model predictions, configuration and dimensions of the plant can be determined. Three types of models have been found in literature. There can be characterized respectively as: (1) Type I models that predict the average axial solids profile only; (2) Type II models that predict the axial and radial solids profile by assuming a core-annulus flow regime; and (3) Type III models which predict two-phase gas-solid flows through two-phase continuity and conservation equations (Harris & Davidson, 1994).

The axial solid fraction profile along the CFB riser height can be predicted using the hydrodynamic models from any of the three types described in the previous section. However, Type I and II models are highly empirical, with the coefficients of the associated model correlations usually being fitted using experimental data. This limits the applicability of these models in cases where the dimensions or operation conditions are out of the ranges tested (Kunii & Levenspiel, 1991; Pugsley & Berruti, 1996; Kim et al., 2002; Pallarés & Johnsson, 2006). However, clearly these models are useful in cases where the plant dimensions and operation conditions are within the tested ranges. In addition, reaction kinetic models are easily coupled with Type I and II models (Berruti et al., 1995; Pallarés & Johnsson, 2006). Therefore, Type I and II models are often used

as design tools to investigate the effect of operating conditions and dimensions on the solids fraction and solids mass flow rates.

Type III models are based on fundamental equations of fluid dynamics, and consist of the constitutive equations of continuity, momentum and energy conservation. Therefore, Type III models can be applied in a wider range of plant dimensions and operation conditions to describe the local flow structure in more detail. Type III models also provide more insights to the micro-flow structure, such as the flow in the corner of the CFB or around a bend. However, Type III models require significant amount of computational effort, therefore its use is currently limited to individual components of the plants (Berruti et al., 1995; Zhang et al., 1991; Taghipour et al., 2005; Knowlton et al., 2005; Ravelli et al., 2008).

From the above analysis, Type I models are applied in this study as the focus is on the averaged axial solids fraction. As already mentioned in Chapter 1, the model results are compared with experimental measurements from the cold model to elucidate the differences to determine the validity of the models.

Type I models include parameters that are determined by different forms of correlations. Some correlations are a function of operating conditions, plant dimensions, fluid dynamics and material properties, such as gas velocity, riser diameter, and particle diameter (Geldart et al., 1979) and Colakyan & Levenspiel (1984) which involved the gas velocity, riser diameter or particle diameter. Other correlations involve dimensionless numbers. These correlations have been developed over a range of operating parameters and have been fitted to experimental results (Monazam & Shadle, 2008).

Different correlations have been developed for different regions of the CFB riser. For instance, there have been correlations developed for predicting the void fraction or the voidage of the dense zone at the bottom of the CFB riser (Johnsson et al., 1991; Monazam & Shadle, 2008). The void fraction in the bottom of the riser could also be determined by using the expanded bed heights of the dense zone and performing a mass balance; details of the calculations can be found in literature (Johnsson et al., 1991; Babu et al., 1978; Lewis et al., 1949; Kunii & Levenspiel, 1991). However, due to the instability of the fluidization behaviour in the dense zone, the dense zone voidage is commonly predicted by fitting the correlation to the experimental values (Senior &

Brereton, 1992; Schoenfelder et al., 1996; Gungor & Eskin, 2007).

In the studies of Senior & Brereton (1992), Schoenfelder et al. (1996), and Gungor & Eskin (2007), other parameters, such as the elutriation rate, K_∞ which is the constant solid entrainment rate at an infinite distance from the surface of the dense zone of a fluidized bed has also been fitted. The decay constant a_d which defines the profile of the axial solid concentration distribution away from the surface of the dense zone of a fluidized bed, is also fitted. Bai & Kato (1995) derived a saturation carrying capacity as a function of the dimensional parameters of the Archimedes number, the Froude number, and the density ratio. Geldart et al. (1979) and Colakyan & Levenspiel (1984) proposed the elutriation rate as a function of the particle terminal and gas superficial velocity. Again, these equations were fitted to the respective experimental results, and may not apply to other systems if the operating conditions are different.

Besides that, experimental input was occasionally required for using the correlations. Correlations for the decay constant a_d and the dense zone voidage were derived as a function of the density ratio, the Froude number, the external solid flux, and the geometry of the CFB riser by Kim et al. (2002). The model proposed by Kim et al. (2002) required input values of the solid outflow, the solids inventory, the geometry of the plant and the gas velocity. The solid outflow needs to be measured experimentally, before the values can be provided for the hydrodynamic model to predict the solid fraction. This limits the general applicability of the model.

Another example of parametric fitting of a hydrodynamic model is given in the work of Schoenfelder et al. (1996), who developed a two-dimensional ozone decomposition reactor model for circulating fluidized beds. An ozone generator injected ozone into the main air supply directly after the blower to ensure sufficient mixing. The decomposition of ozone by iron oxide based catalysts was then modelled by incorporating a hydrodynamic model with the reaction model for axial ozone decomposition. All the parameters for the hydrodynamic model were fitted to the experimental results in order to obtain a value for the reaction rate of the ozone decomposition process.

The simplification of the modeling work suggests that although there are a number of correlations for different parameters found in Type I models, no general correlation can be applied to any specific CFB riser for accurate prediction of the hydrodynamic

properties. In this work, different published correlations associated with Type I models are critically assessed. The assessment is performed by comparing predicted results of the model with the experimental results from this study.

2.4.2 Prediction of Solids Mass Flow Rate

Once the axial solid fraction (ε_s) is determined using hydrodynamic model, the solids core flow rate and the pressure drop can be modelled. The solids core flow rate can be calculated if the solid density, velocity and cross-sectional area of the riser are known. In order to determine the solids velocity, a simplistic model can be developed by performing a force balance over a single particle. This process normally results in a differential equation which can be solved using numerical methods with a guess value for the initial solid velocity (Löffler et al., 2003).

Some assumptions are made in establishing the force balance over a single particle in the transport zone of the CFB riser. Firstly, the solid concentration in the CFB riser is assumed to be dilute and secondly, the flow is assumed to have reached a fully developed state. A third assumption, which has been applied in other publications, is that the solid outflow from the CFB is equal to the solids core flow at the height of the exit point of the riser (Richtberg et al., 2005; Senior & Brereton, 1992). The applicability of these models and the validity of the above assumptions are assessed in this study.

2.4.3 Modeling of the CFB Riser Pressure Drop

The pressure drop in the CFB riser is an important parameter both for plant design and for operation as it is indicative of the solid fraction. Pressure drop is normally modelled in two parts of the CFB riser, the bottom dense zone and the upper dilute, transport zone. In the bottom dense zone, the pressure drop can be determined from the void fraction, and is considered to be related to the weight of solids per unit height (Pugsley & Berruti, 1996). In the upper dilute transport zone, the total pressure drop per unit length is a summation of the hydrodynamic head of the solids ΔP_s, the pressure drop due to gas and solids acceleration, $\Delta P_{g,acc}$ and $\Delta P_{s,acc}$, and the frictional pressure drop (ΔP_{sf}).

$$\Delta P = \Delta P_s + \Delta P_g + \Delta P_{g,acc} + \Delta P_{s,acc} + \Delta P_{sf} \tag{2.1}$$

The pressure drop due to gas acceleration in the riser is negligible. The pressure drop due to solids acceleration was calculated by Gungor & Eskin (2007) as a function of the solid velocity squared and the solid fraction. In the model proposed by Gungor & Eskin (2007), the frictional force of the gas on the walls was a function of the gas Reynolds number. For the frictional force between the solids and the walls, there is a solid-and-wall friction factor, and is given in many forms by Gungor & Eskin (2007), Nakamura & Capes (1973), Nieuwland et al. (1997). The correlations developed by the aforementioned authors were functions of the solid particle density, the solids velocity or the annular solids velocity. For the solids annular solids velocity, there were separate correlations (Namkung & Done Kim, 1998; Rhodes et al., 1992), which added to the complexity of predicting the solids frictional pressure drop.

Previous studies (Gungor & Eskin, 2007; Nieuwland et al., 1997) showed that reasonable agreements could be achieved between the predicted results and the experimental values. However, Nakamura & Capes (1973) reported that the inclusion of solids-to-wall frictional forces could result in an over-prediction of the transport zone pressure drop by a factor of 10 or higher. Furthermore, Nieuwland et al. (1997) found that at lower gas velocities (in the fast fluidization regime), the hydrodynamic head of the solid phase was the most significant component for the overall pressure drop, as shown in Fig. 2.6 (Nieuwland et al., 1997). From the figure, it is observed that the hydrodynamic head of solids becomes less significant as the gas velocity increases and the fluidization approaches pneumatic flow regime. Under this situation, the frictional forces become more dominant (Nieuwland et al., 1997). It was also found that the solid acceleration component as included in Eq. (2.1) is actually negligible in the upper region of the riser since the flow has become fully developed and the change in the solid velocity with variation in riser height is insignificant (Nieuwland et al., 1997). In view of the findings from Nieuwland et al. (1997), the pressure drop due to frictional forces and solids acceleration are neglected in the hydrodynamic model in this study.

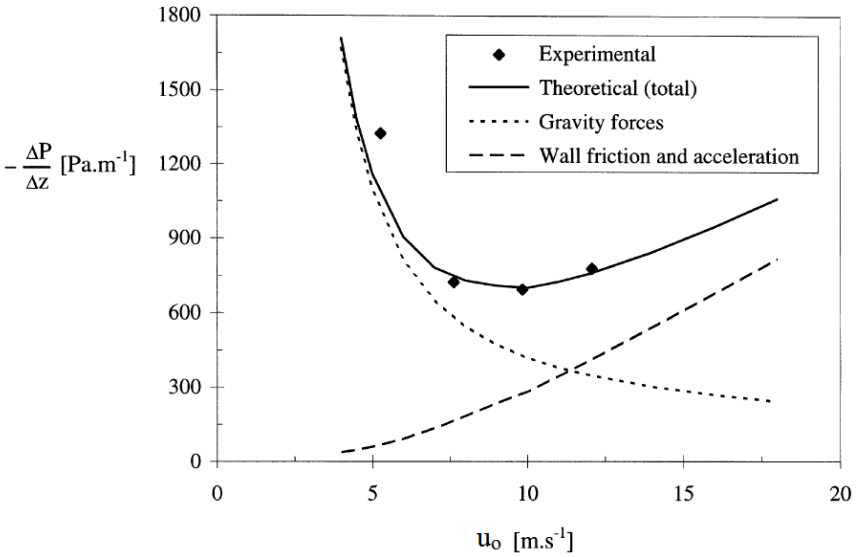

Fig. 2.6: Predicted and experimental pressure drop per height as a function of gas velocity (Nieuwland et al., 1997).

In the current study, after the experimental work and hydrodynamic modelling on the CFB riser (Phase I) is done, the investigation of the hydrodynamics proceeds to the dual fluidized bed (DFB), which is Phase II of the project.

2.5 Hydrodynamics of a Dual Fluidized Bed with Singular and Binary Mixtures

2.5.1 Hydrodynamics of Dual Fluidized Beds with a Singular Bed Mixture

There have been several publications on the hydrodynamics of the DFB, but existing studies do not present an operational map to mark boundaries for steady state operation. For example, the study by Goo et al. (2008) presented the axial solid fraction, pressure drop and solid mass flow rate in a cold model DFB. However, an operational map for steady state operation was not shown. A study by Charitos et al. (2010) presented the operational regions of the CFB plant, where the authors defined the operating behaviour of the CFB with respect to the CFB gas velocity, the CFB pressure drop and total solids inventory. However, the operational condition of the chute and loop-seal were not

included in the study by Charitos et al. (2010). Hence, this thesis aims to develop an operational map that graphically shows how operating variables affect the steady operation of the DFB.

In addition to an investigation on the solid hydrodynamics of the primary material representing sand in the dual fluidized bed (DFB), there is also a need to include a secondary bed material, representing char. This is because during the gasification process, char is generated almost instantly when biomass is fed into the gasifier and devolatilized (Biagini et al., 2009). The bed material is now a binary mixture consisting of two different types of material (sand and char). It has been reported that the hydrodynamics of a DFB is affected by the addition of a secondary component. The following review is presented for existing studies on the hydrodynamics of binary mixtures.

2.5.2 Hydrodynamics of Dual Fluidized Beds with Binary Mixture

The use of two different types of materials, especially materials that represent a mixture of sand and char in a DFB, is not commonly found. Both studies by Goo et al. (2008) and Charitos et al. (2010) in a DFB use only one type of bed material. Documentations on binary mixtures mostly focused on the mixing efficiency of the two types of materials in the CFB riser or BFB. For example, the mixing characteristics of Geldart Group D particles in a BFB were investigated by Rasul & Rudolph (2000). It was found that there was an operating boundary at which the binary mixture segregated. During segregation, the small, heavy particles settle at the bottom of the bed, and are called jetsam particles. The big, light particles float to the surface of the bed, and are known as flotsam particles. The boundary drawn between segregation and mixing is useful to prevent segregation of the binary mixture, which would lead to a drop in combustion efficiency in a BFB combustor (Rasul & Rudolph, 2000).

Similar work was done by Jang et al. (2010) who characterized the mixing index of the binary mixture in a BFB. In their study, the BFB was divided into separate layers and each layer was first removed carefully for screening and sieving tests. The mixing degree was then determined by measuring the weight fraction of each type of solid material in each layer.

In a separate study, Sau et al. (2008) investigated the hydrodynamics of binary mixtures in a tapered BFB. Sau et al. (2008) argued that with a tapered BFB (that is, with the diameter expanding up the height of the BFB in the gas flow direction) the fluidizing gas velocity reduces so that the rate of loss of bed material out of the BFB due to entrainment in the gas flow decreases. This would increase the gas flow capacity of the BFB, allowing a higher operating velocity for the system. A new correlation was developed for predicting the minimum fluidization velocity of the binary mixture in relation to the taper angle of the BFB.

A study by Chen & Wen (1982) found that an increase in fraction of secondary material, representing biomass in the bed mixture, decreased the pressure drop for a given total solids inventory. This was because of a reduction in the effective density due to an increase in the fraction of less dense secondary material. It was the aim of this study to perform the binary mixture test for different solids inventory to determine the effect on solids circulation and pressure drop through the DFB.

From the review of the studies above, there is a lack of work on the effect of adding a secondary material on the hydrodynamics of the dual fluidized bed. The studies by Rasul & Rudolph (2000), Jang et al. (2010) discussed above were only focused on the mixing characteristics of the binary mixture in a BFB, and did not look at the effect of the binary mixture in the entire DFB system. The study by Sau et al. (2008) was concerned with the minimum fluidization velocity for different BFB taper angles, effective density and particle size of the binary mixture, once again ignoring the effect on the hydrodynamics of the entire system. The effect of binary mixtures on the hydrodynamics of a DFB cold model including both CFB and BFB, is pursued in this work.

2.6 Computational Fluid Dynamic Modeling of Cyclone Separators

Cyclones are used for separating particulates from the gas stream and are used in various industrial applications (as mentioned in Chaper 1) due to their design simplicity, low manufacturing and maintenance costs (Azadi et al., 2010). After the gas and solid enter the cyclone, they swirl downwards. At a certain height within the conical region,

the gas reverses direction and flows upwards and through the vortex finder, which is essentially the exit point of the cyclone. Overall, the gas flow forms a precessing vortex core (PVC) flow structure, with the vortex core swaying from side to side. This behaviour of the precessing vortex core is the source of unsteady state behaviour of the gas flow in the cyclone. The particles are thrown outwards towards the wall due to centrifugal forces induced by the swirling flow. These particles hit the cyclone wall and fall downwards at the wall due to gravity. However, due to the precessing vortex core, there will be certain entrainment of particles from the dense layer of particles in the wall region into the upward flowing core. The amount of particles that are entrained into the gas stream is consequently related to the aforementioned gas and particle fluid dynamics (Cortés & Gil, 2007).

The study of the flow behaviour of the gas and solids in the cyclone has been performed widely using computational fluid dynamics (CFD) with the recent advancement in computational capabilities. CFD is a method used to analyze the fluid flow in various systems, and is based on a complex set of equations and numerical algorithms (Blazek, 2005; Versteeg & Malalasekera, 2007). In literature, there are different modelling considerations in CFD for the flow behaviour in the cyclone, such as the number of elements required to obtain an accurate solution, the choice of the turbulence model for the gas phase, or the appropriate model for the gas-solid flow phenomenon.

For instance, there was a large degree of variation in the grid size used by various workers using CFD for circulating flow fields in a cyclone, ranging from 29000 to 450000 grid nodes for laboratory scale cyclones (Wan et al., 2008; Xiang & Lee, 2008; Jiao et al., 2007; Karagoz & Kaya, 2007). Derksen (2003) used as many as 7.7×10^{6} elements in the grid for the simulations with Large Eddy Simulation (LES) as the turbulence model.The size of the discretizing time step for running the simulations also varied, with Derksen (2003) using a time step of 1×10^{-5} s, while Wan et al. (2008) used a value 1×10^{-4} s. No information was given about the time step used by Xiang & Lee (2008), Jiao et al. (2007), and Karagoz & Kaya (2007).

For modelling the gas-solids flows, one of the available approaches is the Eulerian-Eulerian model (or simply the Eulerian model), which is used to simulate flows

with high concentration of particles. In this model, both the gas and the solid phases have their own governing equations and are treated as inter-penetrating phases with source terms in both sets of equations to represent interactions due to drag, for example. This method requires a relatively high computational cost. This disadvantage has limited the application of Eulerian models in cyclone simulations (Utikar et al., 2010), and have prompted the use of another gas-solid modelling approach, which is known as the Eulerian-Lagrangian (or Lagrangian) model.

The Lagrangian model predicts the particle trajectories by integrating the Newton's equations of motion (Utikar et al., 2010). There are two Lagrangian approaches in treating gas-solid flows. First is the one-way coupling model, where the solid volume concentration or solid fraction is low, and the flow condition is dilute. The motion of the solid phase is assumed to not influence the gas flow. The second Lagrangian approach is the two-way coupled or fully-coupled method, where the motion of the particulate phase does influence the gas flow when the solid fraction is high enough (Utikar et al., 2010).

The exact solid fraction at which the one-way or two-way coupled Lagrangian model is chosen varies in the literature (Derksen, 2003; Cortés & Gil, 2007; Cui et al., 2010). Cui et al. (2010) invoked two-way coupling at a solid volume concentration of 5.4×10^{-5} at the inlet, while Utikar et al. (2010) suggested 1×10^{-3}. It should be noted that two-way coupled Lagrangian model is known to cause numerical instabilities, and an under relaxation factor has to be applied (Derksen et al., 2008).

The work from Cui et al. (2010) revealed that particles would stagnate on the conical wall of the cyclone, causing high erosion rates. The region most susceptible to erosion found by Cui et al. (2010) is different from that observed in the CFB cyclone of CAPE gasifier, as described in Chapter 1, where the region of highest erosion was found near the inlet. Nevertheless, a preliminary study to investigate the impact of the particles on the erosion on the cyclone was performed.

The review of the work in the literature shows that the CFD is a powerful tool to model the flow in a cyclone. However, there are considerable variations in the numerical approaches taken reported in the literature, such as the choice of discretizing grid size and time step. It is not clear what is the most suitable modelling approach for the cold model cyclone. Thus, it is the aim of this study to determine a suitable modelling

approach and develop a CFD based design tool for the cyclone. The modelling approach in the design tool is validated by experimental results cited from literature. The modelling approach is applied to the cold model cyclone, after which further validation is carried out using experimental data collected in this work.

2.7 Overall Summary

An operational map of the CFB riser plant with relation to the effect of CFB and loop-seal airflow rates has not been found in the literature. Therefore, an operational map relating the operating variables to the regions where the CFB riser operates in a steady state was investigated. Following the work from Yan et al. (2005), a suction probe is used to measure the local solid flux and determine the solid volume fraction due to its relative simplicity and reliability. Measurements of the solids outflow have been performed in literature, and this study will follow a similar method used by Charitos et al. (2010). The effect of an abrupt exit on the solid outflow and downward solid flow rate near the wall has not been investigated widely (Richtberg et al., 2005). Therefore, part of the work in this thesis is to thoroughly examine the effects of the exit geometry and the aerodynamic effects on the solid outflow from the CFB riser.

Type I hydrodynamic models of the CFB riser have been used to predict the axial solid fraction distribution due to their simplicity (Berruti et al., 1995; Pallarés & Johnsson, 2006). However, Type I hydrodynamics models contain several parameters or correlations that are fitted to experimental results (Senior & Brereton, 1992; Schoenfelder et al., 1996; Gungor & Eskin, 2007). These parameters and correlations may not be applicable generally to other CFB systems with different design or operating conditions. A critical assessment of several correlations in the literature (Geldart et al., 1979; Colakyan & Levenspiel, 1984; Tanaka et al., 1972; Adánez et al., 1994; Johnsson et al., 1991; Babu et al., 1978; Lewis et al., 1949) is performed by comparing the predicted results with experimental measurements. Any discrepancies is discussed.

It is reported that the inclusion of the solids frictional pressure drop can overpredict the pressure drop in the transport zone (Nakamura & Capes, 1973). The pressure drop due to solids acceleration is also reported to be negligible in the upper regions of the

riser (Nieuwland et al., 1997). In developing a hydrodynamic model in this work, the contribution from frictional forces and solids acceleration are neglected for predicting the pressure drop.

There are studies on the DFB which focused on the solids mass flow rate or flow regimes, but these studies did not provide an operational map to demonstrate regions of steady operation of the plant (Goo et al., 2008; Charitos et al., 2010). Therefore, an operational map is developed in this study to denote the boundaries for steady state operation of the DFB. The hydrodynamics of the dual fluidized bed with binary mixtures are not common in the literature. Most other studies are related to segregation or mixing efficiencies, the influence on the minimum fluidization velocity, or the effect on the pressure drop for a constant solids inventory (Rasul & Rudolph, 2000; Chen & Wen, 1982; Jang et al., 2010). Therefore, another objective in this study is to focus on the addition effect of secondary material on the hydrodynamics of the DFB.

There are different considerations for CFD modelling of a cyclone, such as the discretizing grid size and time step, which have been found to be differing in literature (Wan et al., 2008; Xiang & Lee, 2008; Jiao et al., 2007; Karagoz & Kaya, 2007; Derksen, 2003; Cui et al., 2010). This study thus focuses on the development of a design tool for the cold model cyclone, which aims to clarify the modelling approach for the cold model cyclone.

Chapter 3

Investigation of Solids Circulation in a Cold Model of a Circulating Fluidized Bed

Chapter 2 has reviewed the experimental work on the CFB risers found in literature, and it was found that the operational map of a CFB riser, the aerodynamic effects and riser exit width effect on the solid circulation rate has not been investigated extensively. The measurements of these variables and their relation with each other are essential for better understanding of the hydrodynamics of the CFB riser. A design tool can then be formulated to estimate the solid circulation rate.

The experimental investigation in this chapter focuses on Phase I of the project, and is limited to only the CFB riser, cyclone, and loop-seal. The loop-seal is connected to the bottom section of the riser, instead of the BFB, to replenish the riser solid inventory. Besides an operational map for steady state operation of the CFB riser, the work documented in this chapter proposes a correlation for the aerodynamic factor (defined in Section 3.3.5), and relates the solid circulation rate with the exit geometry. The results will show that the correlation links the effect of solid concentration to the aerodynamic factor, which in turn affects the amount of solid flowing out of the CFB riser.

3.1 Introduction

As mentioned in Chapter 1, fluidized beds are used with the gasification technology to produce a mixture of volatile gases that can be further used as gaseous fuels, or it can be synthesized to produce liquid fuels. Fig. 3.1 shows a diagram of a dual fluidized bed (DFB) gasification plant, which consists of a circulating fluidized bed (CFB) combustor and a bubbling fluidized bed (BFB) gasifier. The cold model of the DFB gasification plant in this study is shown in Fig. B.1 in Appendix B. The process starts with the gasification of biomass with superheated steam in the BFB, producing a mixture of combustible gases that flows into a cyclone and then out of the plant for utilization as syngas or as gaseous fuel. The bed material in the BFB (sand, and solid char) flows through a chute to the riser of the CFB. Hot primary air is passed into the bottom of the CFB riser for the combustion process, which produces heat and flue gas, primarily N_2, CO_2, excess O_2 and H_2O. The bed material in the riser now consists of sand, leftover char and small amounts of ash. This is continuously conveyed to the CFB cyclone where it is separated from the flue gas. A secondary flow of hot air in the CFB riser injected at a certain height from the bottom aids the upward transport of solids into the cyclone thus reducing the primary airflow rate required, so that by-pass of primary air into the BFB via the chute is avoided (Löffler et al., 2003). Limiting the primary airflow rate also creates a sub-stoichiometric region below the secondary air injectors, which reduces NO_x emissions (Ersoy et al., 2004). The hot flue gas flows out of the system from the top of the CFB cyclone. The bed material flows from the bottom of the cyclone, down to a standpipe and into a loop-seal. The loop-seal functions as a seal to prevent BFB producer gas from mixing with the CFB flue gas. It also functions as a non-mechanical valve, returning the bed material to the BFB to provide heat for sustaining the biomass gasification process.

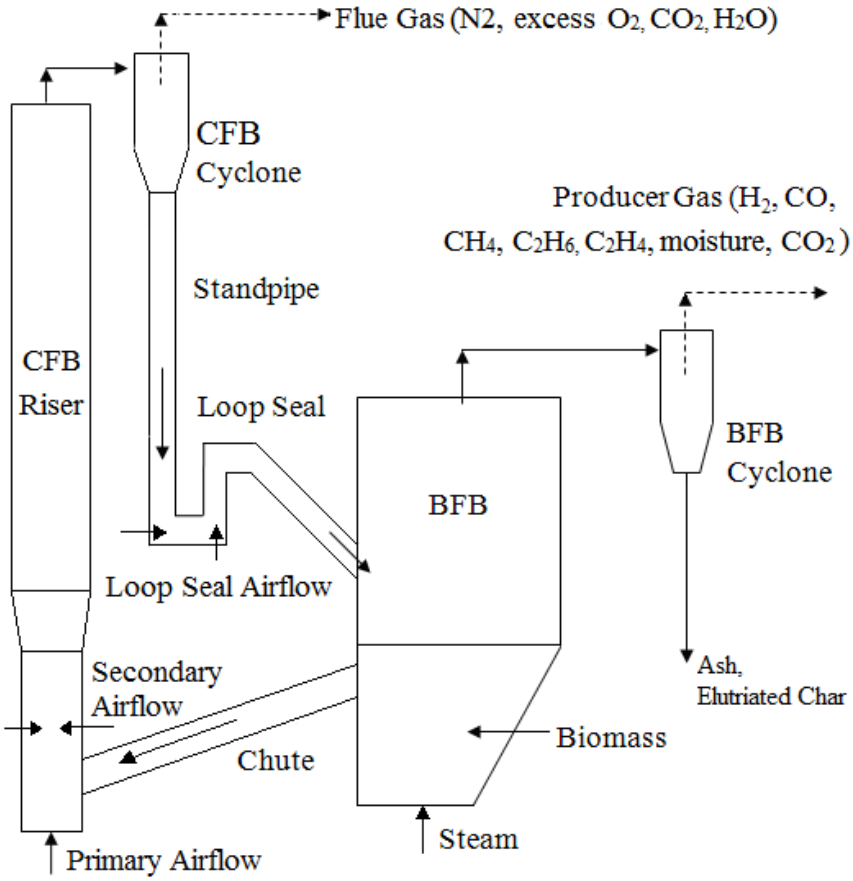

Fig. 3.1: Flow diagram of a dual fluidized bed (DFB) gasification plant.

The factors affecting the operational performance of the DFB gasification plant have been identified. The solids mass flow rate through the loop-seal needs to be controlled carefully to prevent BFB producer gas from by-passing into the CFB cyclone via the loop-seal and standpipe. As by-pass flow represents a loss in producer gas, it would induce a drop in efficiency of the gasifier. Furthermore, as the solids carry heat needed by the steam gasification reactions, the solids mass flow through the loop-seal affects the reaction rates within the BFB and hence the production of producer gas. Another variable of importance is the recirculation rate of solids within the CFB riser. The solids flow in the riser shows a core-annular structure, with a dilute upward flowing core of solids and a downward flowing layer along the annular wall layer (Davidson, 2000; Johansson et al., 2007). The annular-wall layer is first formed at the top of the riser generated by solids that do not exit into the cyclone, but instead impact on the roof and sides of the riser and flow back downwards at the wall. This annular wall flow increases with distance from the riser top, down the height of the riser as a portion of the solids

from the upward flowing core are carried radially outwards by turbulence and entrained into the downwards wall flow (Lackermeier et al., 2001; Harris et al., 2003; Mabrouk et al., 2008). In CFB combustors or incinerators, water is converted to steam inside heat-exchanger tubes that line along the walls. The rate at which solids are transferred to the walls of the riser therefore affects the steam conversion rate (Johansson et al., 2007; Gnanapragasam & Reddy, 2009). The solids flow in the annular wall layer has also been documented to cause erosion of the wall (Johansson et al., 2007). Yet another important parameter is the pressure drop over the riser, which is related to the solids fraction in the riser. When the pressure drop becomes too low, it is likely that the riser has been exhausted of bed material (Smolders & Baeyens, 2001; Schlichthaerle & Werther, 1999). This may indicate blockage in the chute, which is preventing solids from passing through into the riser.

The measurement of solids recirculation within the CFB riser and solids flow into the BFB will provide information useful for determining appropriate operating conditions that maximize both gasification efficiency and producer-gas production. However, the measurement of the solids mass flow in an industrial gasification plant is difficult, because normal operating temperatures are between 700 and 900°C, making sampling procedures unsafe. Therefore, a cold model of the system operating at ambient temperatures is commonly constructed to investigate the effect of gas flow rate on the solids mass flow and other hydrodynamic parameters.

In this study, experiments on a cold model of a CFB combustor has been designed, constructed, and tested to elucidate factors that affect the hydrodynamics of a gasification plant. In particular, the phenomenon of solids recirculation within the CFB riser is focused upon, and a new semi-empirical model is presented to predict the fraction of solids that exit the riser into the cyclone, and the fraction that re-circulates back down the riser at the wall. The cold model was a scaled down version of the CFB combustor of an existing 8MW_{th} DFB gasification plant located in Güssing, Austria (Löffler et al., 2003; Kaiser et al., 2003; Proll et al., 2009). The cold model was made almost entirely of polycarbonate to allow the solids flow to be visualized. Air at ambient temperature was used as the fluidization medium. Measurements taken include riser pressure drop, loop-seal solids mass flow and solids recirculation rates within the riser.

Based on the pressure drop measurements and visual observations of the solids flow, a map of stable operating conditions was developed to provide a guide for determining suitable gas flows and mass flow circulation rates when operating circulating fluidized beds. The BFB was not incorporated into the cold model in this part of study (Phase I) so that attention could be focused on the hydrodynamics of the CFB. The BFB has been added in Phase II studies and will be presented in Chapter 5.

3.2 Materials and Methods

3.2.1 Cold Model Plant Description

Fig. 3.2 shows the cold model plant of the CFB, which is geometrically similar to the CFB of the dual fluidized bed (DFB) gasification plant in Güssing, Austria (Löffler et al., 2003; Kaiser et al., 2003). The diameter of the riser is 180 mm at the base and the total height is 2.60 m. The system has primary air with volumetric flow rate Q_{pri} flowing through an air distributor plate at the bottom of the riser to fluidize the solid particles. The air distributor plate has 32 evenly spaced nozzles that protrude up into the riser by 50 mm, and each nozzle has 12 orifices that are spaced 15 mm apart. Secondary air with volumetric flow rate Q_{sec} is injected at 0.20 m above the distributor plate to provide additional airflow to convey the particles out of the riser. A diffuser, located 0.50 m above the distributor plate, expands the diameter of the riser to 210 mm to reduce the air velocity. The reduction in air velocity allows re-circulation of solids within the riser via downward flow of solids in the annular region of the wall (Schut et al., 2000; Löffler et al., 2003). Solids exit through a square opening (width and height of 0.70 m) near the top of the riser at the wall and enter a cyclone where the solids are separated from the air. From the cyclone bottom, the solid particles drop down to a standpipe and then to the loop-seal, while air flows out through the top of the cyclone. Any entrained particles in the out flowing gas are collected in a bag filter. Loop-seal aeration with volumetric airflow rate Q_{ls} is provided via three taps in the sides of the loop-seal.

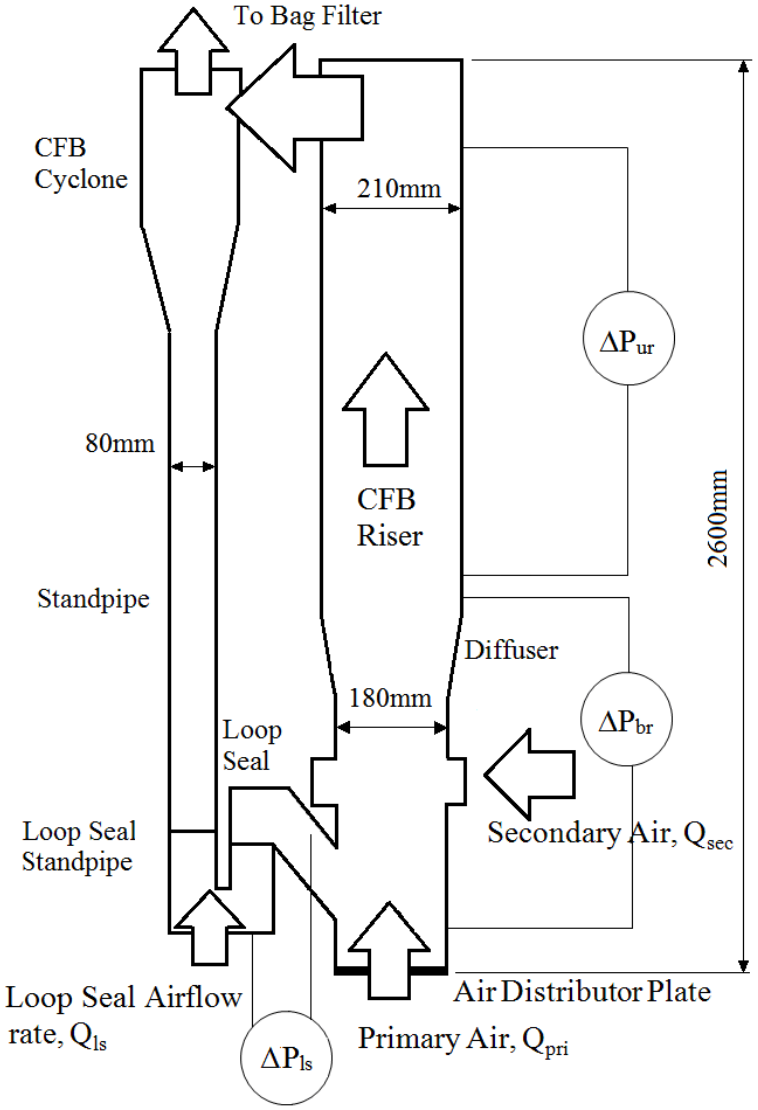

Fig. 3.2: Flow diagram of the cold model of a CFB.

3.2.2 Scaling Laws for the Cold Model

Scaling laws have been used to find an appropriate bed material in the cold model and to determine operating conditions that would result in dynamic similarity between the cold model and the dual fluidized bed (DFB) gasification plant in Güssing. According to Farrell (1996), the following dimensionless parameters should be maintained to be similar during scaling of a gasifier to achieve dynamic similarity: the density ratio (De), the Archimedes number (Ar), the flow number (Fl), and the dimensionless solid circulation rate, G^*. These dimensionless parameters are defined as follows:

$$De = \frac{\rho_g}{\rho_s} \tag{3.1}$$

$$Ar = \frac{(\phi d_p)^3 \rho_g (\rho_s - \rho_g) g}{\mu_g^2} \tag{3.2}$$

$$Fl = \frac{u_o}{u_{mf}} \tag{3.3}$$

$$G^* = \frac{G_s}{\rho_s u_s} \tag{3.4}$$

A gas density of 0.3 kg/m^3 is common in an industrial gasifier which is operated at high temperatures (Proll et al., 2009) and sand as inert bed material has a density of 2500 kg/m^3. In order to maintain the same density ratio De for the cold model operated at ambient temperature (with air density of 1.18 kg/m^3), copper particles of density 8940 kg/m^3 were selected. The copper particles were supplied by Metal and Steel Corporation (Taiwan), and had a particle size d_p of 138 μm and were irregular in shape with a circularity factor, ϕ of 0.60. This resulted in an Archimedes number in the cold model of 163, which is close to the Archimedes number of 171 in the industrial plant. The flow number Fl is 35 in the gasification plant at Güssing (Kreuzeder et al., 2007). In the current investigation, the flow number ranges from 16 to 46. The dimensionless solids circulation rate G^* for the Güssing plant (Kreuzeder et al., 2007) and the current work is 0.0028 and 0.0006. Based on process requirements, the solids circulation of the Güssing plant can be reduced by a factor of one-third, making the dimensionless solids circulation rate similar to the cold model in this work (Pfeifer et al., 2009). Medium density polyethylene (MDPE) can replace the char in the cold model. The hydrodynamics of the binary mixtures in the cold model was investigated and presented later in Chapter 5.

Note that the particle circularity is calculated from the equation

$$\phi = 4\pi \frac{A}{P^2} \tag{3.5}$$

where the perimeter P and cross-sectional area A are obtained from analysis of microscopic images of the particles (Fu et al., 2006; Raub et al., 2008; Barry et al., 2009;

Prakongkep et al., 2010).

3.2.3 Experimental Procedures

By observing the solids flow within the CFB for a range of different primary, secondary and loop-seal airflow rates, an operational map was drawn to determine the range of stable operating conditions outside which the solid flow is either highly unsteady or there is no solids circulation at all. In this experiment, the cold model was operated up to maximum primary, secondary, and loop-seal airflow rates of 157 m^3/h, 320 m^3/h, and 10 m^3/h, respectively.

The solids mass flow rate from the riser into the standpipe, $\dot{m}_{so}$ was measured by cutting off the airflow to the loop-seal to prevent solids from moving through the loop-seal, and then measuring the solids accumulation rate in the standpipe over a period of time (normally in the vicinity of 10 s). The height change in the standpipe was converted to a mass using the measured bulk density of the powder and the cross-sectional area of the standpipe. In this experiment, the primary airflow rate was varied from 32 to 96 m^3/h while keeping the secondary and loop-seal airflow rates constant at 171 and 6 m^3/h respectively. The experiment was repeated for different bed inventories (effectively the total amount of solids in the system) of 6, 8, and 10 kg in the riser. A separate experiment to investigate the influence of the secondary airflow rate on the solids flow was performed by varying the secondary airflow rate from 107 to 320 m^3/h for a range of different primary airflow rates. The bed inventory was fixed at 10 kg for the secondary airflow rate experiment, while the loop-seal airflow was maintained at 8 m^3/h.

Radial profiles of solids flux in the core-flow region of the riser were measured by iso-kinetic sampling at different heights up the riser (0.95, 1.55, 2.55 m above the distributor plate) and for various primary airflow rates ranging from 32 to 96 m^3/h while maintaining the secondary airflow and loop-seal airflow rates at 171 and 6 m^3/h respectively. Iso-kinetic sampling was achieved using a suction probe of diameter 5 mm connected to a particle separator to collect the solids. The suction velocity was set equal to the gas velocity measured at the same sampling location using a Pitot tube. In fact, Grace et al. (1997), Davidson (2000) and Schut et al. (2000) have found that the suction

velocity does not affect the solids collection rate when the particle inertia is sufficiently high, as is the case in this work. A sensitivity analysis on the suction velocity for values ranging from 90 to 150% of the suction velocity required for iso-kinetic sampling has confirmed this finding in the work presented here. Particles were collected for two minutes to achieve good statistical averages of the solids flux. The solids flux was calculated by dividing the mass of solids collected by the cross-sectional area of the suction probe and the time for collection. The solids volume fraction at each radial position was determined by dividing the solids volumetric flow rate (mass of solids collected divided by the particle density and collection time) by the sum of the solids volumetric flow and air-suction volumetric flow rate, which was measured by a rotameter. At each radial position, three repeating measurements of the solids flux and solids fraction were taken and averaged. The uncertainties on the solids flux and solids fraction measurements were estimated as the standard deviation of three values. The radial solids flux profiles at a given riser height were integrated over the cross-sectional area of the riser to determine the total mass flow rate in the core, $\dot{m}_{core}$ at that axial location. The experiment was repeated for three different amounts of bed material (or bed inventory) of 6, 8 and 10 kg in the riser to investigate the effect of mass loading on the solids flow in the riser. An experiment was also conducted to determine the effect of loop-seal airflow rate on the solids core flow rate in the riser.

The downward annular wall flux of solids in the riser, G_w was measured by fixing a 3 mm diameter tube with the opening facing next to the inside wall of the riser at a height of 2.5 m above the distributor plate (opposite to the riser exit) to collect particles that flowed downwards. The particles flowed down by gravity into a bottle (sealed from the external environment) located outside the riser. The annular wall solid flux was calculated by the mass of particles collected over a given time divided by the cross-sectional area of the tube and the time for collection. This measurement was conducted to examine the effect of primary, secondary and loop-seal airflow rates on the recirculation rate of solids within the riser. It may not be an accurate measurement of the annular-wall flux, which is difficult to measure due to the uncertainty of the thickness of the annular wall-flow, the velocity of the particles, and the intrusive effect of the collection probe.

To investigate the effect of the opening width of the exit port at the top of the riser on the solids mass flow, two obstruction plates were placed in the opening to reduce its width from 70 mm to 50 and then to 30 mm, respectively, while the height of the opening was kept constant at 70 mm. For each obstruction plate, the bed inventory in the riser was 10 kg. The primary and secondary airflow rates were maintained constant at 53 m^3/h and 171 m^3/h respectively, while the loop-seal airflow was kept at 8 m^3/h.

Pressure drops were measured over various points in the plant. The fluidized bed consists of two zones: a dense zone at the bottom section of the riser where the solids fraction is high, and a transport zone in the upper section of the riser where the solids fraction is lower. The pressure drop over the CFB riser bottom section, ΔP_{br}, was measured across two pressure taps located at heights of 0.10 m and 1.00 m above the distributor plate, as shown in Fig. 3.2. It was observed visually that the dense zone was always below 1.00 m for the tested range of primary airflow rates, and therefore this height was chosen as the location of one of the pressure taps. The second pressure tap was located 0.10 m above the distributor plate rather than at the bottom of the distributor plate to avoid any interference from high-velocity jets issuing horizontally from the nozzles on the air distributor plate. The pressure drop in the upper section of the CFB riser, ΔP_{ur}, was measured with two taps located at heights of 1.00 m and 2.30 m above the distributor plate. The pressure drop across the weir of the loop-seal ΔP_{ls} was measured across the points shown Fig. 3.2. These points were chosen to provide an indication of the effect of loop-seal airflow on the amount of solids in the weir section of the loop-seal. Note that the pressure taps were mounted flush against wall at all locations, and the pressure drops, measured using differential-pressure transducers, were time averaged with fluctuations used to estimate uncertainty. In these experiments, the primary airflow rates was varied from 32 to 96 m^3/h with a constant secondary airflow rate of 171 m^3/h. At each primary airflow rate, the loop-seal airflow rate was varied from 5 to 9 m^3/h.

3.3 Results and Discussion

3.3.1 Operational Map

Fig. 3.3 shows the operational map developed in this study which shows different operation regimes of the cold model CFB plant at a loop-seal airflow of 8 m^3/h. There were limits on the maximum primary and secondary airflow rates possible, which are marked as "operating limit" in Fig. 3.3. In Region A, there was no fluidization, because the primary gas velocity was below the minimum fluidization velocity, u_{mf}. Hence, there was no circulation of solids through the plant. In Region B, the superficial velocity in the dense zone exceeded the minimum fluidization velocity, however steady riser operation was not achieved due to a combination of two effects: 1) the bed did not expand sufficiently into the secondary airflow injection zone to allow sufficient elutriation into the transport zone and 2) slugging occurred in the dense zone. The slugging phenomenon has also been observed by Zijerveld et al. (1998), Bi et al. (2000), and Makkawi & Wright (2002) in circulating fluidized bed plants operated at just above minimum fluidization. In Region D, the total gas velocity (primary plus secondary airflow rates) was between the minimum fluidization and the particle terminal velocities. Although the solids were fluidized, no particles were entrained upwards in the riser. Region E is the elutriation regime, where the gas velocity was just above the particle terminal velocity, u_t. In this operating region, solids in the transport zone were dilute, and there was low solids circulation through the system. Particulates near the top exit of the riser formed ropes that followed streamlines out through the exit and into the cyclone. Near the bottom of the riser, a splash zone existed above the dense bed of material, where bursting bubbles at the surface of the bed resulted in violent eruptions with particle clusters being flung upwards and some falling back downwards.

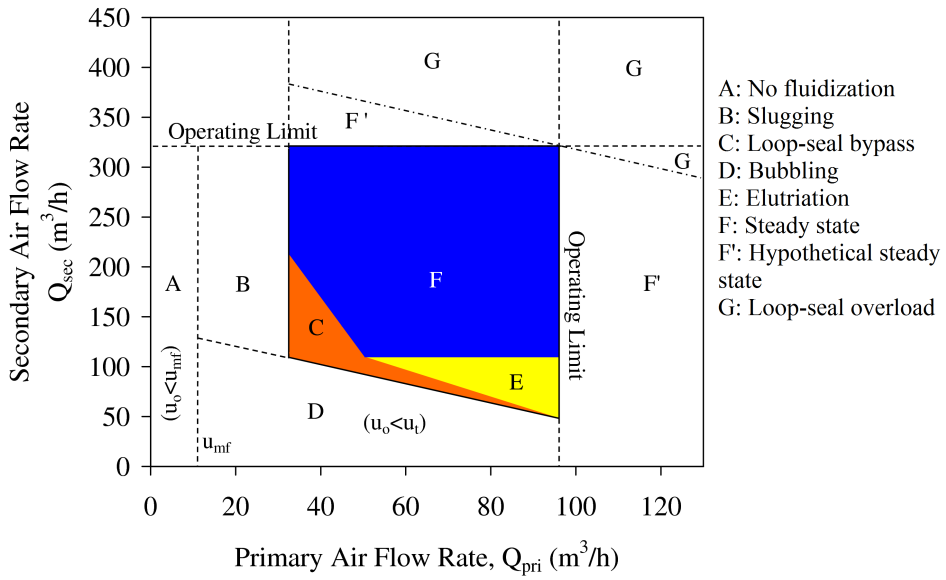

Fig. 3.3: Operational map at loop-seal airflow of 8 m^3/h.

In Region F, solids moved freely up and out of the riser, down through the cyclone into the standpipe, and back into the riser via the loop-seal. The splash zone observed in Region E was not evident in Region F. Instead, dense clusters of particles continued to move upwards in the core. In contrast to Region E, clusters of particles flowed downward at the wall. This annular solids flow at the wall occurred in sporadic waves, which formed and disintegrated at random. A portion of the downward flowing solids was re-entrained into the upward flowing core. This non-uniform unsteady downward annular solids flow was also observed by Davidson (2000) and Senior & Brereton (1992). The solids concentration at the wall was high relative to the core region, and the core flow was often obscured from view. Note that many published mathematical models of CFB risers assume that solids are uniformly distributed in the downward flowing annular wall layer (Rhodes et al., 1992; Namkung & Done Kim, 1998; Johansson et al., 2007). This has not been observed in the experiments presented here.

In Region G, the total airflow rate (primary and secondary) resulted in significantly more mass exiting the riser than could be supplied to the riser via the loop-seal, so that the loop-seal became overloaded and solids accumulated within the standpipe. In fact, this phenomenon was only observed at a single point close to the operating limit when the primary and secondary airflow rates were 96 and 320 m^3/h, or the total airflow was 416 m^3/h. We speculate that any combination of primary and secondary airflows for

which the sum is greater than 416 m^3/h would result in overloading in the loop-seal. It was observed that the loop-seal fluidization became unsteady when the loop-seal became overloaded, as occurred in Region G. Region F' is a hypothetical region where the plant should also operate in a steady manner. However, due to the limitations of the current equipment, the airflow rates could not be sufficiently high to verify this. In Region C, the plant was still operating in a steady manner; however the gas seal was compromised. At the low primary and secondary airflows of Region C, the solids flow up the riser was low, and the relatively high loop-seal airflow of 8 m^3/h was sufficient to cause the height of material in the loop-seal standpipe to decrease to a level where gas from the riser could by-pass through the loop-seal, up the standpipe and out the cyclone.

The operational map in Fig. 3.3 shows conditions where the CFB will operate at an optimum level, with a proper gas seal and sufficient solids mass flow rate. Note that there was a lower limit on the loop-seal airflow of 3 m^3/h. At this value, the superficial velocity was just above the minimum fluidization velocity, and it was observed that the flow of solids through the loop-seal was highly irregular. When the loop-seal airflow rate was above 3 m^3/h, the loop-seal bed was fluidized well, and the flow of solids through the loop-seal was smooth and steady. Furthermore, when the bed inventory was increased above 10 kg, slugging fluidization occurred in the bottom and upper sections of the riser, and the plant became unstable. This occurred because the pressure drop over the height of the bed became high relative to the pressure drop over the distributor plate, so that non-uniform airflows through the nozzles of the distributor plate developed, which resulted in channeling of the airflow and unstable fluidization (Svensson et al., 1996). Thus, 10 kg was considered the maximum bed inventory for steady operation of the riser.

3.3.2 Effect of Primary and Secondary Airflow on Riser Solids Outflow Rate

The riser solids outflow rate was measured by cutting off the loop-seal airflow and measuring the accumulation of solids in the standpipe. The results are shown in Figs. 3.4 and 3.5 show that the riser solids outflow rate increases with primary and secondary airflow rates for a given riser bed inventory. Thus, both the primary and secondary

airflows are key operational parameters for controlling the solids circulation through the system. Fig. 3.4 also shows that the riser solids outflow rate increases as the bed inventory increases from 6 to 10 kg for a given primary airflow rate, which indicates that the hold-up of solids in the riser also affects the solids circulation rate, which has been demonstrated by Goo et al. (2008). As explained previously, the inert bed material acts as a heat transfer medium in an industrial gasifier, and therefore the circulation rate of these solids is important for controlling the gasification rates of the biomass. A physical explanation for the increase in solids circulation rate with increasing primary and secondary airflows and bed inventory will be given below in the light of various pressure drop measurements presented.

In industrial dual fluidized bed gasification plants, such as shown in Fig. 3.1, appropriate primary, secondary and loop-seal airflow rates must be chosen to avoid gas by-pass from the BFB to the riser cyclone via the loop-seal, which occurs when there is a significant reduction in loop-seal solids. In the cold model investigated in this work, combinations of primary and secondary airflows that allow gas bypass from the riser into the standpipe are given by Region C in Fig. 3.3. Increasing primary and secondary airflow rates will allow the loop-seal to be replenished at a sufficient rate to maintain the seal, which will shift the operation from Region C into the stable operating Region F as shown in Fig. 3.3. Primary and secondary flow rates in the riser of an industrial gasifier can be similarly adjusted to ensure the seal in the loop-seal is maintained, although other factors must be considered such as limiting the primary flow to the CFB riser to reduce NO_x emissions and avoid primary air bypass from the CFB riser into the BFB via the chute.

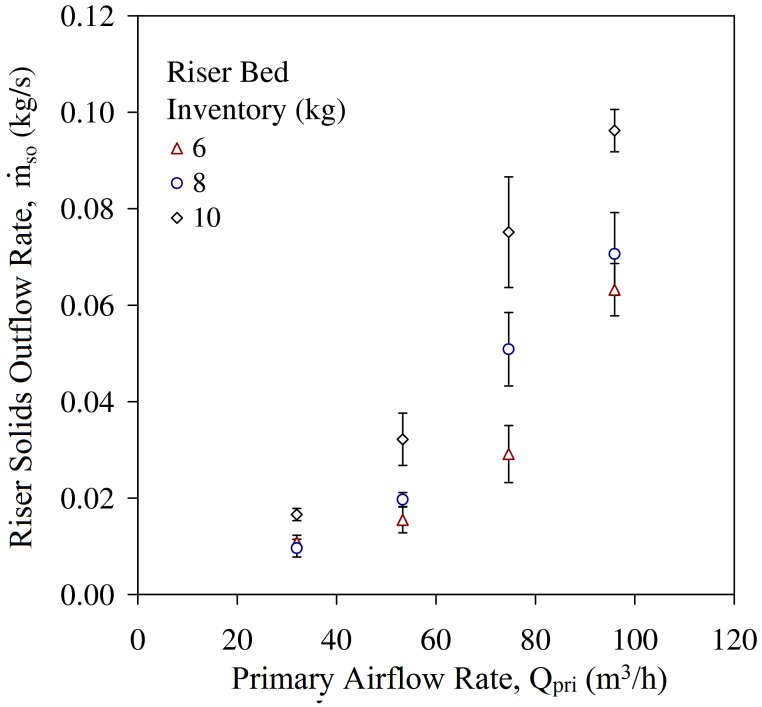

Fig. 3.4: Variation of riser solids outflow rate ($\dot{m}_r$) with primary airflow rate (Q_{pri}) for different bed inventories (secondary airflow (Q_{sec}) constant 171m^3/h; loop-seal airflow rate(Q_{ls}) of 6 m^3/h).

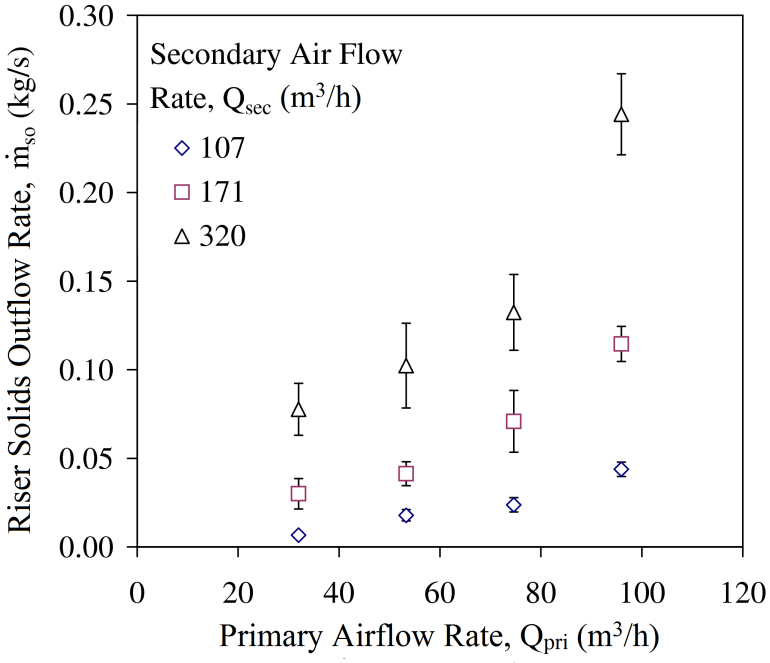

Fig. 3.5: Variation of riser solids outflow rate ($\dot{m}_r$) with primary airflow rate (Q_{pri}) for different secondary airflow rates (Q_{sec}) (loop-seal airflow rate (Q_{ls}) of 6 m^3/h; constant bed inventory of 10 kg).

3.3.3 Axial and Radial Profiles of Solids Mass Flux within the Riser

The axial and radial profiles of the solids flux and the solids fraction within the core region of the riser are presented in Fig. 3.6. In this case, the plant is operating in Region F of Fig. 3.3. The profiles are essentially parabolic in shape (validated by additional measurements as shown in Appendix C), with the maximum upward solids flux at the center and a negligible upward solids flux close to the wall. The decrease in the solids flux up the height of the riser indicates that particles are transported radially by airflow turbulence towards the wall, where they are entrained into the downward flowing layer near the wall. This effect has also been observed by Richtberg et al. (2005), Hahn et al. (1995), and Schlichthaerle & Werther (1999). Fig. 3.6 shows that higher solids fluxes and hence higher solids mass flows occur at higher primary airflow rates, which confirms the results presented in Fig. 3.4. The solids fraction in the core region of the riser also increases with primary airflow rate, as shown in Fig. 3.6.

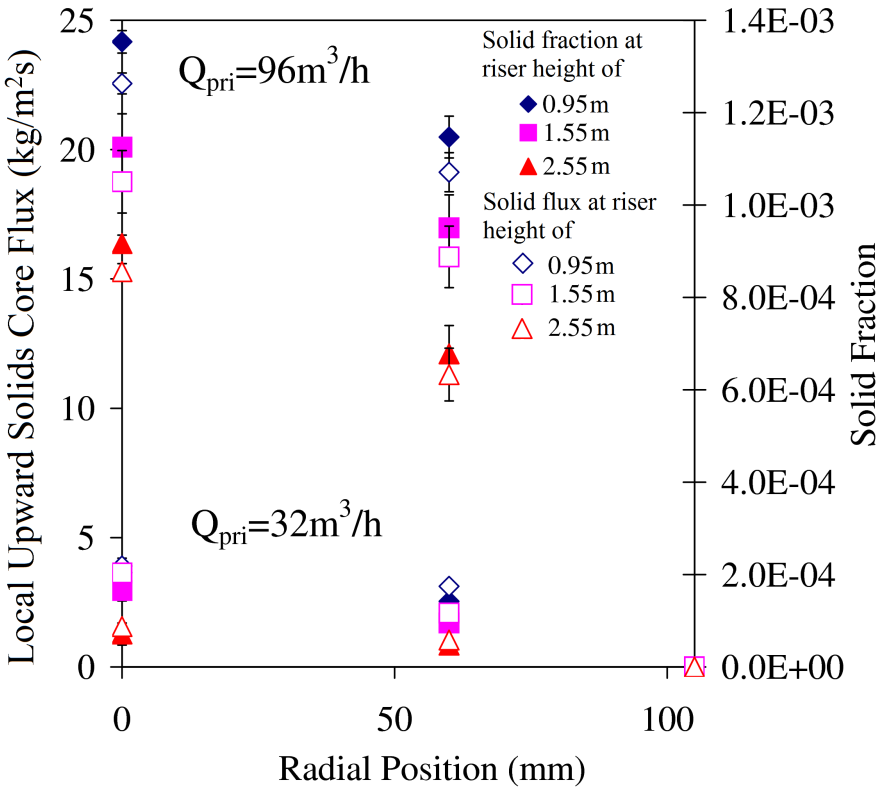

Fig. 3.6: Radial profiles of local solids flux and solids fraction in the riser for two primary airflow rates (secondary airflow rate (Q_{sec}) 171 m^3 /h; loop-seal airflow rate (Q_{ls}) 6 m^3/h; bed inventory 10 kg). Note the solids fraction as indicated by the dashed lines are read from the right hand side Y-axis.

Fig. 3.7 shows the effect of primary airflow rate on the riser solids core flow rate at a height of 2.55 m. This graph is derived by integrating the flux profile shown in Fig. 3.6 over the cross sectional area of the riser. Fig. 3.7 once again shows that the mass circulation rate increases with increasing primary airflow rate. In addition, the mass circulation rate increases as the bed inventory increases from 6 to 10 kg for a given primary airflow rate, which shows that solids hold-up also affects solids circulation rates, as stated earlier. Fig. 3.8 shows that an increase in loop-seal airflow rate results in a modest increase in the solids core flow rate in the riser. As the loop-seal airflow rate is increased, the fluidized bed in the loop-seal expands and material is shifted from the loop-seal into the riser. This has the same effect as increasing the bed inventory in the plant, as shown in Fig. 3.4. An explanation for this phenomenon will be given in the light of pressure drop measurements further on in the paper.

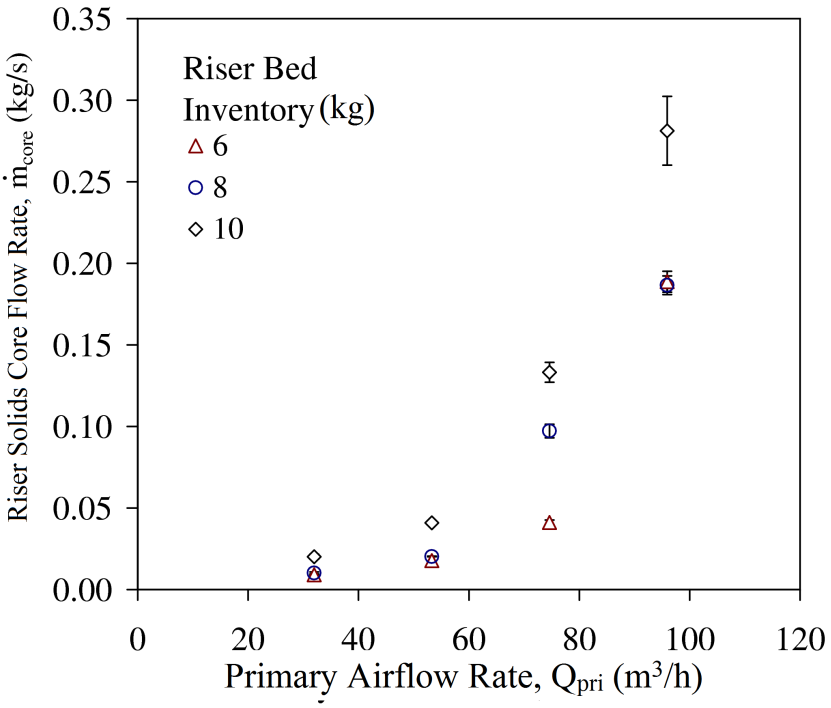

Fig. 3.7: Riser solids core flow rate at a height of 2.55 m up the riser for different primary airflow rates (Q_{pri}) and bed inventories (secondary airflow rate (Q_{sec}) 171 m^3/h, loop-seal airflow rate (Q_{ls}) 6 m^3/h).

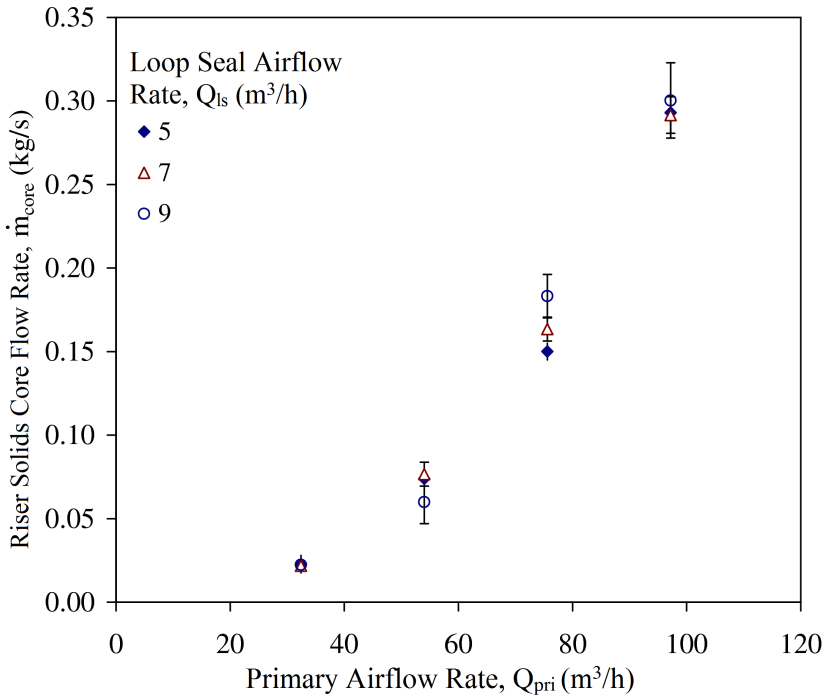

Fig. 3.8: Riser solids core flow rate at a height of 2.55 m up the riser height for different primary airflow rates (Q_{pri}) and loop-seal airflow rates (Q_{ls}) (secondary airflow rate (Q_{sec}) 171 m^3/h, bed inventory 10 kg).

3.3.4 Effect of Primary Airflow Rate on Annular Wall Solid Flux

As discussed above, both the solids mass flow rate within the riser and the exit solids flow rate from the riser increase as the primary airflow rate is increased. Fig. 3.9 shows that the downward annular wall solid flux also increases with increasing primary airflow rate, which implies that solids recirculation within the riser has increased. Thus, primary airflow rate is an important parameter for controlling the transport of both heat and mass within the riser of an industrial gasifier. Similar to the solids core flow rate, an increase in loop-seal airflow rate results in a modest increase in annular wall solid flux, as shown in Fig. 3.9, which is caused by a small shift of solids from the loop-seal into the riser. The effect of secondary airflow on the annular wall solid flux was not determined in this work. Given that an increase in either primary or secondary airflow results in a total increase in airflow above the secondary airflow injection point, and observing the trend of increasing riser solids outflow rate with both increasing primary and secondary airflows shown in Figs. 3.4 and 3.5, respectively, it is reasonable to assume that an increase in annular wall solid flux would also occur with increasing the secondary airflow.

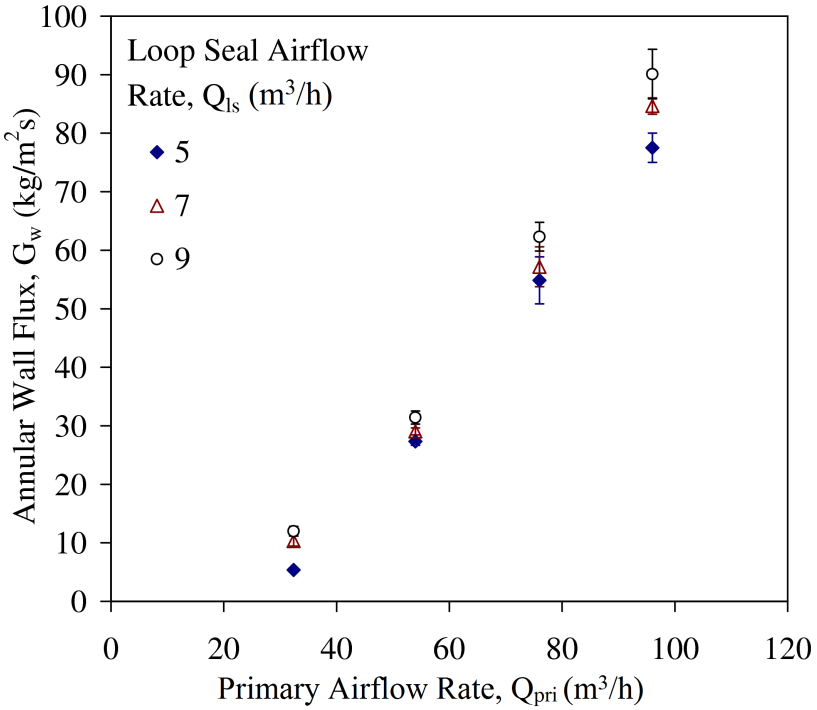

Fig. 3.9: Annular wall solid flux (G_w) at a height of 2.55 m up the riser for different loop-seal airflow rates (Q_{ls}) and primary airflow rates (Q_{pri}) (secondary airflow rate (Q_{sec}) 171 m^3/h, bed inventory 10 kg).

3.3.5 A Semi Empirical Model for Solids Flow out of the CFB Riser

A comparison of Figs. 3.4 and 3.7 shows that the riser solids outflow rate, $\dot{m}_{so}$ is lower than riser solids core flow rate, $\dot{m}_{core}$ for any given set of primary, secondary and loop-seal airflows. It was observed visually that not all of the solids that reach the top of the riser exit out into the separator cyclone. A fraction of the solids flows back down to form an annular layer at the wall. The proportion of solids that are re-circulated depends on the inertia of the particles at the top of the riser and the solids concentration. Fig. 3.10 shows a model to explain the mechanism of recirculation of solids at the top of the riser. In this model, particles impact on the ceiling of the riser and uniformly disperse in the radial direction. The fraction of particles that exit the riser into the cyclone is equal to the ratio of the opening width w to the riser circumference πD. Therefore, the mass flow rate of particles that exit the riser $\dot{m}_{so}$ can be estimated as

$$\dot{m}_{so} = (\frac{w}{\pi D})\dot{m}_{core} \tag{3.6}$$

where $\dot{m}_{core}$ is the mass flow rate of particles in the core close to the top of the riser. However, visual observations have indicated that this model is inaccurate when the particles have low inertia (at low primary and secondary airflows) and low concentrations. In this case, it has been observed that the particles do not impact on the ceiling of the riser. Instead, as they approach the top of the riser, they cluster together to form ropes that follow airflow streamlines through to the exit. The ratio of the mass flow rate of particles that exit the riser to the mass flow rate of particles in the core close to the top of the riser then becomes significantly higher than $w/\pi D$. Visual observations suggest that, in this limiting case, most of the particles that reach the top of the riser will exit into the cyclone, that is $\dot{m}_{so}$ / $\dot{m}_{core}$ is close to unity when the primary and secondary airflow rates are low.

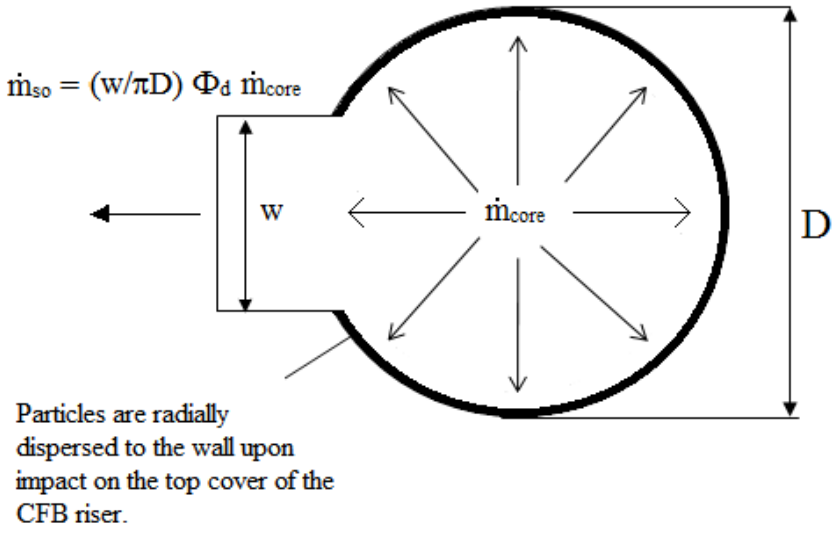

Fig. 3.10: Graphical depiction of particle dispersion and the effect of opening width on the riser solids outflow.

To take this effect into account, an aerodynamic factor, Φ_d has been included in the model, as follows

$$\dot{m}_{so} = \Phi_d(\frac{w}{\pi D})\dot{m}_{core} \tag{3.7}$$

In this model, when the inertia and concentration of the particles are high, particles are less influenced by the change in direction of the airflow as it curves towards the exit of the riser. The inertia of the particles is sufficiently high so that the particles continue flowing upwards, impacting against the ceiling of the riser and dispersing radially

outwards. In this limiting case, the aerodynamic factor Φ_d becomes unity. At the opposite extreme, when the inertia and concentration of the particles are relatively low, majority of the solid particles that reach the top of the riser exit into the cyclone, because the particles have insufficient inertia to resist the change in direction of the airflow towards the exit. In this case, the aerodynamic factor Φ_d approaches $\pi D/w$, or $\Phi_d(w/\pi D)$ is close to unity.

The data shown in Fig. 3.4 and Fig. 3.7 have been used to determine the value of the aerodynamic factor Φ_d for a range of different operating conditions (primary, secondary and loop-seal airflow rates) and bed inventories. The aerodynamic factor has been plotted against the radially-averaged solids fraction close to the top of the riser as shown in Fig. 3.11 for which it has been found that the aerodynamic factor decreases with increasing solids fraction at the top of the riser for all bed inventories tested and over a range of primary and secondary airflows. When the solids fraction is low, the aerodynamic factor Φ_d approaches a value of $\pi D/w$, which implies that all particles reach the top of the riser and exit through to the separator cyclone. In this case, it was observed that the particles form dense ropes close to the exit that appear to follow streamlines in the airflow out through the riser opening. As the solids fraction increases, the aerodynamic factor decreases, it would approach a value of unity if the solid concentration was high enough, which implies that the mechanism of impact and radial dispersion most significantly affects the outlet flow of particles.

All the experimental points appear to lie on a single curve, regardless of the bed inventory or primary, secondary and loop-seal airflows. A correlation has been fitted to the experimental data using the limits of $\pi D/w$ at low solids fraction and unity at very high solids fraction, as follows:

$$\Phi_d = (\frac{\pi D}{w} - 1)exp(-a\overline{\varepsilon}_{s,core}) + 1 \tag{3.8}$$

where $\overline{\varepsilon}_{s,core}$ is the radially-averaged solids fraction in the core of the riser close to the riser exit. In this correlation, the coefficient a takes on a value of 3668 which gives an R^2 value of 0.8327. Note that some of the aerodynamic factor values derived from experimental data are more than $\pi D/w$ at low concentrations, which implies that more mass has exited the riser than arrived at the top of the riser, which is physically

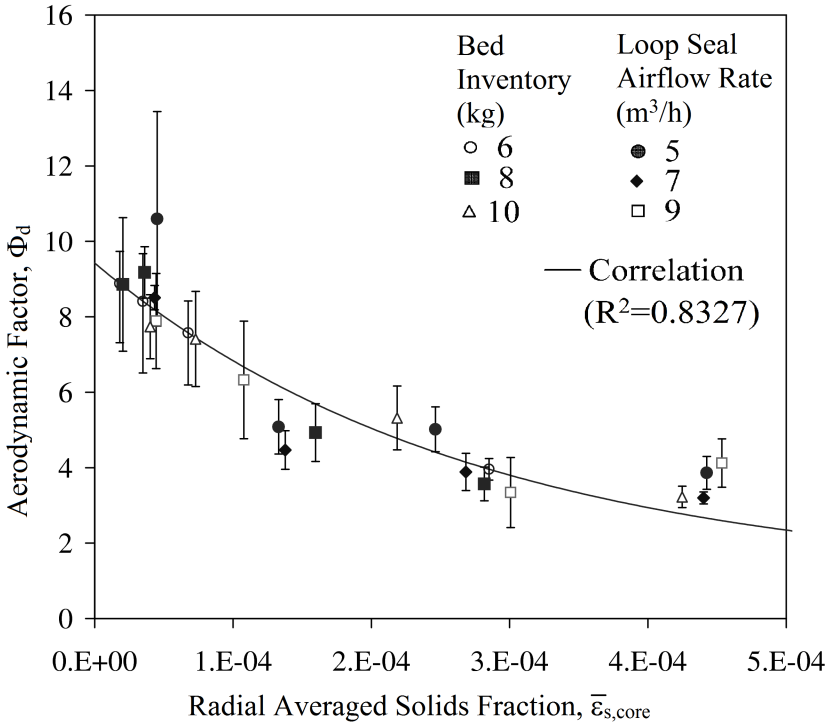

Fig. 3.11: Aerodynamic factor as a function of the radially-averaged solids fraction at a height of 2.55 m up the riser for different bed inventories and loop-seal airflows.

unreasonable. Firstly, the riser exit solids mass flow and the mass-flow of particles at the top of the riser could not be measured simultaneously, because the loop-seal airflow had to be shut off to measure the riser solids outflow rate. Secondly, there were modest fluctuations in virtually all measured variables with time, even in the so-called stable operating region, as indicated by the error bars in the solids-flux profiles shown in Fig. 3.6. These fluctuations were due to the erratic ejection of particles by bursting bubbles from the dense zone in the riser bottom section, and the random formation of ascending and descending clusters.

The width of the exit port of the riser, which allows solids to pass through into the cyclone, was changed in order to test the validity of the model presented diagrammatically in Fig. 3.10. When the solids fraction is sufficiently high such that the aerodynamic factor approaches unity, then it can be expected that the reduction in width of the exit port would result in a proportional reduction in solids mass flow into the cyclone. Fig. 3.12 shows that the solids flow out of the circulating fluidized bed decreased in proportion with the reduction in the opening width for a given primary and secondary airflow. In fact, a reduction in the exit width by a factor of 2.5 resulted in a

decrease in the solids flow that exits the riser by a similar factor of 2.7, which lends support to the validity of the model presented diagrammatically in Fig. 3.10.

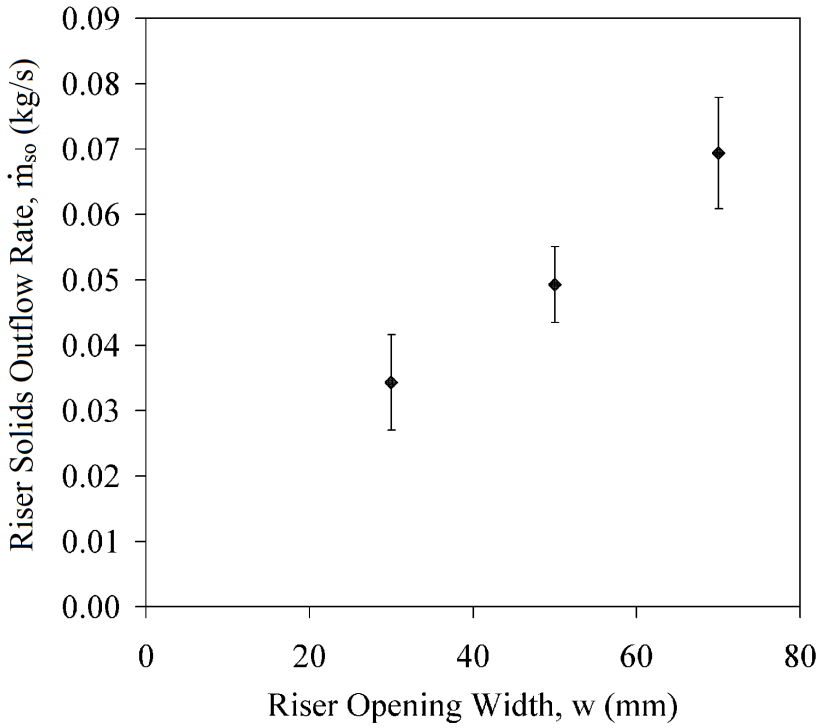

Fig. 3.12: Variation of riser solids outflow rate ($\dot{m}_{so}$) with exit width (bed inventory of 10 kg; primary airflow rate 53 m^3/h; secondary airflow rate(Q_{sec}) 171 m^3/h).

3.3.6 Pressure Drop Measurements

Figs. 3.13, 3.14 and 3.15 show the results of pressure drop measurements for the riser bottom, upper sections and the loop-seal, respectively. The measurements were performed for operating conditions within Regions F and C of Fig. 3.3. Fig. 3.13 shows that the pressure drop in the riser bottom section ΔP_{br} decreases with increases in the primary airflow rate Q_{pri}, which is a result of the bed expansion and associated increase in voidage of the dense zone in the riser bottom section. The fluidized bed expansion also results in an increase in the solids fraction at the level of the secondary airflow injection ports, above which the solids are entrained upwards, which explains the increase in solids mass flow with increasing primary airflow rate as shown in Fig. 3.4. This is supported by Fig. 3.6, which shows an increase in solids fraction in the core of the transport zone as the primary airflow Q_{pri} is increased. Increasing the bed inventory also has the effect

of increasing the solids concentration at the level of the secondary airflow injection ports, which increases the solids mass flow rate, as demonstrated in Fig. 3.7. Increasing the secondary airflow rate effectively increases the solids velocity and hence solids mass flow rate, as shown in Fig. 3.5. The increase in pressure drop in the riser upper section ΔP_{ur} as Q_{pri} increases (Fig. 3.14) is due to the redistribution of solids from the dense zone into the riser upper section and the resultant increase in frictional losses from inter-particle and particle-wall interactions in this zone. Fig. 3.14 also includes the pressure drop over the riser upper section when there are no solid particles in the system for comparison with the pressure drop when the particles are present. The significant increase in pressure drop that occurs when the particles are present demonstrates the effect of pressure losses due to the drag force required to lift the particles upwards and frictional losses due to particle-particle/particle-wall interactions.

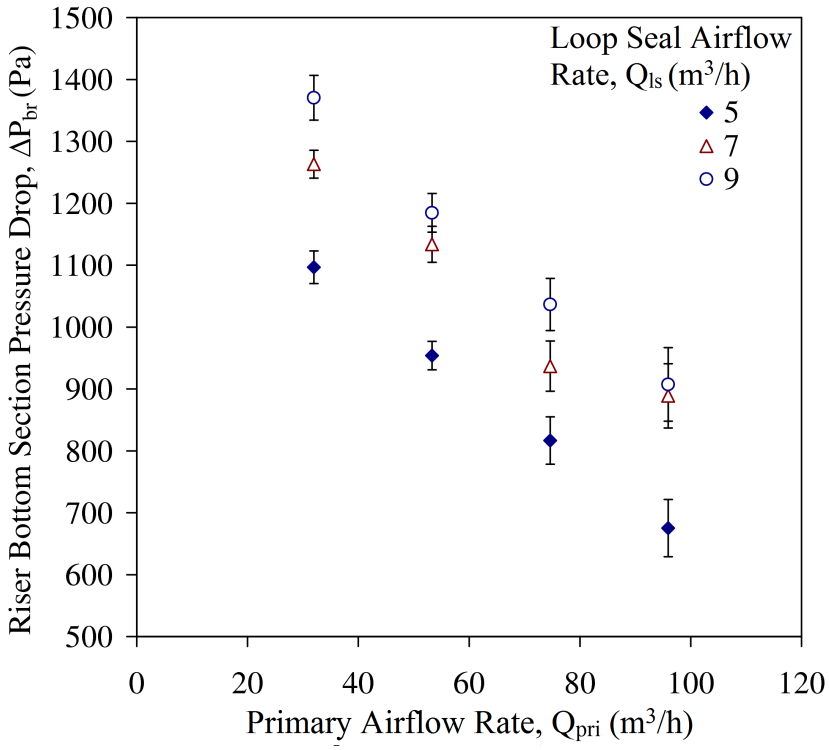

Fig. 3.13: Effect of primary airflow Rate (Q_{pri}) and loop-seal airflow rate (Q_{ls}) on riser bottom section pressure drop (ΔP_{br}) (bed inventory 10 kg; secondary airflow rate (Q_{sec}) 171 m^3/h).

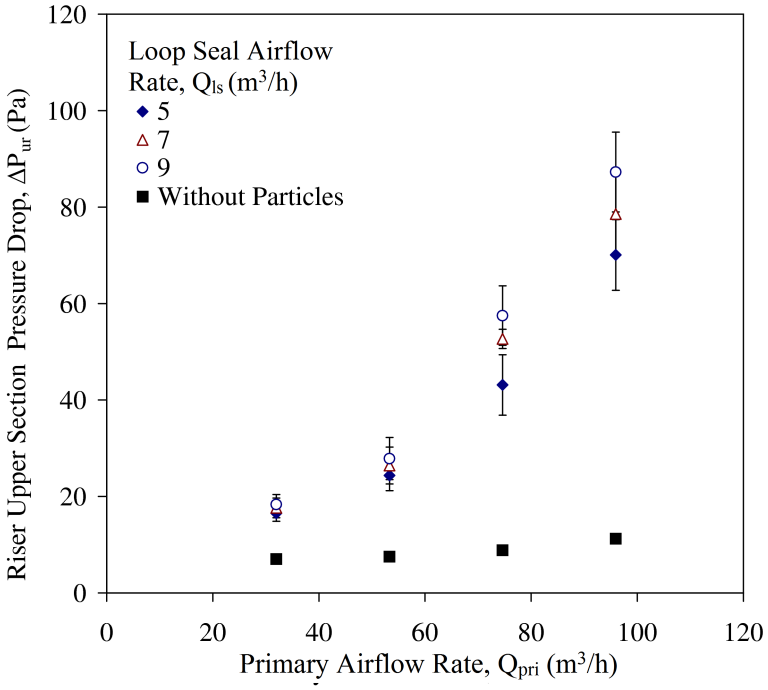

Fig. 3.14: Effect of primary airflow rate (Q_{pri}) and loop-seal airflow rate (Q_{ls}) on riser upper section pressure drop (ΔP_{ur}) (bed inventory 10 kg; secondary airflow rate (Q_{sec}) 171 m^3/h). Pressure drop in the riser upper section without solid particles is also included for comparison.

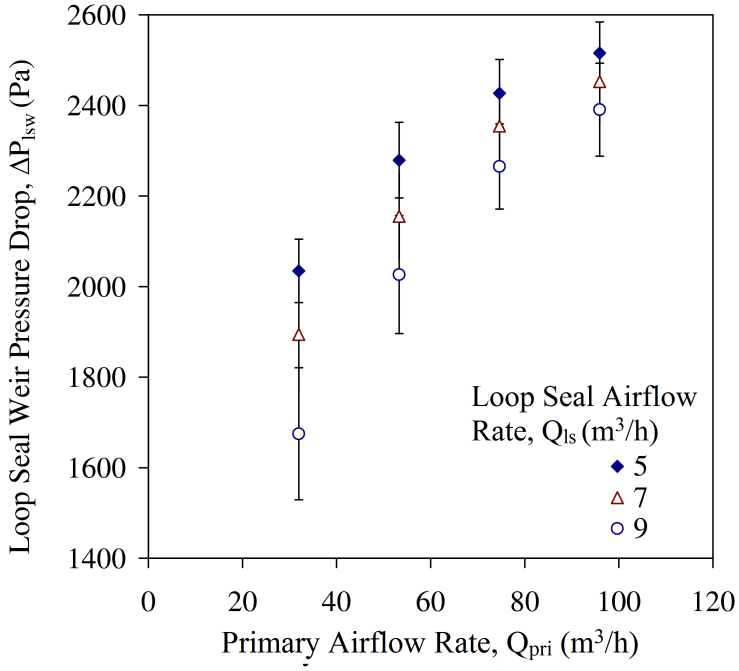

Fig. 3.15: Effect of primary airflow rate (Q_{pri}) and loop-seal airflow rate (Q_{ls}) on loop-seal pressure drop (ΔP_{ls}) (bed inventory 10 kg; secondary airflow rate (Q_{sec}) 171 m^3/h).

The loop-seal airflow rate has a significant effect on the pressure drops both in the riser bottom and the upper sections, and the pressure drop in the loop-seal, as shown in Fig. 3.13, 3.14 and Fig. 3.15. The loop-seal pressure drop ΔP_{ls} is a reflection of the amount of particles below the weir of the loop-seal. Fig. 3.15 shows that ΔP_{ls} decreases as the loop-seal airflow rate is increased. This is caused by the expansion and associated increase in voidage of the fluidized bed in the loop-seal, which effectively shifts the particles over the weir of the loop-seal and into the dense zone in the bottom section of the riser. The drop in loop-seal solids and accompanying rise of solids within the riser results in the increase in the pressure drops in the riser bottom and upper section as shown in Fig. 3.13 and 3.14, since more solids must be supported by the fluidizing airflow in the riser. The modest increase in riser solids core flow rate and downwards annular solid wall flow with increasing loop-seal airflow shown in Fig. 3.8 and 3.10 is due to the increase of solids in the riser. The increase in loop-seal pressure drop ΔP_{ls} with increased primary airflow rate Q_{pri} shown in Fig. 3.15 is due to the shift of solids from the riser into the loop-seal, caused by the increase in solids flow, as demonstrated in Fig. 3.4.

Changes to the primary, secondary or loop-seal airflow rates within Region F cause redistribution of solids within the plant. Within Region F, the steady-state always adjusts to the new operating conditions as regulated by the loop-seal, which behaves as a typical S-shaped bend. Thus, an increase in primary or secondary airflow rates increases the solids mass flow out of the riser as well as the solids recirculation within the riser, as shown in Figs 3.5 and 3.7. Provided that the loop-seal is fluidized properly by the loop-seal airflow, the mass flow of solids through the loop-seal increases automatically to equalize the pressure across the loop-seal. If the loop-seal airflow rate is too high and the riser solids outflow rate is too low due to low primary and secondary airflows, the loop-seal can become depleted of solids to the extent that a proper gas seal is no longer maintained. This would result in bypass of primary air through the loop-seal, up the standpipe and out the CFB cyclone. In this case, the CFB plant operates in Region C of Fig. 3.3. This must be avoided in an industrial gasification plant with a coupled CFB riser and BFB, such as shown in Fig. 3.1, because such bypass would represent a loss of producer gas.

3.4 Conclusions

A circulating fluidized bed (CFB) cold model (Phase I) has been designed and constructed in this part of the study. Experiments have been carried out on the cold CFB model in order to investigate the effects of various operating parameters on solids circulation within the system. An operational map has been developed based on flow visualizations and using solids mass flow rate and pressure drop measurements to differentiate between different fluidization regimes. This operating map shows the limits for stable operation of the circulating fluidized bed system. Outside these limits, various unstable operating conditions occur, such as highly unsteady fluidization and circulation of solids, an overloaded loop-seal, or loop-seal bypass. In the stable operating region, increasing the primary and secondary airflows has the effect of increasing the solids circulation rate through the system and solids recirculation within the CFB riser. The same effect can be observed by increasing the total amount of solids in the system, although the maximum amount of solids possible is constrained by the weight that can be properly supported on the distributor plate during fluidization. For stable operation, the loop-seal airflow rate must be sufficient to generate required fluidization of the loop-seal solids. However, the loop-seal airflow rate should not be too high to cause the loop-seal to become depleted of solids, which would result in bypass of air from the riser. The loop-seal airflow rate has only a modest effect on solids circulation in the system.

A new model has been proposed to estimate the ratio of solids that exit the riser to solids that flow in the core of the riser. In this model, high solids concentration and high velocities represent the condition in which solids inertia dominates. Thus, the solids are unaffected by the change in airflow direction towards the riser exit. Instead, they impact on the ceiling of the riser and disperse radially and evenly outwards. The fraction that exits the riser to the upward flowing solids is equal to the ratio of the riser exit width to the circumference of the riser. The opposite extreme condition is low solids concentration and low velocities. In this case, the solids have insufficient inertia to resist the change in airflow direction towards the riser exit. They cluster together to form ropes that follow streamlines out through to the riser exit. Thus, majority of the upward flowing solids exit from the riser.

The pressure drop over various points in the circulating fluidized bed has been measured. The pressure drop in the riser bottom section decreases with increasing primary airflow rate, due to an increase in the dense zone voidage and expansion of the bed into the vicinity of the secondary flow injectors. This allows more solids to be carried up to the riser upper section, and therefore there is a corresponding increase in the pressure drop in the riser upper section as well as an increase in overall solids circulation rate within the system. The loop-seal airflow rate also affects the pressure drop across the riser bottom and upper sections, due to a shift in material between the loop-seal and riser.

Chapter 4

Critical Assessment of Hydrodynamic Models for the CFB Riser

The original plan of this part of the work was to validate Type I hydrodynamic models using experimental data measured with the cold CFB model. Type I models are used to predict the axial solid fraction, the solids mass flow rate and the pressure drop in the riser of a CFB (Harris et al., 2003). However, it became quickly apparent during this work that Type I models suffer from a lack of generality since they are largely empirical in nature, and in most cases the models were fitted to experimental data from a particular system. However, when these models are used in different systems or conditions, significant errors may be observed. In this chapter, this lack of generality is exposed by comparing the predictions of different Type I models with the experimental data collected in Chapter 3. It will be shown that there is a significant amount of physics that is not being properly captured by the simple empirical models. Some of the assumptions that accompany the model will also be assessed.

4.1 Introduction

In the operation and design of a CFB biomass gasifier, hydrodynamic models are very useful to predict flow parameters in the CFB riser such as the axial solid fraction, solids mass flow rate and pressure drop. The predicted results of these hydrodynamic parameters can be used for control of the plant stable operations and for improving the

energy efficiency of the gasification process. The modelling results can also be used for sensitivity analysis during scale up.

The hydrodynamic models reported in literature comprise of various combinations of correlations and equations, and these correlations are normally limited to a certain range of conditions because they have been developed on the basis of experimental data from one experimental setup, and have not been validated for use on other experimental setups. Due to the large variation between models, it is not clear which model is valid for a given experimental setup. The objective of this part of the research is to provide a critical evaluation of the various models available, in literature for prediction of hydrodynamic properties. This is assessed by comparing the measured hydrodynamic properties presented in Chapter 3 with the corresponding predicted properties from the models. The main parameters and correlations assessed are the dense zone voidage (ε_{dz}), the voidage at infinity (ε_{∞}), the associated elutriation rate (K_{∞}), and the decay constant (a_d). The discrepancies will be analyzed between the model predictions and the experimental results. Possible areas for future investigations are then identified to improve the predictive models.

Fig. 4.1 summarizes the main hydrodynamic parameters and related correlations that were used in the models. In Fig. 4.1 the dense zone stretches to a height H_{dz}, 0.18 m above the air distributor plate. The dilution point is the point just above the H_{dz} where the injected secondary air dilutes the flow. Above the dilution point is the transport zone, which is the start of an exponential decay of the solid fraction in the core region of the riser (Löffler et al., 2003). The solids fraction decays up the height of the riser because particles move radially towards the wall, carried by turbulence, and are entrained into a downward annular flow of solids at the wall. A diffuser is located at a height of 0.56 m above the air distributor plate to increase the backflow of solids down the annular wall above this height (Schut et al., 2000; Löffler et al., 2003). The exponential decay of solid fraction continues in this zone until the top of the riser. At this point, solids exit the riser and into an attached cyclone, as described in Chapter 3.

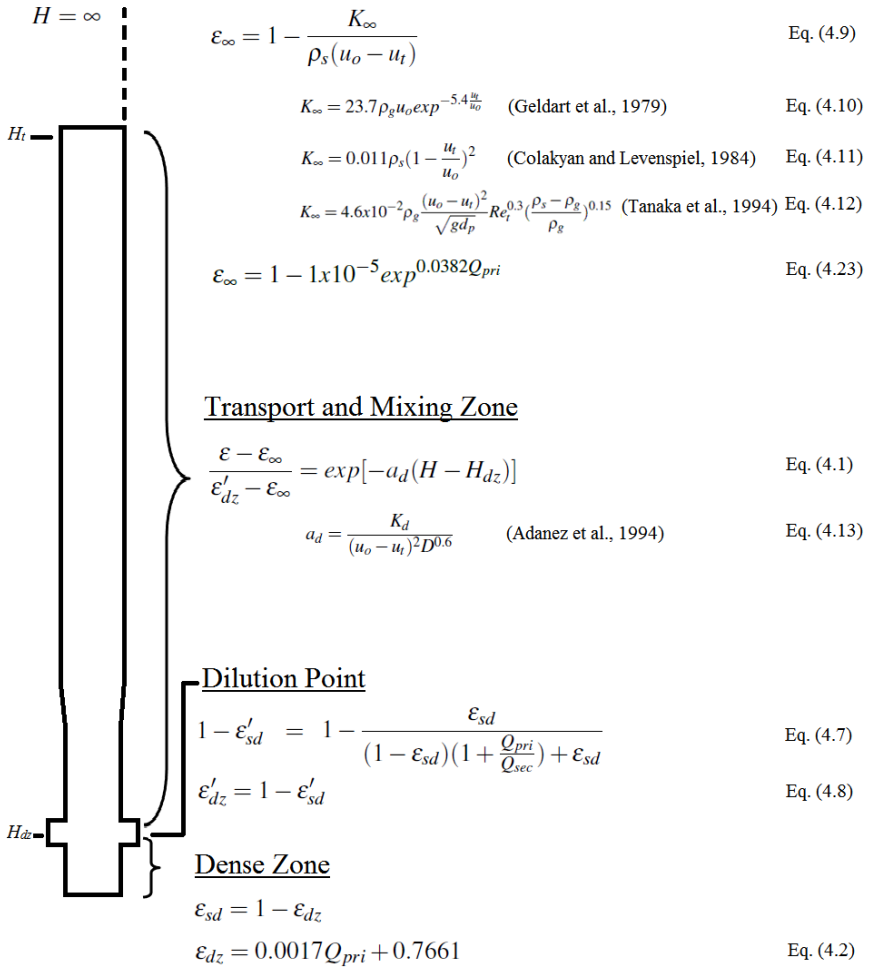

Fig. 4.1: List of equations assessed in this study for respective regions in riser

4.2 Theory and Assumptions

4.2.1 Modelling of Axial Distribution of Solid Fraction in the Riser

The solid fraction can be predicted by three different types of hydrodynamic model (Harris et al., 2003) which were presented in Chapter 2. Type I models only predict the axial solid fraction distribution. Type II models predict the axial and radial solid fraction distribution. Type III models, using fundamental conservation equations, can provide detailed fluid flow information throughout the riser. In this part of study, the Type I hydrodynamic models are assessed by comparing predicted and experimentally measured results of axial solid fraction at different heights in the CFB riser. The predicted solid fraction are used to predict the solids circulation rate and pressure drop in

the riser, and these predictions are then compared with experimental values presented in Chapter 3.

For Type I models, a solids mass balance over a short, discretized height element in the riser is established in order to develop an equation to predict the solids fraction in the riser core at any height (Kunii & Levenspiel, 1991). The flow rate of dispersed and clustered solids flowing upward in the centre of the riser as well as the solids flowing downward in the annular wall layers are considered in the mass balance. There is also an interchange of solids between the upward flowing solids in the core flow and the downward flowing solids in the annual layer, which is reflected by a decay constant, a_d, fitted from experimental data. The decay constant governs the decaying profile of the axial solid fraction along the riser height. After integration and considering the solid fraction at the dense zone height ($H = H_{dz}$ in Fig. 4.1) and at an infinite riser height ($H \longrightarrow \infty$) as the boundary conditions, the final form of the mass balance equation for the voidage fraction is given in Eq. (4.1), which can be used for prediction of the voidage in the core, as shown by Kunii & Levenspiel (1991),

$$\frac{\varepsilon - \varepsilon_\infty}{\varepsilon'_{dz} - \varepsilon_\infty} = exp[-a_d(H - H_{dz})] \tag{4.1}$$

where ε_∞ is the voidage (also called the void fraction) at an infinite height ($H = \infty$ in Fig. 4.1), ε'_{dz} is the voidage at the dilution point, ε is the average voidage in the riser core at a height of H in the transport zone, a_d is the decay constant that accounts for the interchange of solids between upward and downward flowing solids, and H_{dz} is the height from the bottom of the distributor plate to the top of the dense zone. The voidage (also called void fraction) is the fraction of gas volume flow rate over the total of gas and solid volume flow rate. Once the voidage is known, the solid fraction ε_s can be calculated as (1-ε), which is the radially averaged of the solid fraction in the riser core.

In deriving Eq. (4.1), it was assumed that the solid fraction in the riser decreases exponentially from the dense zone voidage at the top of the dense zone to a constant value equivalent to (1-ε_∞) at a certain height above this, known as the transport disengaging height (TDH). The solid fraction remains constant with height above TDH as there is no longer an axial concentration gradient (Kunii & Levenspiel, 1991), so there is no net driving force for solids to move radially towards the wall and be entrained into

a downward flowing annular wall layer. Indeed, the annular wall layer would vanish above this height, unless there is another source of solids for the annular wall layer, such as the riser top and exit interruption in the CFB riser, in which solids that do not exit the riser rebound off the ceiling of the riser and flow back down the wall. In using Eq. (4.1), the dense zone voidage, the voidage at the dilution point, the voidage at infinity, and the decay constant need to be determined separately which is discussed in the following sections.

To predict the dense zone voidage, the dense zone bed height is required. There are correlations in literature to predict denze zone bed height for a given distributor plate. For example, Babu et al. (1978), Lewis et al. (1949) and Johnsson et al. (1991) have developed correlations to predict bed height above perforated plate distributors. However, no correlation was found in the literature for the distributor plate used in this work, which consisted of a number of multi-orifice nozzles, as described in Chapter 3. Developing a general correlation that can be used for a nozzle type distributor plate would be difficult due to the complexity of the flows involved (Paiva et al., 2004). Therefore, a simple empirical model for the dense zone voidage was derived from experimental measurements of the dense zone bed height, and is shown in Eq. (4.2):

$$\varepsilon_{dz} = 0.0017 Q_{pri} + 0.7661 \tag{4.2}$$

In the experiments used to fit the coefficients for Eq. (4.2), the dense zone bed height was allowed to expand freely above the secondary air injectors without any secondary air flowing through. Under normal operating conditions, secondary air is injected, which dilutes the dense zone solids. Fig. 4.2 illustrates the dilution effect from the secondary airflow.

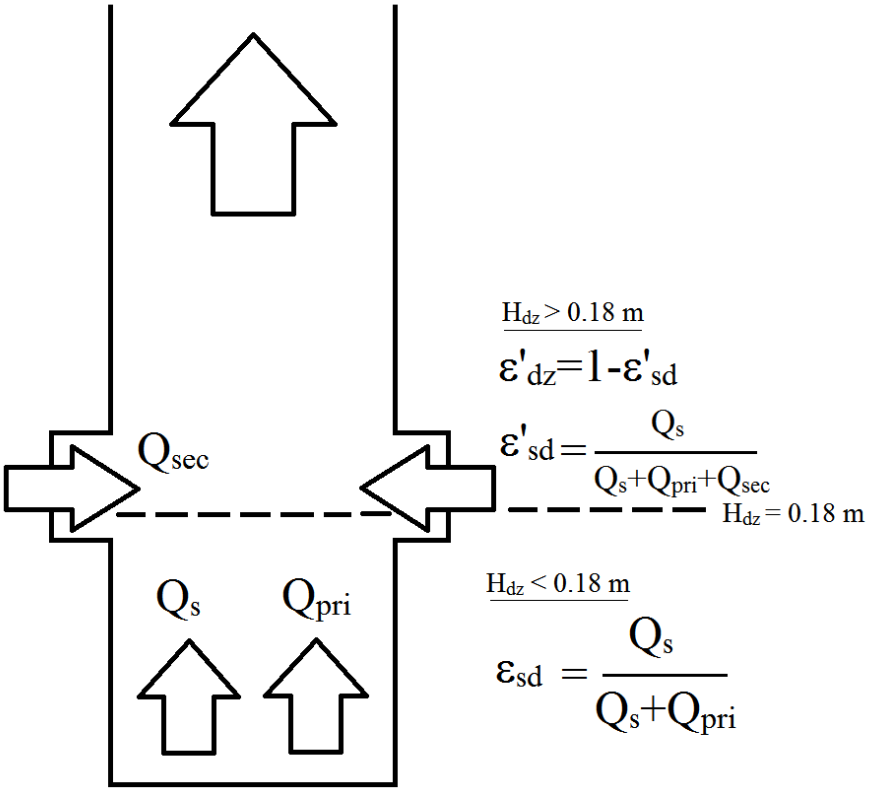

Fig. 4.2: Effect of secondary airflow diluting the dense zone solid fraction.

Fig. 4.2 shows that, in the dense zone below the secondary air injectors (H<0.18 m), both primary air and the solids are flowing upwards. The dense zone solid fraction ε_{sd} can be calculated from the dense zone voidage, ε_{dz} (ε_{sd} = 1- ε_{dz}) and can also be determined as

$$\varepsilon_{sd} = \frac{Q_s}{Q_s + Q_{pri}} \tag{4.3}$$

where Q_s is the solids volumetric flow rate, Q_{pri} is the primary airflow rate. Rearranging the above equations, the solids volumetric flow rate can be derived as a function of the dense zone solid fraction and the primary flow rate:

$$Q_s = \frac{\varepsilon_{sd} Q_{pri}}{(1 - \varepsilon_{sd})} \tag{4.4}$$

The inrush of secondary airflow dilutes the dense zone solids at the height of 0.18 m (Fig. 4.2), transporting the solids up the height of the riser. This is the end of the dense

zone, and is the start of the exponential decay of the solids fraction in the core (for H > 0.18 m). The solid fraction after dilution (ε'_{sd}) by the secondary airflow (Q_{sec}) is thus the flow of solids over the sum of the solids flow and primary and secondary airflows:

$$\varepsilon'_{sd} = \frac{Q_s}{Q_{pri} + Q_{sec} + Q_s} \tag{4.5}$$

Substituting Eq. (4.4) into Eq. (4.5) gives

$$\begin{aligned} \varepsilon'_{sd} &= \frac{\frac{\varepsilon_{sd} Q_{pri}}{1-\varepsilon_{sd}}}{Q_{pri} + Q_{sec} + \frac{\varepsilon_{sd} Q_{pri}}{1-\varepsilon_{sd}}} \\ &= \frac{\varepsilon_{sd} Q_{pri}}{(Q_{pri} + Q_{sec})(1-\varepsilon_{sd}) + \varepsilon_{sd} Q_{pri}} \end{aligned} \tag{4.6}$$

By dividing Eq. (4.6) by Q_{pri}, we have the final form of the solid fraction in the dilution point as:

$$\varepsilon'_{sd} = 1 - \frac{\varepsilon_{sd}}{(1-\varepsilon_{sd})(1+\frac{Q_{pri}}{Q_{sec}}) + \varepsilon_{sd}} \tag{4.7}$$

The dilution point, ε'_{dz}, can be calculated as follows

$$\varepsilon'_{dz} = 1 - \varepsilon'_{sd} \tag{4.8}$$

Eq. (4.8) is then used in Eq. (4.1) to predict the axial solid fraction in the transport zone.

In the CFB riser a diffuser was installed at a height of 0.56 m above the distributor plate. In this study, it was assumed that the enhanced backmixing of the solids caused by the diffuser did not affect the solids fraction in the core region of the riser. Due to this simplification, the solids fraction at the core before and after the diffuser was considered to be equal.

To use Eq. (4.1) for calculating the voidage in the CFB riser, the voidage at infinite height, ε_∞, is needed. This is related to the elutriation rate K_∞ (Kunii & Levenspiel, 1991; Bai & Kato, 1995) defined as the flow rate of particles at an infinite height of the riser, as follows:

$$\varepsilon_\infty = 1 - \frac{K_\infty}{\rho_s (u_o - u_t)} \tag{4.9}$$

where ρ_s is the particle density, u_o is the superficial gas velocity which is the total

volumetric flow rate divided by the cross-sectional area of the riser, and u_t is the particle terminal velocity. In the present study, the following elutriation rate correlations were assessed:

$$K_\infty = 23.7\rho_g u_o exp^{-5.4\frac{u_t}{u_o}} \tag{4.10}$$

$$K_\infty = 0.011\rho_s(1-\frac{u_t}{u_o})^2 \tag{4.11}$$

$$K_\infty = 4.6x10^{-2}\rho_g \frac{(u_o-u_t)^2}{\sqrt{gd_p}} Re_t^{0.3}(\frac{\rho_s-\rho_g}{\rho_g})^{0.15} \tag{4.12}$$

Eqs. (4.10) and (4.11) were correlated from batch experiments on the elutriation rate performed by Geldart et al. (1979) and Colakyan & Levenspiel (1984) using different materials and particle sizes. Eq. (4.12), proposed by Tanaka et al. (1972), was correlated from a range of experiments performed on gas-solid and liquid-solid fluidized systems. In this work, Eqs. (4.10) to (4.12) were substituted separately into Eq. (4.1) to predict the solid fraction at the top of the riser (H=2.55 m), and these predicted solids fractions were compared with the experimental values.

Eq. (4.1) also contains the decay constant, a_d, which is related to the rate of interchange between the upward flowing solids in the core of the riser and the downward flowing solids in the annular wall layers. The decay constant has been determined by Adánez et al. (1994) using the following equation:

$$a_d = \frac{K_d}{(u_o-u_t)^2 D^{0.6}} \tag{4.13}$$

where K_d is the fitting parameter for the decay constant, which was found to be 8.6 in the work by Löffler et al. (2003). As mentioned in Section 2.4.1, the decay constant has been fitted by other researchers from experimental results (Senior & Brereton, 1992; Schoenfelder et al., 1996; Gungor & Eskin, 2007). In the present study, K_d will also be fitted to experimental results gathered in this work.

4.2.2 Effect of Solid Reflux from the Top of CFB Riser

It has been shown before that, due to the exit geometry, there is a solid reflux at the top of the CFB riser, which affects the solids mass flow rate out of the riser. To account for this effect, a reflux ratio denoted as k_m has been introduced by some researchers (van der

Meer et al., 2000). The reflux ratio is defined as the ratio of mass flow rate of particles in the annular walls, $\dot{m}_w$, to the solids outflow rate, $\dot{m}_{so}$. Rearranging the reflux ratio as a function of the solids core flow rate and the solids outflow rate:

$$\begin{aligned} k_m &= \frac{\dot{m}_w}{\dot{m}_{so}} \\ &= \frac{\dot{m}_{core} - \dot{m}_{so}}{\dot{m}_{so}} \\ &= \frac{\dot{m}_{core}}{\dot{m}_{so}} - 1 \\ \frac{\dot{m}_{core}}{\dot{m}_{so}} &= k_m + 1 \\ \frac{\dot{m}_{so}}{\dot{m}_{core}} &= \frac{1}{k_m + 1} \end{aligned} \tag{4.14}$$

van der Meer et al. (2000) have found values for the reflux ratio of a T-shaped exit geometry to be 0.39.

In Chapter 3, another type of model was developed to predict the reflux ratio. The solids outflow rate $\dot{m}_{so}$, was derived as a function of the aerodynamic factor (Φ_d), the exit width (w) and the core flow rate at the top of the riser,

$$\dot{m}_{so} = [\frac{\Phi_d w}{\pi D}]\dot{m}_{core} \tag{4.15}$$

The aerodynamic factor was already quantified in Chapter 3, and the exit width w is 0.07 m in this study. The ratio of $\dot{m}_{so}/\dot{m}_{core}$ from Eqs. (4.14) and (4.15) are compared to experimental results from Chapter 3, and are further discussed in Section 4.3.3.

4.2.3 Modeling the Solids Flow up the Riser

The upward solids flow rate in the core of the CFB riser is given by:

$$\dot{m}_{core} = \varepsilon_s \rho_s u_s A_{core} \tag{4.16}$$

where ε_s is the radially averaged solid fraction in the riser core at a given height, which can be determined from the core voidage as given by Eq. (4.1), u_s is the solid velocity, and A_{core} is the area of the core of the riser. The solids velocity can be estimated by

performing a force balance across a single particle (Löffler et al., 2003), as given by:

$$mu_s\frac{du_s}{dz} = (\rho_g - \rho_s)g\frac{\pi(\phi d_p)^3}{6} + \frac{1}{2}C_D\frac{\rho_g}{\varepsilon^{n_r}}\frac{\pi(\phi d_p)^2(u_o - u_t)^2}{4} \tag{4.17}$$

where m is the mass of a single particle, C_D is the drag coefficient, n_r is the Richardson-Zaki correction constant to account for the effect of particle swarms on the drag force, and u_s is the solid velocity. Eq. (4.17) was developed based on assumptions that the solid particle has reached a fully developed state, where the solid fraction does not decrease anymore with increasing height (if H>TDH), and there are no inter-particle interactions (ε is close to unity and flow is dilute). These assumptions simplified the prediction of the solids velocity, and may not be valid due to inter-particle interactions. The validity of these assumptions are discussed after comparison of the predicted solids core flow rate (Eq. (4.16)) with experimental results.

The drag coefficient, C_D, is defined as:

$$C_D = \begin{cases} \frac{24}{Re_p} & \text{Re<0.1} \\ \frac{24}{Re_p}(1+0.15Re^{0.687}) & Re_p < 500 \\ 0.44 & 1000 < Re_p < 1-2\times10^5 \end{cases} \tag{4.18}$$

where the particle Reynolds number, Re_p, is a function of the solids velocity u_s, which is equal to the difference between the superficial gas velocity and the terminal velocity $(u_o - u_t)$, and is expressed as

$$Re_p = \frac{\rho_g(\phi d_p)(u_o - u_t)}{\mu_g} \tag{4.19}$$

where ϕ is the particle circularity, d_p is the particle diameter, ρ_g and μ_g are the gas density and viscosity, respectively. The particle terminal velocity (u_t) in a stagnant environment for the copper particles (with similar properties listed in Chapter 3) was calculated to be 1.20 m/s. The solids velocity up the height of the riser can then be solved numerically once the boundary conditions are known. At the dilution point, the initial solid velocity was assumed to be equal to the superficial gas velocity of both the primary and secondary airflow rates.

4.2.4 Modelling the Pressure Drop

A model of pressure drop in the bottom and the upper sections of the riser is proposed and its accuracy is then tested by comparing with the measured values presented in Chapter 3. The pressure drop in the bottom region of the riser, ΔP_{br} is determined from the pressure head of the solids and can be calculated from the following equation:

$$\Delta P_{br} = \rho_s g \int_{H1}^{H_2} (1-\varepsilon) dH \tag{4.20}$$

where ε is the voidage from Eq. (4.1). The voidage in Eq. (4.20) includes the dense zone voidage (Eq. (4.2)) and the voidage above the dense zone (Eq. (4.1)). In Eq. (4.20), H_1 and H_2 corresponds to the location of the pressure taps for measuring the riser pressure drop in the bottom section, which are at 0.10 and 1.00 m above the distributor plate.

The pressure drop within the upper section of the CFB riser consists of several components which include the pressure head of the gas and solids (ΔP_g, ΔP_s), the acceleration of gas ($\Delta P_{g,acc}$) and solid particles ($P_{s,acc}$), and the frictional pressure drop (ΔP_{sf}), respectively. This is summarized by Eq. (4.21).

$$\Delta P_{ur} = \Delta P_s + \Delta P_g + \Delta P_{g,acc} + \Delta P_{s,acc} + \Delta P_{sf} \tag{4.21}$$

The pressure drop components due to acceleration of gas and solid are assumed to be negligible in the riser upper section for fully developed flow where the solids velocity is constant after a certain riser height as mentioned before in Section 4.2.3. The validity of these assumptions is discussed in Section 4.3.3.

Nakamura & Capes (1973) reported that the inclusion of solids-to-wall frictional forces could result in an over-prediction of the transport zone pressure drop by a factor of 10 or higher than the measured values. Besides that, it was shown in Fig. 2.6 that the wall frictional force only becomes dominant if the superficial gas velocity in the riser is above 11 m/s (Nieuwland et al., 1997). Since the maximum superficial gas velocity in the experiments of the present study is only 2.14 m/s, it can be concluded that the wall frictional forces can be neglected for modelling the riser upper section pressure drop.

Thus, the pressure head of the solid volume fraction in the core region is the only dominant component for the riser upper section pressure drop ΔP_{ur} which is related to

the solid fraction gradient along the CFB riser height. Therefore, the riser upper section pressure drop can be calculated by integrating the pressure drop over a certain riser height. In this study, the pressure drop in the upper regions of the riser (ΔP_{ur}) was predicted and measured within a height of H_3 and H_2:

$$dP_{ur} = \rho_s g \int_{H_2}^{H_3} (1-\varepsilon) dH \tag{4.22}$$

In the CFB riser used in this study, H_3 and H_2 can be regarded as the heights of the pressure taps at 2.3 m and 1.0 m respectively; ε is the radially averaged voidage in the core at a riser height calculated from Eq. (4.1). The predicted riser upper section pressure drop was then compared to the experimental measurements.

4.2.5 Assessment Procedure

The empirical correlation for the dense zone voidage (Eq. (4.2)) is used to determine the voidage at the dilution point (Eq. (4.7) and (4.8)). From the voidage at the dilution point, the transport zone voidage and solid fraction can be calculated from Eq. (4.1). Eq. (4.1) contains another variable the voidage at infinity (ε_∞), which requires a separate correlation for the elutriation rate, K_∞. Three different correlations for the elutriation rate (Eqs. (4.10), (4.11) and (4.12)) are then assessed based on the comparison of the predicted and measured solid fraction at the top of the riser (H=2.55 m). Because the model predicts that the solid fraction at the top of the riser no longer varies with the decay constant, the solid fraction will be equal to the solid fraction at an infinite height. Therefore, a valid comparison of the experimental data and the predicted results from Eqs. (4.10) to (4.12) can be made.

Using a suitable correlation for the elutriation rate, a sensitivity analysis of the decay constant a_d, from Eq. (4.13) is then performed for the solid fraction at 0.95 m. A suitable value for K_d was then chosen to predict the solids core flow rate. However, it will be shown that the solids core flow rate was not predicted accurately because the solid fraction was inaccurately predicted.

In order to reduce the discrepancy from the predicted solid fraction, the voidage at infinity was then fitted to the measured solid fraction at a riser height of 2.55 m. A

suitable K_d value was then chosen for the prediction of solid fraction at 0.95 m. Then, a comparison of the predicted and measured solids core flow rate is made again, using the fitted correlation for the voidage at infinity. Using the same fitted correlation, riser upper section pressure drop was then predicted (Eq. (4.20) and (4.22)) and compared to measured values. A comparison of the predicted and measured riser pressure drop in the bottom region was also made.

4.3 Assessment of Predicted Results from Hydrodynamic Models with Experimental Data

4.3.1 Elutriation Rate Correlations

Fig. 4.3 shows the measured and predicted solids fractions at the top of the riser (2.55 m) for primary airflow rates from 32 to 96 m^3/h and a fixed secondary airflow of 171 m^3/h. The predicted solids fractions at the top of the riser are calculated via the elutriation rates from three different correlations as given in Eqs. (4.10) to (4.12). The prediction of Eq. (4.10) for the elutriation was in reasonable agreement with the experimental results, whereas there were significant discrepancies for the other models (Eqs. (4.11) and (4.12)).

The discrepancies between the predicted results and the experimental values are due to the different experimental conditions used in the present study compared with those used in the development of Eqs. (4.10) to (4.12). These correlations are only applicable within the range of experimental conditions tested in developing them. For example, in this work the Froude number ranged from 1.1 to 1.5, whereas in the work of Tanaka et al. (1972), the Froude number varied from 10 to 500. In addition, the density ratio of solids to gas in the work of Tanaka et al. (1972) was between 1 and 4000 which is much lower than the density ratio of 7575 in the present study. In the experiments of Colakyan & Levenspiel (1984), an amount of 10 % of the total bed inventory was added as fines whereas in this work no additional fines were added. The higher mass loading of fine particles in the total bed inventory increases the elutriation rate, which results in a higher solid fraction at an infinite riser height. Finally, a ratio u_t/u_o was found to be between 1.5 and 2.4 in this work for the dense zone, whereas the model of Geldart et al. (1979) is applicable over

for the u_t/u_o ratio in the range from 0.1 to 1.5. This shows the clear weakness of using empirical models fitted to experimental data - that these models are not general in nature. The elutriation rate of Geldart et al. (1979) (Eq. (4.10)) gives the best fit particularly for primary airflow rates above 70 m^3/h, and thus has been used in Eq. (4.1) for initial assessment of the hydrodynamic model.

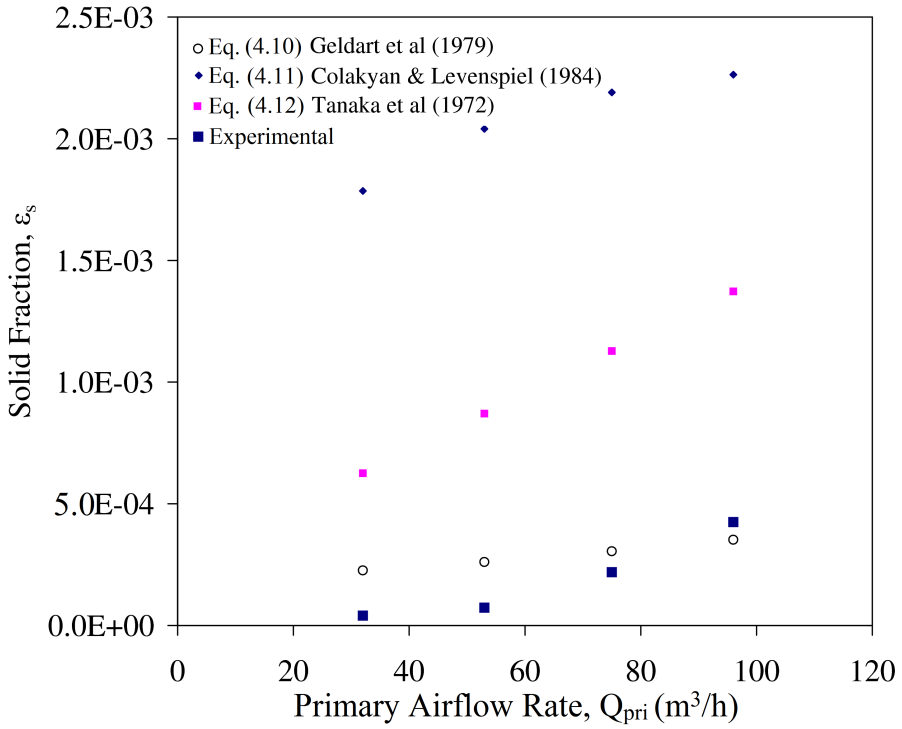

Fig. 4.3: Comparison of predicted and measured solid fraction ε_s at H=2.55 m with elutriation rates calculated from different correlations. Experimental conditions: Q_{ls}=6 m^3/h; Q_{sec}=171 m^3/h.

4.3.2 Assessment of Hydrodynamic Models

The models for prediction of the solid fraction along the CFB riser height include several fitting parameters, such as the decay constant (a_d) in Eq. (4.1) which can be calculated using Eq. (4.13). This equation in turn involves one fitting parameter, K_d. A sensitivity analysis was performed to determine the effect of this fitting parameter on the predicted values for the solid fraction. As mentioned earlier, the dilution effect due to the injection of secondary flow at a height of 0.18 m above the distributor plate was incorporated into the hydrodynamic model using Eq. (4.7) and (4.8). In the sensitivity analysis, Eq. (4.10) was used for the calculation of elutriation rate as this model gave the

best fit to the experimental data as shown in Fig. 4.3. The decay constant, a_d, is calculated using Eq. (4.13).

Fig. 4.4 shows the predicted solid fraction using all values of K_d at a riser height of 0.95 m and 2.55 m. The error bars for the experimental data at a riser height of 0.95 m are not visible due to the scale of the y-axis on the left. For a riser height of 2.55 m, the predicted solid fraction does not agree well with the experimental data, though the results were more accurate at a riser height of 0.95 m. All the data points for the predicted solid fraction at a riser height of 2.55 m are on the same line irrespective of the value of K_d. The fitting parameter K_d does not have any effect on the predicted solid fraction at this height because, in this case, the hydrodynamic model predicts that the height has exceeded the transport disengaging height (TDH), and thus the solid fraction at the top of the riser is close to the solid fraction at infinity, which does not depend on the rate of solids fraction decay in the transport zone.

In Fig. 4.4, the sensitivity analysis on the fitting parameter shows that a K_d value 2.5 gives a close agreement of the predicted solid fraction with the experimental data at a riser height of 0.95 m, and a further increase in K_d does not have significant effect on the solid fraction. Therefore, a K_d value of 2.5 was chosen for further analysis of the hydrodynamic model. Löffler et al. (2003) used a higher value of 8.6, which can be attributed to a faster rate of solid fraction decay along the riser height in their experiments.

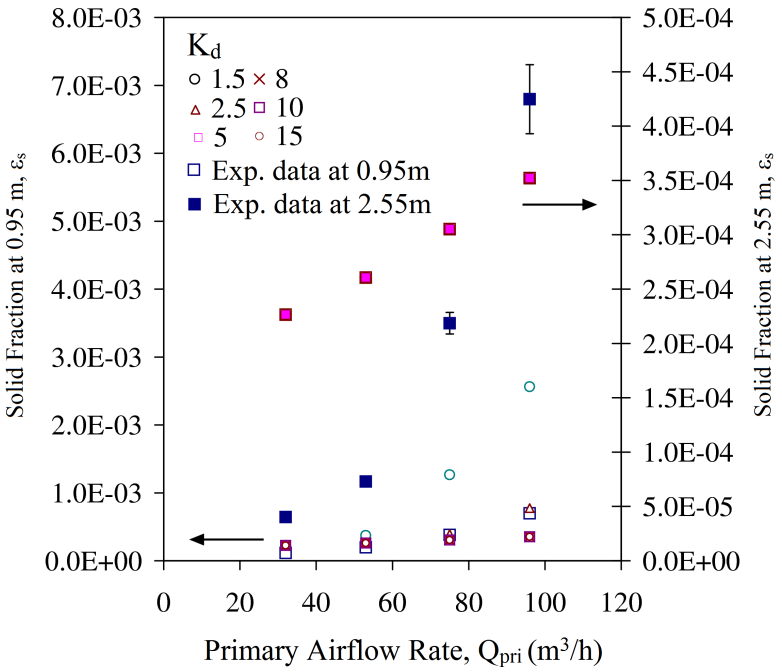

Fig. 4.4: Comparison of measured and predicted solid fraction ε_s at H=0.95 m and 2.55 m. The decay constant (a_d) is calculated from Eq. (4.13) with K_d values vary from 1.5, to 15, the voidage at infinity ε_∞ is Eq. (4.10), dense zone voidage, ε_{dz} from Eq. (4.2), dilution point voidage ε'_{dz} from Eq. (4.7) and (4.8). Experimental conditions: Q_{ls}=6 m^3/h; Q_{sec}=171 m^3/h.

Using Eqs. (4.2), (4.10), (4.13) with a K_d value of 2.5, the solids core flow rate in the CFB $\dot{m}_{core}$ was predicted using Eq. (4.16) and the solids velocity from Eq. (4.17). Fig. 4.5 shows that the predicted solids core flow rate at a riser height of 2.55 m was lower than experimental values at the higher primary airflows. It should be noted that the solids core flow rate is a function of the solid fraction (Eq.(4.16), and thus the discrepancy can be due to the errors in the predicted solid fraction (Fig. 4.4). The main reason for the discrepancy between the predicted and measured solid fraction is in turn due to the inaccuracy in the elutriation rate correlation in Eq. (4.10), which causes errors in the predicted voidage at an infinite riser height (ε_∞). These errors are most likely due to the difference in experimental operating conditions used to derive Eq. (4.10) compared with the experimental operating conditions tested in this work, as mentioned in Section 4.3.1.

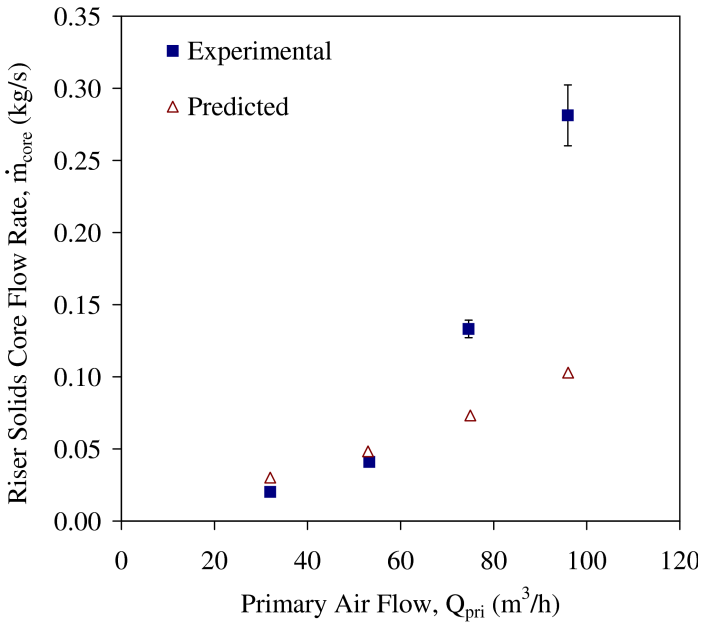

Fig. 4.5: Comparison of measured and predicted solid core flow ε_s at H=2.55 m. The decay constant (a_d) is calculated from Eq. (4.13) with K_d =2.5, the voidage at infinity ε_∞ is Eq. (4.10), dense zone voidage, ε_{dz} from Eq. (4.2), dilution point voidage ε'_{dz} from Eq. (4.7) and (4.8). Experimental conditions: Q_{ls}=6 m^3/h; Q_{sec}=171 m^3/h.

To reduce the source of inaccuracy in the prediction of the solids core flow rate, the measured values of the solid fraction at the top of the CFB riser were used to develop an empirical correlation for the voidage at infinity (ε_∞) as follows:

$$\varepsilon_\infty = 1 - 1 \times 10^{-5} exp^{0.0382 Q_{pri}} \tag{4.23}$$

Accurately representing the solids voidage at infinity in the formulation allowed the deficiencies in any other modelled parameters used to calculate the solids core flow rate (through Eq. (4.16)) to be highlighted, such as solids velocity. It has to be noted that the actual voidage at infinity could not be determined experimentally for the current work. The voidage at infinity was approximated to be equal to the voidage at the top of the riser (H=2.55 m).

Fig. 4.6 shows that the predicted solid fraction using Eq. (4.23) at riser heights of 0.95 m and 2.55 m is close to experimental values for a range of primary airflows, essentially because the fitted correlation (Eq. (4.23) is used for the voidage at infinity and the K_d coefficient has been adjusted to a value of 2.5 to match prediction with experimental values.

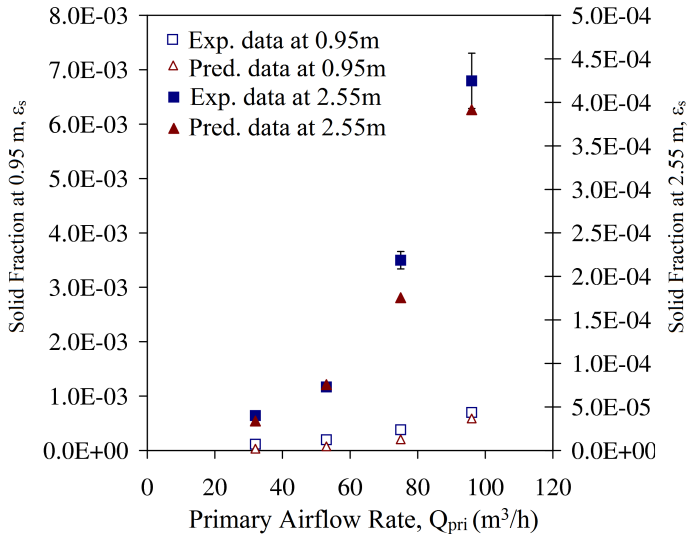

Fig. 4.6: Comparison of measured and predicted solid fraction ε_s at H=0.95 m and 2.55 m. The decay constant (a_d) is calculated from Eq. (4.13) with K_d =2.5. The voidage at infinity (ε_∞) is estimated from Eq. (4.23), dense zone voidage, ε_{dz} from Eq. (4.2), dilution point voidage ε'_{dz} from Eq. (4.7) and (4.8). Experimental conditions: Q_{ls}=6 m^3/h; Q_{sec}=171 m^3/h.

Despite the solid fraction can be predicted accurately, Fig. 4.7 shows that the hydrodynamic model under-predicted the solids core flow rate at a height of 0.95 m and 2.55 m when compared with the measured values. Since the solids fraction has been fitted to the experimental values, according to Eq. (4.16), the most likely reason for the under-prediction of the solids core flow rate would be an under-predicted solids velocity in the core. The under-predicted solids velocity is due to several factors. Firstly, the formation of clusters of particles and their effects on the drag force should be accounted for through the Richardson-Zaki correction in Eq. (4.17). However, in the experiments, even at low primary airflow rate (32 m^3/h), when the solid concentration was dilute and the Richardson-Zaki correction tended to unity, occasional ropes or streams of particles were observed to flow within the riser. If the ropes or streams of particles are imagined as a single cluster of multiple particles, the effective size of the cluster would be higher, and the effective density would be lower. The combined effect would lower the drag coefficient (Zou et al., 2008). This would increase the length of acceleration zone for the cluster of particles to reach a constant velocity (Huang et al., 2006). Therefore, the actual solids velocity should be higher.

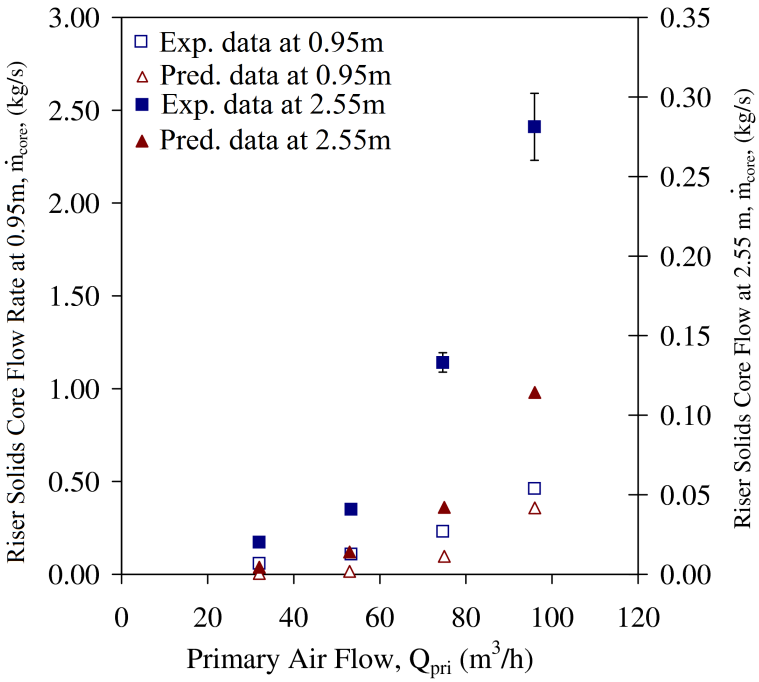

Fig. 4.7: Comparison of predicted and measured riser solids core flow at H=0.95 m and 2.55 m. Voidage at infinity ε_∞ is calculated from Eq. (4.23), K_d is 2.5 with a_d from Eq. (4.13), dense zone voidage, ε_{dz} from Eq. (4.2), dilution point voidage ε'_{dz} from Eq. (4.7) and (4.8). Experimental conditions: Q_{ls}=6 m^3/h; Q_{sec}=171 m^3/h.

Another factor for the error is the presence of high velocity jets from the secondary air injectors, which rapidly accelerate the particles. With the clustering of particles reducing the drag coefficient, coupled with the high velocity jets, the length of acceleration required for the particles to achieve a fully developed state will be longer. Hence, the solids velocity (in clusters or streams) will be higher compared to the predicted solids velocity from the force balance over a single particle (Eq. (4.17)). The abrupt exit near the top of the riser also causes reflux of solids downwards at the wall in an annular layer, leading to an increase in inter-particle interactions with the core flow. Again, the inter-particle interactions are not taken into account in Eqs. (4.16) and (4.17), leading to a discrepancy to the predicted riser solids core flow.

One way to correct for the solids velocity for the clustering phenomenon and inter-particle interactions is to use an effective cluster density, an effective cluster diameter and a cluster based drag coefficient in Eq. (4.17), in place of the particle density,diameter and single-particle drag coefficient (Zou et al., 2008). The inclusion of cluster properties decreases the drag coefficient (and the terminal velocity), and hence increases the solids

velocity. However, in the current study, we are unable to emulate the work from Zou et al. (2008) because we are unable to determine the cluster diameter. Future investigations can include work on measurement and modelling of the cluster diameter and density to validate its effect on the drag coefficient and solids velocity.

As mentioned in Section 4.3.2, the fitting parameter K_d is lower compared to the work from Löffler et al. (2003), resulting in a lower decay constant. Thus there is a slower decay of the solids fraction with increasing riser height in this work. The aforementioned factors of the particle clustering effect, the high velocity secondary air jets, and the inter-particle interactions may have contributed to the slower decay of the solids fraction. It should be noted that the values of the decay constant a_d vary widely in literature. The range of the decay constant in this work was 7.16 to 34.45 m^{-1}, whereas Yang et al. (2009) used a value of 0.25 m^{-1}, Chen & Wen (1982) used 3.5 to 6.4 m^{-1}, and Löffler et al. (2003) had 2.4 to 24.9 m^{-1}. The differing values of the decay constant are attributed to the difference in the riser diameter, riser height and also the particle properties. The difference in the decay constant a_d and also the fitting parameter K_d shows again, that there is no general value that can be used in the hydrodynamic model. The correlations are unable to include the specific nature of the physical behavior occurring in each separate CFB riser. For an accurate prediction of the solid fraction, a fitting of parameters is inevitable, and there should be a careful assessment of the correlations before they are applied to any CFB riser.

4.3.3 Effect of Reflux on Solids Circulation Rate

Fig. 4.8 shows a comparison between the values of $\dot{m}_{so}/\dot{m}_{core}$ obtained from experiments of the present study with those from the propsed model in this study (Eq. (4.15)) and the model of van der Meer et al. (2000) (Eq. (4.14)). According to van der Meer et al. (2000), the reflux ratio (k_m) for a short extension of a blind T-exit geometry is 0.39 (from Fig. 2.5). Using this value, the ratio of $\dot{m}_{so}/\dot{m}_{core}$ is calculated to be 0.72 from Eq. (4.14). In the study of van der Meer et al. (2000), the reflux ratio was derived from a single operating condition (van der Meer et al., 2000). In this work, the reflux ratio is found to be a function of the gas velocity as shown in Fig. 4.8. However, Eq. (4.14) does not cater for these variations. There are also discrepancies caused by some

differences in the riser configuration and exit geometry between the present study and those of van der Meer et al. (2000). In the study of van der Meer et al. (2000), the CFB riser had a square cross-section and the exit duct was horizontal which would allow particle dunes to form in the exit duct. This led to a return flow of solids and an increase in the solids recirculation in the riser. In the present study, the riser cross-section was rectangular, and the riser exit was inclined downwards and was connected to the cyclone to prevent solids build-up in the exit duct.

The ratio of $\dot{m}_{so}/\dot{m}_{core}$ from the hydrodynamic model (Eq. 4.15) was found to be reasonably accurate when compared to the experimental data. The correlation coefficient R^2 for Eq. 4.15 is 0.5199, which is better than that of van der Meer's equation (Eq. 4.14) which was in the negative. The low R^2 value for Eq. 4.15 suggests that the reflux ratio is not a strong function of the primary airflow rate. Fig. 4.8 also shows that at low primary airflow rate, the $\dot{m}_{so}/\dot{m}_{core}$ ratio approaches unity while at high primary airflow rates, $\dot{m}_{so}/\dot{m}_{core}$ decreases. This trend has been discussed in Chapter 3.

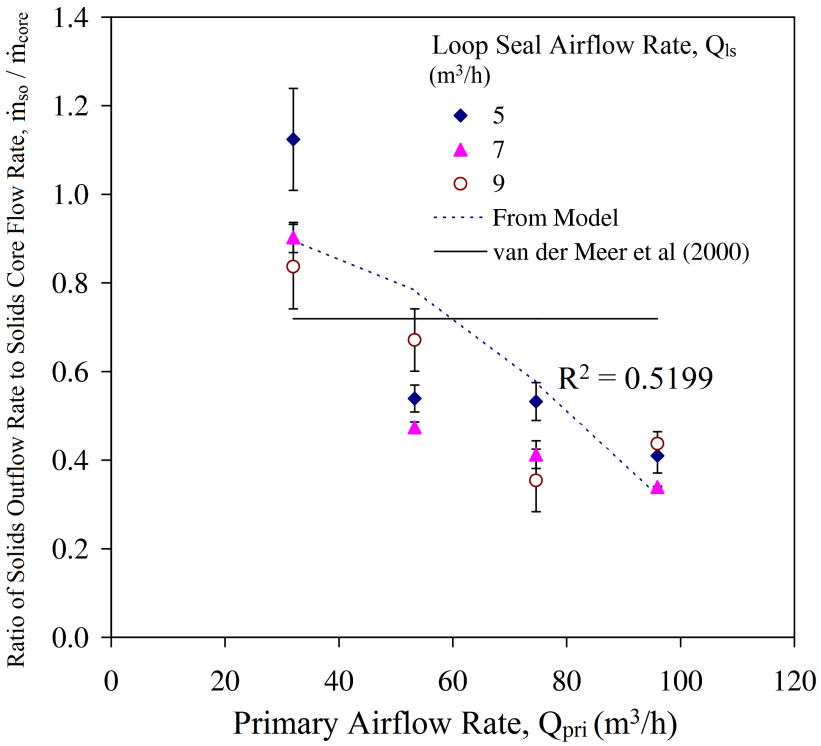

Fig. 4.8: Comparison of experimental values of $\dot{m}_{core}/\dot{m}_{so}$ with Eq. (4.14) (van der Meer et al., 2000) and Eq. 4.15. Experimental conditions: Q_{sec}=171 m^3/h.

4.3.4 Modelling Pressure Drop

The correlations and fitting constant that resulted in the most accurately predicted solids fractions were used in the pressure drop analysis. Thus, weaknesses in the solids fraction models could be separated out so that any weaknesses in the pressure drop models could be exposed. The solid fraction is calculated using Eq. (4.1) in which the voidage and decay constant were determined as described in Sections 4.3.1 to 4.3.4. The dense zone voidage was from Eq. (4.2), and the dilution point voidage from Eq. (4.7) and (4.8).

Fig. 4.9 shows the measured and predicted pressure drop at the bottom of the riser (Eq. (4.20)). The pressure drop is over-predicted when compared to the measured values. The significant discrepancy is due to the over prediction of the solids fraction just above the dilution point. The reason of this discrepancy is due to the fact that the hydrodynamic model is unable to model a significant mixing mechanism between gas and solids that extends above the dilution point.

Fig. 4.10 shows the measured and predicted pressure drop in the upper sections of the riser, calculated from Eq. (4.22). From Fig. 4.10, it is found that the trend of the predicted and experimental results of the riser upper section pressure drop ΔP_{ur} are in reasonable agreement when K_d parameter is taken as 2.5, although the predicted pressure drop tends to be lower than the measured values. The lower values of the predicted pressure drop in the upper regions of the riser are due to the assumption that the pressure drop due to solids acceleration is negligible in the transport zone in a fully developed and dilute flow. In reality, the clustering effects reduces the drag coefficient, resulting in a high solids acceleration. Consequently, the predicted pressure drop is lower when this effect is not taken into account. However, the trend of the predicted riser pressure drop in the upper sections as a function of primary airflow rate is similar to that of the measured data, and a correlation factor can be introduced to reflect the neglected pressure drop components in the model.

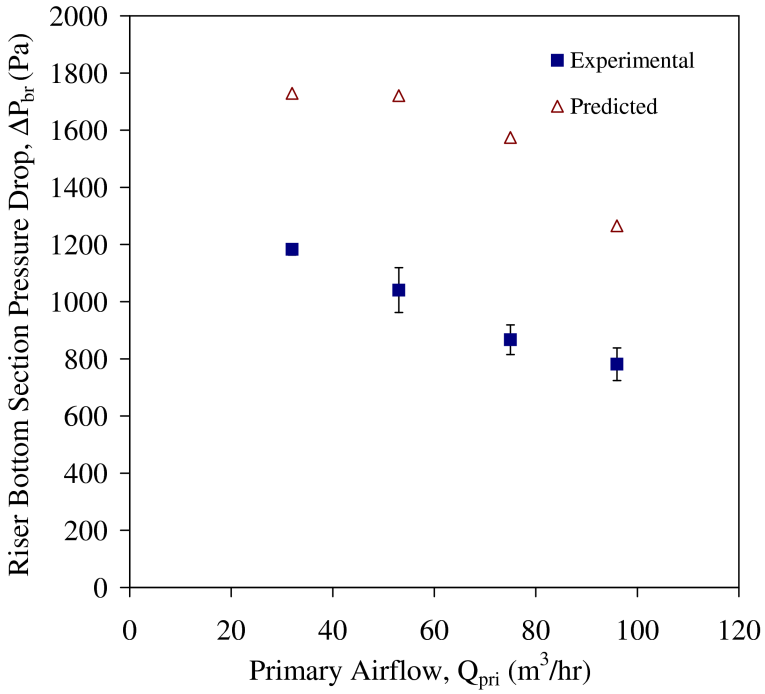

Fig. 4.9: Comparison of predicted and measured riser pressure drop in the bottom region ΔP_{br}. Experimental conditions: Q_{ls}=6 m^3/h; Q_{sec}=17 1m^3/h. Dense zone voidage from Eq. (4.2).

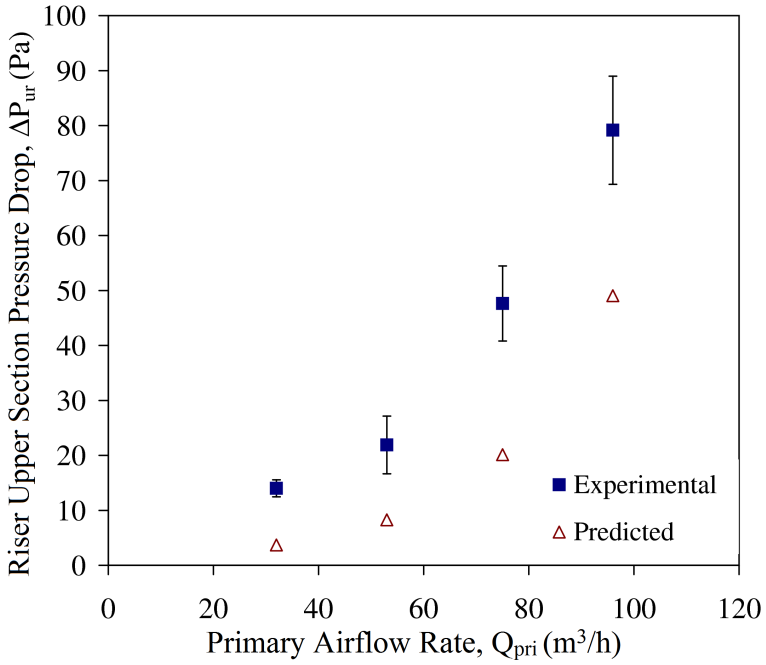

Fig. 4.10: Comparison of the predicted and measured riser upper section pressure drop ΔP_{ur} for different primary airflows. Voidage at infinity ε_∞ is calculated from Eq. (4.23), K_d is 2.5 with a_d from Eq. (4.13), dense zone voidage from Eq. (4.2), dilution point voidage from Eq. (4.7) and (4.8). Experimental conditions: Q_{ls}=6 m^3/h; Q_{sec}=171 m^3/h.

4.4 Conclusions

An assessment of the various empirical models published in literature has shown that these models are unable to accurately predict the axial solid fraction or the solids core flow rate in the CFB riser of this work due to a lack of generality. Often these models are fitted to experimental data for one configuration, but being empirical in nature, these models cannot be applied to different configurations. For example, some of the published correlations for the elutriation rate are not valid for high density particles, such as the particles copper used in this work. Besides that, the models do not account for some of the physics that affects solid flow in the CFB riser. For example, clustering effects of particles are not accounted for properly in the published models. Clustering effects reduce the effective density but increase the effective size, and hence reduce the drag coefficient, which causes the solid particles to undergo an extended acceleration length aided by the secondary air jets. Further work is required to model and validate the cluster properties before its effect on the reduction of the drag force can be justified.

From the assessment of pressure drop model, it was found that the model over-predicts the riser bottom section pressure drop. This was because the model is not able to account for the significant gas-solid mixing mechanisms just above the dense zone and in the lower regions of the riser. Using the empirical correlation for the voidage at infinity and a value of 2.5 for the decay constant K_d, the predicted riser upper section pressure drop has similar trend to experimental data.

Chapter 5

Hydrodynamics of Binary Mixture in a Dual Fluidized Bed

After the experimental investigation of the circulating fluidized bed (CFB) in Phase I of this study as explained in Chapter 3, and the critical assessment of hydrodynamic models detailed in Chapter 4, the project progressed to Phase II, which was marked by the successful construction and commissioning of the dual fluidized bed (DFB) cold model (see image in Appendix B). Although the results for Phase I in Chapter 3 and 4 may not be in full agreement with those of Phase II, the hydrodynamics of the CFB in the DFB cold model is still similar when operating the CFB in connection with the BFB. However, additional operating concerns need to be addressed when operating the DFB, which are discussed in this chapter.

5.1 Introduction

In a dual fluidized bed (DFB) gasification plant, there are two fluidized bed reactors, one acting as a combustor and the other as a gasifier. Description and flow diagram of the DFB gasification plant have been given in Chapter 3 (Fig. 3.1). This system has become more common for biomass gasification in industry owing to its higher fuel conversion rate and low tar production compared with its counterparts, such as the bubbling and circulating fluidized bed reactors (Xu et al., 2006). To operate a DFB at stable conditions, there are two additional operating variables, compared with the CFB alone, that need to

be considered for steady state operation. These two additional operating variables are the bubbling fluidized bed (BFB) airflow rate (Q_{BFB}) and the chute airflow rate (Q_{ch}), depicted in Fig. 5.1. In addition, the interaction of the pressure difference between the CFB riser and the BFB reactor, indicated by ΔP_{CB}, as well as the chute pressure drop (ΔP_{ch}), are dominant factors affecting steady state operation of the DFB system. The chute pressure drop is especially critical as it is indicative of the gas seal effectiveness between the CFB riser and the BFB. When the bed material in the BFB is fluidized such that it expands above the chute exit height, the bed material flows into the inclined chute and into the dense zone of the CFB riser. This creates a gas seal between the BFB and the CFB riser dense zone, preventing primary airflow in the CFB from bypassing through the chute and out into the BFB. The bypassing of primary airflow through the chute, which can be accompanied by a partial reverse flow of solids, is a condition called chute bypass, and can occur when the bed expansion in the BFB is insufficient due to a low BFB airflow rate (Q_{BFB}).

Fig. 5.2 illustrates the flow condition during chute bypass. Chute bypass causes a loss of air flow from the CFB riser and a consequent decrease in the combustion efficiency. The resultant bypassing air flow into the BFB dilutes the energy content of producer gas and decreases the gasification efficiency of the BFB. In addition, due to the partial reverse flow of solids in the chute, the solids flow rate from the BFB to the CFB can be significantly reduced, leading to a low solids circulation rate through the plant. Chute bypass should be avoided in an industrial DFB plant. One of the aims of this chapter is to determine operating conditions that cause chute bypass to occur.

Operational boundaries for the steady state operation of the DFB as a function of the primary airflow rate in the CFB riser and the BFB airflow rate are presented in this chapter. This operational map also indicates operating conditions that result in chute bypass. Such an operational map has not been reported in the literature previously. Measurements of the riser bottom and upper section pressure drops and the solids core flow rate are also presented.

In the gasification plant, the bed material normally includes a mixture of sand as the inert bed material, biomass, and char, produced by devolatilization of the biomass. The hydrodynamics of this mixture within the DFB is important due to the interaction between

the components of the bed, and the effect this interaction has on the solids recirculation rate in the system (Rasul & Rudolph, 2000; Chen et al., 2006; Jang et al., 2010). In a DFB gasification plant, biomass is gasified in the BFB, and only the resultant char passes through to the CFB. The DFB cold model used in this work was not able to simulate the conversion of biomass into char and the combustion of char in the CFB riser. However, the focus of this section of the research was on how the char flow in the chute and CFB riser affected the steady operation of the DFB. It was assumed that biomass had no direct effect on solid and gas flows in the chute and riser, and therefore this component was not represented in the cold model investigation. In this study, copper and medium density polyethylene (MDPE) pellets were used in the DFB cold model to represent sand and biomass chars in a DFB gasifier. Two different sizes of MDPE pellet sizes were used to represent the range of biomass char particle sizes observed in practice. An investigation into the effect of this binary mixture on the pressure drop and the solids core flow rate in the cold model DFB is presented here.

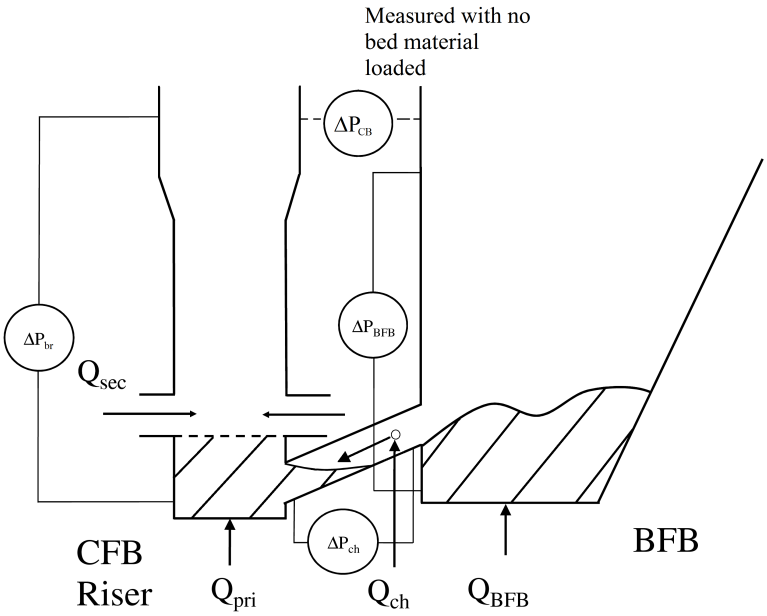

Fig. 5.1: Location of pressure taps, and aeration points for DFB.

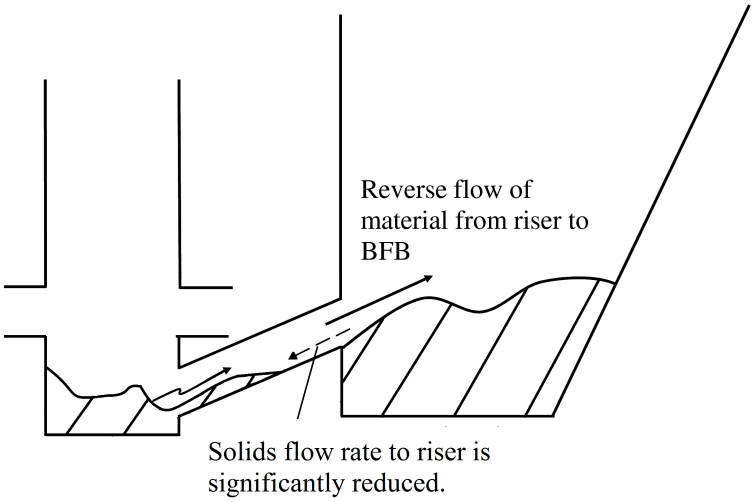

Fig. 5.2: Reverse flow of gas and solids from riser to BFB during chute bypass.

5.2 Materials and Methods

5.2.1 Materials and Methods for Initial Experiments with only Copper as Bed Material

In the DFB system tested in this study, the BFB is connected to the CFB via a chute near the bottom of the two columns (Fig. 5.1 and 3.1). The bottom section of the BFB is tapered at 30° to the vertical axis, so that the BFB diameter is increased from 0.25 m at the base where the air distributor plate is located to 0.625 m at a height of 0.66 m. The increase in the BFB diameter reduces the velocity of gas up the height of the BFB, which in turn reduces the entrainment of solid particles into the gas stream. The tapered geometry of the BFB also increases the particle residence time by allowing the flotsam particles (mentioned in Chapter 2) to circulate in the tapered region (Foscolo et al., 2007). The dimensions and configuration of the BFB of the cold model are a scale-down model from the BFB gasification reactor in the Güssing biomass gasification plant (Löffler et al., 2003; Kaiser et al., 2003).

The chute connection near the DFB bottom as shown in Fig. 5.1 is inclined at 45° to the horizontal axis. The inclined chute contains a sparge, which is a pipe with nozzles protruding into the inclined chute. The nozzles produce high velocity air jets with total flow rate (Q_{ch}) towards the CFB riser to promote the bed material flow from the BFB to

the CFB. The inclined chute is connected to the BFB at a height of 0.13 m above the BFB air distributor plate, which is the lowest possible height without intersecting with other components of the BFB, namely, with one of the flanges of the BFB.

To help elucidate the condition in the where chute bypass occurs, the CFB-BFB pressure drop was measured without loading any bed material into the system. With no solids loaded in the DFB, there is always a chute bypass from the CFB to the BFB through the chute driven by a pressure drop across these units. Fig. 5.1 shows the location of the pressure taps for determining the CFB-BFB pressure drop ΔP_{CB}, which are located 1.0 m above the base of the CFB air distributor plate. The BFB airflow rate (Q_{BFB}) was varied from 54 to 76 m^3/h to determine its effect on the CFB-BFB pressure drop. The chute airflow was shut off during this experiment to avoid disruption from the jets of the sparge on the pressure drop measurements during the chute bypass flow. The primary and secondary airflow were maintained constant at 54 and 324 m^3/h respectively during these measurements.

In the subsequent experiments on the DFB, copper particles (80 kg provided by DL Industrial, Singapore) were used for the bed material. The copper particles had an average Archimedes number of 215 (particle diameter of 142 μm and circularity of 0.64), which is within 25% of the Archimedes number of particles in the gasification plant in Güssing. Deviations of the dimensionless numbers were difficult to avoid, and a certain margin of error should be allowed for, as has been stated by Proll et al. (2009). With the copper loaded into the DFB, the effects of BFB airflow and chute airflow on the solids flow rate and pressure drops were investigated. The BFB airflow rate was set to 54 and subsequently, 76 m^3/h, and the chute airflow rate was varied between 0 and 5 m^3/h. During these experiments, the primary, secondary and loop-seal airflow rates were maintained at 54, 324, and 5 m^3/h respectively. The BFB airflow was limited to 76 m^3/h to so that the flow number (u_o/u_{mf}) was maintained to a value of 3.41, which is within range with the values in the industry (Foscolo et al., 2007). The solids core flow and solids outflow rates were determined by following the procedures detailed in Chapter 3. Pressure drops were monitored according to the locations detailed in Chapter 3, with two additional pressure drops monitored: the pressure drop across the BFB, ΔP_{BFB}, and the chute pressure drop, ΔP_{ch} (shown in Fig. 5.1).

For experiments involving binary mixtures, copper and MDPE pellets (Clariant, New Zealand) were used to simulate sand and woody biomass chars, respectively. Char particles typically range in size from 1 to 8 mm in an industrial gasifier (Scala et al., 2006). The char particle density and circularity in an industrial gasifier are approximately 250 kg/m^3 and 0.71 respectively (Xu et al., 2011a,b), which are within the range of values reported by Scala et al. (2006). Through the scaling laws mentioned in Chapter 3, MDPE pellets of size 370 and 1750 μm with a corresponding particle circularity of 0.47 and 0.72 (particle density of 935 kg/m^3) were selected as the secondary material for the binary mixture experiments. Using Equations (3.1) to (3.3), the Archimedes numbers were calculated to be 157 and 59899 for the MDPE pellet sizes of 370 and 1750 μm, respectively. These values are similar to the values of 115 and 58872 corresponding to biomass chars of 1 and 8 mm in size (found in an industrial gasifier operating under high temperature conditions) respectively. The size distribution of the 370 μm MDPE pellets was wide, ranging from 176 to 704 μm. In each run, 2 kg of either 370 μm or 1750 μm MDPE pellets were preloaded into an intermediate hopper. Note that 2 kg of MDPE represents 2.5% of the total bed material (80kg of copper), which, depending on the operating conditions, is similar to the percentage of biomass char present in the CAPE pilot-scale gasification system during normal operation (Bull, 2008). A valve was opened to allow the MDPE pellets to flow from the hopper into the DFB system.

In the binary mixture experiments, the solids core flow rates of copper and MDPE pellets were determined using the suction probe method described in Chapter 3, for a BFB airflow rates of 54 and 76 m^3/h, while maintaining the primary, secondary, loop-seal and chute airflow rates at 54, 324, 5 and 5 m^3/h, respectively. The sampling time was four minutes. The collected particles were then sieved several times to remove the MDPE granules from the copper particles, and the amount of each material was then measured. The measurements were taken at radial positions of 0, 60 and 105 mm from the center of the CFB riser. The copper and MDPE solids core flow rates were finally determined from an integration of the radial profile of the local solids flux. Note that the 1750 μm MDPE pellets were reasonably uniform in size, while the size distribution of the 370 μm MDPE pellets was wide, ranging from 176 to 704 μm. The wide size

distribution of the 370 μm particles had a bearing on the accuracy of the solids core flow measurements due to the issue of properly separating the copper and MDPE particles, which were similar size at the smaller end of the MDPE particle size distribution. The solids outflow from the CFB was not measured in the experiments with the binary mixture, because the bulk density of the binary mixture was unknown in the loop seal.

The binary mixture experiments did not account for the evolution of char particle size due to attrition and fragmentation mechanisms that are prevalent in gasification (Scala et al., 2006; Gómez-Barea & Leckner, 2010). However, the MDPE pellet sizes represent a wide range of char sizes found in practice (from 1 to 8 mm). Therefore, the experimental results from the binary mixture experiments are still representative of the hydrodynamics of sand-char binary mixture in the actual gasification plant.

5.3 Results and Discussion

5.3.1 Chute Bypass

Chute bypass (illustrated in Fig. 5.2) occurs when the force due to the CFB-BFB pressure drop ΔP_{CB} is equal to or higher than the gravitational force due to the weight of the powder in the chute and inter-particle frictional forces. When this occurs, the seal in the inclined chute can be broken causing a rush of airflow from the CFB riser into the BFB, which can carry bed material with it. Indeed, this phenomenon was observed experimentally under certain operating conditions; that is, bed material flowed from the dense zone in the CFB riser bottom section to the BFB in pulses along the upper surface of the bed within the chute. This has also been observed by other researchers (O'Dea et al., 1990a,b). Chute bypass should be avoided in order to maintain the gas seal between the CFB and BFB by ensuring that there are enough solids in the chute such that the gravitational force due to the weight of the powder is sufficient to overcome the opposing force produced by the CFB-BFB pressure-drop.

An indication of chute bypass is the degree of fluctuation in pressure drop over the CFB riser bottom section (or the riser bottom section pressure drop). In Fig. 5.3, the riser bottom section pressure drop against time is presented when solids are circulating in the system. Two different sets of operating conditions were investigated; one which resulted

in relatively steady flows with no chute bypass, the other which resulted in chute bypass. Fig. 5.3 shows that, during chute bypass, the riser bottom section pressure drop ΔP_{br} fluctuated significantly between 1500 and 2100 Pa with respect to time, with a standard deviation of 139 Pa. The periodic manner of the bypass flow from the dense zone into the BFB (Fig. 5.2) is the reason for the fluctuation in the riser bottom section pressure drop ΔP_{br} (Fig. 5.3). Much less fluctuation (between 2200 and 2400 Pa and standard deviation of 70 Pa) occurs when there is no chute bypass.

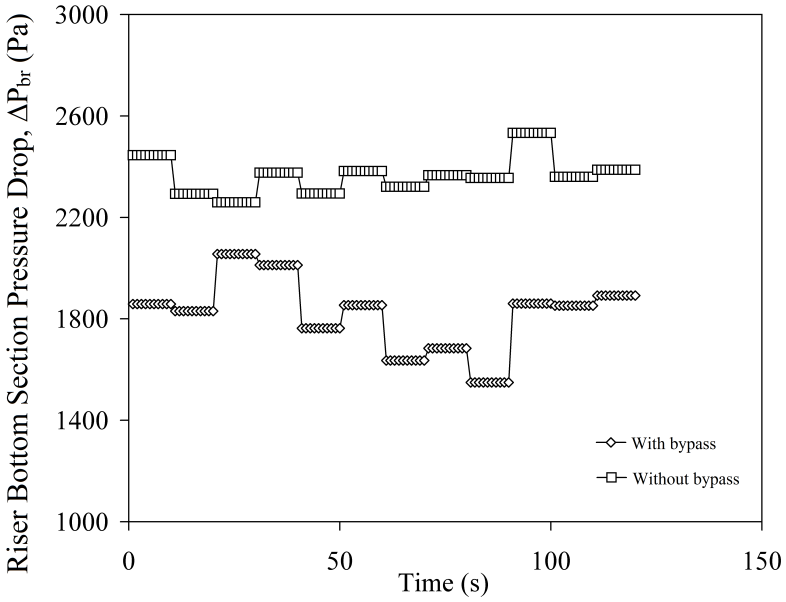

Fig. 5.3: Fluctuation of riser dense zone pressure drop with respect to time in two different situations: with or without chute bypass.

Fig. 5.4 shows the CFB-BFB pressure drop, ΔP_{CB}, (with location of pressure taps shown in Fig. 5.1) versus the BFB airflow rate during chute bypass with no solids in the system. When the BFB airflows is increased, the CFB-BFB pressure drop decreases which indicates how the BFB airflow can be changed to alter the driving force for chute bypass. Fig. 5.4 shows that the CFB-BFB pressure drop ranges between 40 and 60 Pa over the range of BFB airflow tested. This pressure difference between the CFB and the BFB represents the magnitude of the driving force for chute bypass in the DFB cold model.

In this work, the occurrence of chute bypass was identified by visual observations during the experimental runs and from measurements of the chute pressure drop,

especially the magnitude of the time-averaged fluctuation. Based on these assessments, boundaries for steady state operation of the DFB were determined, which are discussed in the next section.

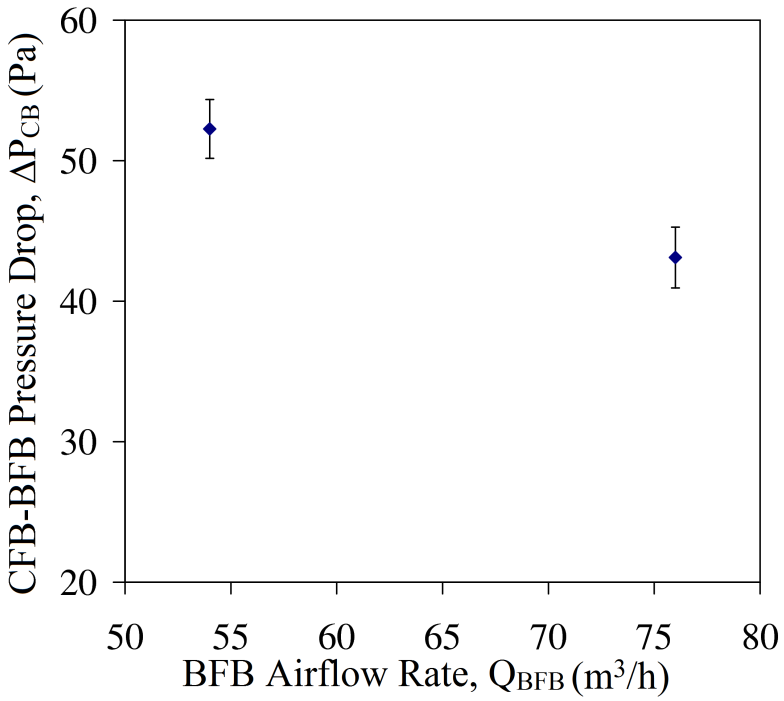

Fig. 5.4: Pressure drop between the CFB riser and the BFB during the chute bypass versus BFB airflow rates. (Q_{pri} 54 m^3/h; Q_{sec} 324 m^3/h; Q_{ls} 5 m^3/h, Q_{ch} was shut off.)

5.3.2 Operational Regime of the Dual Fluidized Bed with Copper as Bed Material

Fig. 5.5 shows the operational map for the DFB plant. Region F is the steady state operating region of the plant. Region F' is the hypothetical steady state operating region of the plant, already shown in Chapter 3 (Fig. 3.3). This hypothetical region could not be confirmed for steady state in this work due to equipment operating limits.

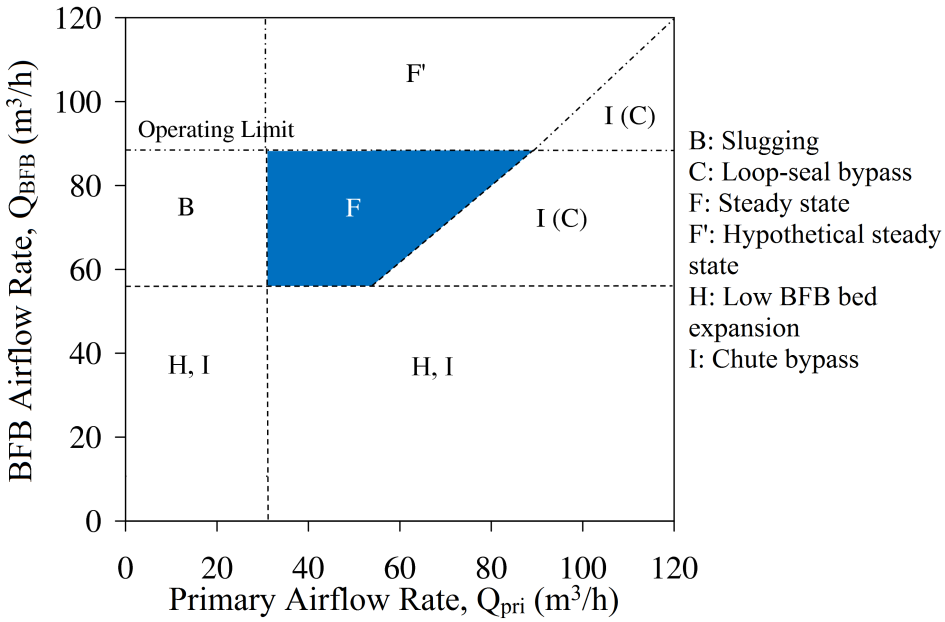

Fig. 5.5: Operational map of the dual fluidized bed plant. Q_{sec} 324 m^3/h; Q_{ls} 5 m^3/h; Q_{ch} 5 m^3/h.

Region H is where the BFB airflow rate is insufficient to expand the bed material to the opening of the chute and chute bypass occurs. Under this condition, there is virtually no flow of solid material from the BFB to the CFB riser through the chute. When the BFB airflow rate is at 54 m^3/h, the bed expands to the height of the chute. Once this bed expansion is achieved, solid material flows through the inclined chute to the dense zone of the CFB. Region B is when the CFB riser primary airflow rate is lower than 32 m^3/h and the DFB operates in a slugging regime, leading to unsteady state operation. Region I is where the CFB primary airflow rate is high enough relative to the BFB airflow which increases the CFB-BFB pressure drop (ΔP_{CB}) such that it is sufficient to result in significant chute bypass. Region I also occurs simultaneously with Region H, since the bed expansion is not enough to fill the chute with material, leading to bypass of gas from the riser to the BFB. As mentioned before, in the actual DFB gasifier, chute bypass decreases the combustion efficiency of the biomass chars in the CFB riser due to a loss of airflow and decreases bed material inflow. The gasification efficiency of the BFB gasifier is also reduced due to the additional gas flow from chute bypass, which dilutes the producer gas.

When the BFB airflow rate (Q_{BFB}) is low such that chute bypass occurs, and the loop-seal airflow rate (Q_{ls}) is excessively high another unsteady state scenario can arise,

denoted by Region C in Fig. 5.5. During chute bypass, solids flow rate from the BFB to the CFB riser dense zone is low, and hence the solids recirculation rate throughout the system is low, with most of the bed material residing in the BFB. The reduced solids flow rate is insufficient to replenish the solids in the loop-seal, especially when the loop-seal airflow rate is high. Under these conditions, the amount of solids in the loop-seal can be reduced to the point that the gas seal breaks, allowing some of the BFB airflow to bypass through the loop-seal and to leak out through the top of the cyclone. This is Region C of Fig. 5.5 (first mentioned in Chapter 3) and occurs if two conditions are satisfied: when chute bypass occurs (Region I) and when the loop-seal airflow rate is excessive.

Having experimentally determined the operational map for the DFB system, more experiments were conducted to investigate the effect of BFB airflow rate and chute airflow rate on the solids core flow rate, solids outflow rate and the pressure drop in the system.

5.3.3 Effect of BFB and Chute Airflow on Pressure Drops, Solids Core Flow and Outflow with Copper as Bed Material

Figs. 5.6 to 5.11 show the effects of BFB airflow and chute airflow on the pressure drops (Figs. 5.6 to 5.8 and 5.10), solids core flow rate (Fig. 5.9) and solids outflow rate (Fig. 5.11) when operating the DFB in Region F and Region I (Fig. 5.5). In these experiments, the CFB primary airflow rate (Q_{pri}), secondary airflow rate (Q_{sec}), and the loop-seal airflow rate (Q_{ls}) were constant at 54, 324 and 5 m^3/h respectively. A dashed-lined box is used in the figures to indicate the operating conditions when the chute bypass (Region I) occurred.

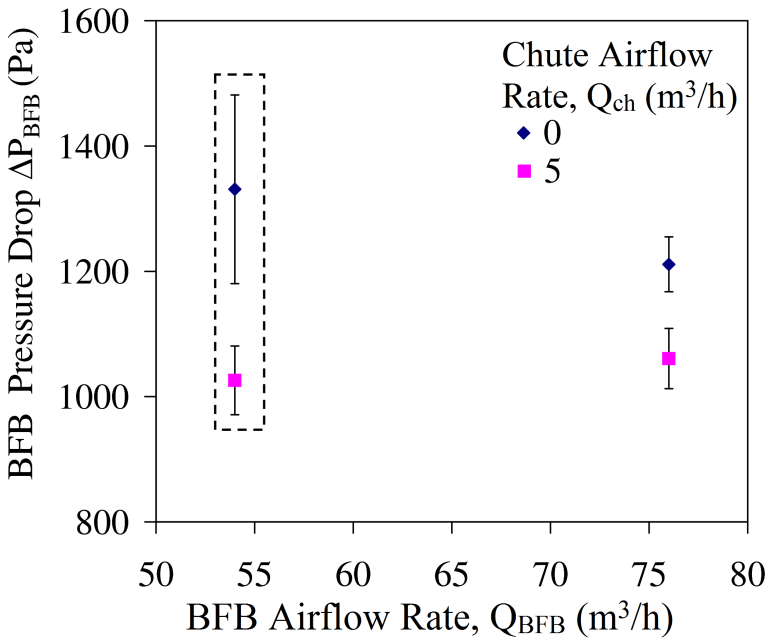

Fig. 5.6: BFB pressure drop as a function of BFB airflow rate and chute airflow rate. (Q_{pri} 54 m^3/h; Q_{sec} 324 m^3/h; Q_{ls} 5 m^3/h). The dashed-line box shows the operating conditions when chute bypass occurs.

Fig. 5.6 shows that pressure drop in the BFB column as a function of BFB flow rate in which the chute bypass is also illustrated. Form the results it is seen that the chute bypass occurs at a low BFB airflow of 54 m^3/h and this is not affected by whether there is chute airflow or not. At the higher BFB airflow rate of 76 m^3/h, the fluidized bed in the BFB expands such that sufficient solids flow into the chute to form a gas seal between the BFB and CFB. When the chute bypass is prevented, the driving force for the chute bypass that is the CFB-BFB pressure drop decreases at the higher BFB airflow as shown in Fig. 5.4. The unsteady nature of the system at lower BFB airflows when chute bypass occurs is highlighted by the larger pressure drop fluctuations with time (indicated by the magnitude of the error bars) compared with when a gas seal is formed as shown in Fig. 5.3. This is especially clear in the case when there is no chute airflow to aid solids flow in the direction of the CFB (Fig. 5.6). Taking the experimental fluctuations into account, the BFB pressure drop is observed in Fig. 5.6 to be fairly constant with a change in BFB airflow from 54 to 76 m^3/h. When the chute airflow is increased, the BFB pressure drop decreases. This is due to change in the steady-state ratio of total solids in the CFB and BFB, with a shift in total solids towards the CFB.

Fig. 5.7 measured results of chute pressure drop as a function of BFB air flow rate

with and without chute airflow. From these results, it can be seen that the chute pressure drop increases with both BFB airflow rate and the chute airflow rate, which indicates that the chute is filled with more solids at the higher BFB airflow rate and with chute airflow rate (5 m^3/h). Under these conditions, the weight of the solids in the chute is sufficient to overcome the chute-bypass driving force that is the CFB-BFB pressure difference, and thus the plant operates under steady state (Region F in Fig. 5.5). With an increase in solids flow rate through the chute, the dense zone in the CFB has more solids, which increases the riser bottom section pressure drop (Fig. 5.8). The higher amount of solids in the dense zone results in a greater entrainment of solids to the transport zone (and the riser upper section), thus the solids core flow rate increases (Fig. 5.9). Consequently, the pressure drop in the CFB riser upper section (or the riser upper section pressure drop) also increases, as shown in Fig. 5.10. Fig. 5.11 shows that the solids outflow rate also increases with the BFB airflow rate and chute airflow rate, reflecting the increase in the solids core flow rate. Chute bypass occurs when the BFB airflow is at 54 m^3/h, as indicated by the low chute pressure drop (Fig. 5.7). In this case, there is an insufficient weight of bed material in the chute to counteract the opposing force on the bed material due to the pressure difference between the CFB and BFB.

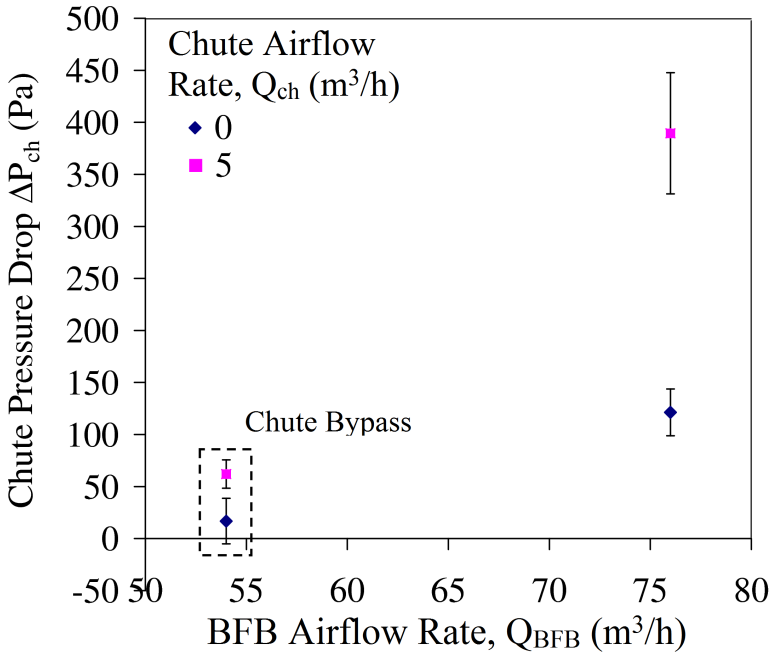

Fig. 5.7: Chute pressure drop with varying BFB airflow rate and chute airflow rate. (Q_{pri} 54 m^3/h; Q_{sec} 324 m^3/h; Q_{ls} 5 m^3/h).

When there is no chute airflow, the solids in the chute are not fluidized, hence, the inter-particle frictional forces are higher and the solids mass flow rate through the inclined chute is lower. Therefore, the solids core flow rate in the CFB and the solids outflow rate from the CFB are lower compared to the corresponding values when chute airflow is applied. Fig. 5.7 also shows that, during chute bypass, the measured chute pressure drop, ΔP_{ch}, decreases to 20-80 Pa. These values are almost in the same range as the CFB-BFB pressure drop ΔP_{CB} with no solids loaded (Fig. 5.4). This is evidence that chute bypass occurs when the force due to the weight of the solids in the chute is insufficient to counteract the force due to the pressure drop across the CFB-BFB. Therefore, chute pressure drop is clearly a useful indication of the likelihood of chute bypass. When its value reduces to a critical range of values or lower, which lie between 20 to 80 Pa in the cold DFB model of this work, chute bypass is likely to occur.

With an increase in the chute airflow, an additional force is provided to overcome the inter-particle force within the bed material in the chute, enhancing solids flow in the chute towards the CFB riser end of the chute. In this way, a more effective gas seal between the CFB riser and the BFB is formed by introducing the chute airflow because the bed material fills the chute more effectively towards the CFB end. With an improved gas seal, the chute pressure drop and riser bottom section pressure drop increase, and so do the solids core flow rate , the riser upper section pressure drop and solids outflow rate for reasons mentioned earlier (Figs. 5.7, 5.8, 5.9, 5.10 and 5.11, respectively). It should be noted that the increase in chute airflow reduces the chute bypass, but does not eliminate the reverse flows entirely, if the BFB airflow is too low. There is no chute bypass when the BFB airflow at the higher value of 76 m^3/h, and as a result, the pressure drops and solids mass flow rates are higher, as can be seen in Figs. 5.7 to 5.11. This is due to the combined effect of a more expanded bed in the BFB at higher BFB airflow, and a lower driving force for chute bypass, as indicated in Fig. 5.4.

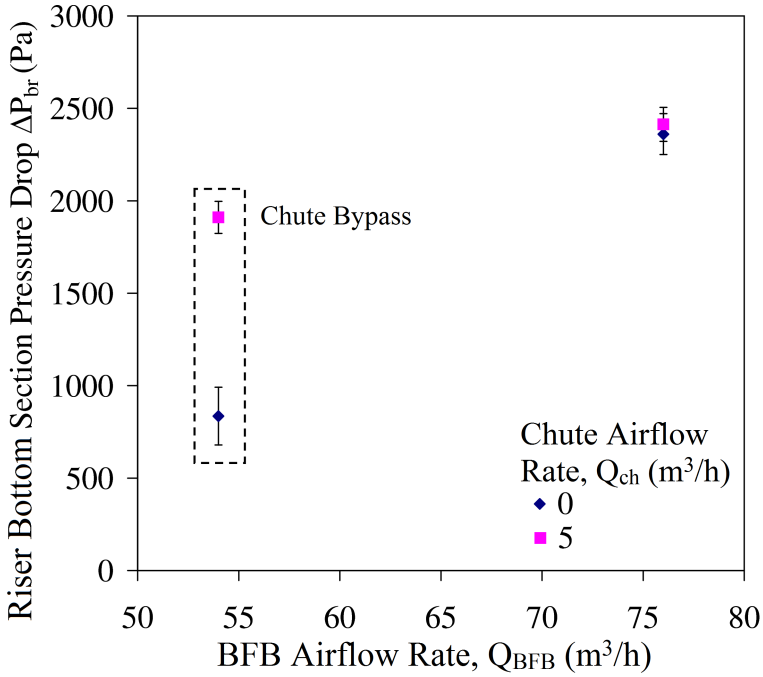

Fig. 5.8: Riser bottom section pressure drop with varying BFB airflow rate and chute airflow rate. Q_{pri} at $54m^3$/h; Q_{ls} at $5m^3$/h

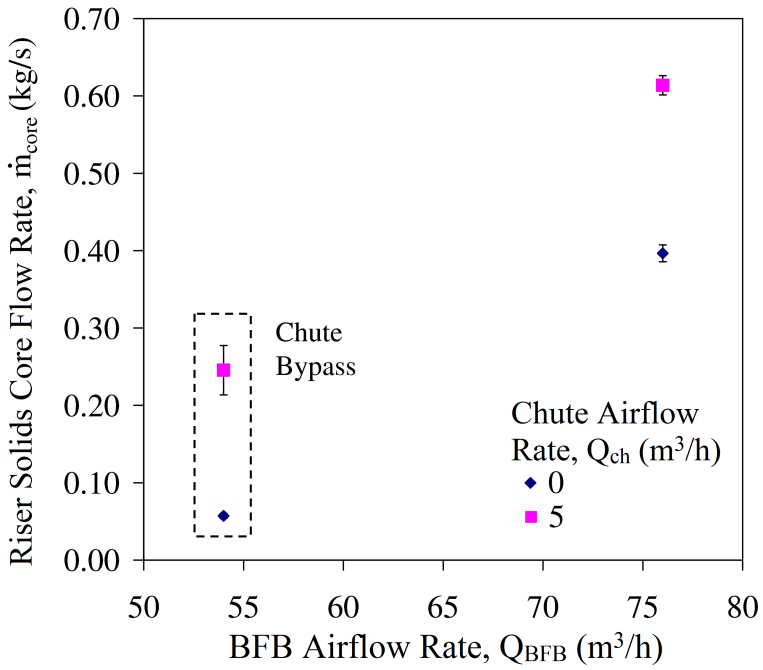

Fig. 5.9: The riser solids core flow rate ($\dot{m}_{core}$) as a function of BFB airflow rate (Q_{BFB}) and chute airflow rate (Q_{ch}). (Q_{pri} 54 m^3/h; Q_{sec} 324 m^3/h; Q_{ls} 5 m^3/h).

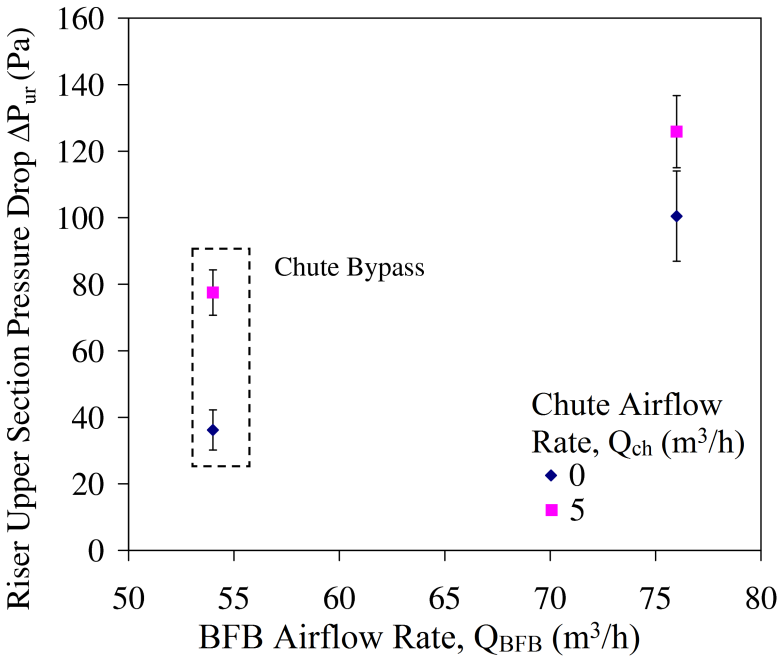

Fig. 5.10: Riser upper section pressure drop as a function of BFB airflow rate and chute airflow rate. (Q_{pri} 54 m^3/h; Q_{sec} 324 m^3/h; Q_{ls} 5 m^3/h).

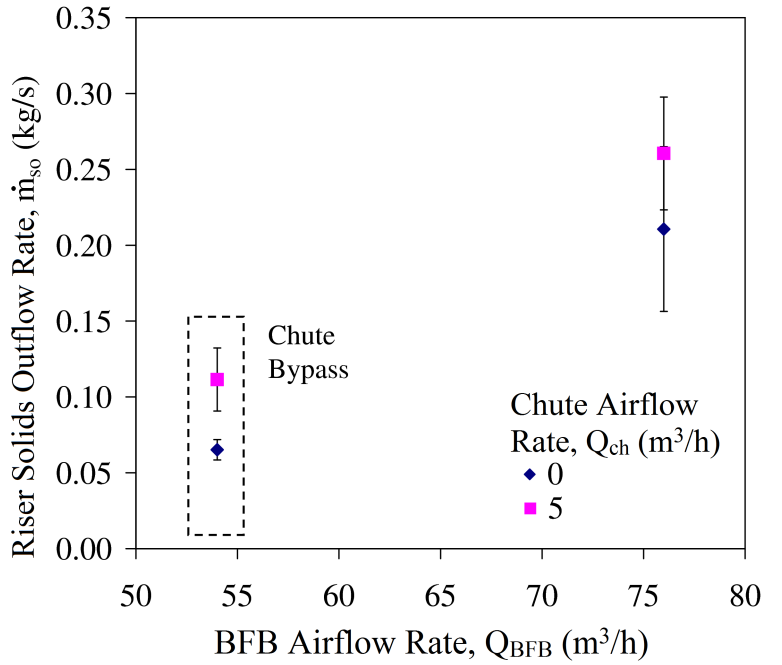

Fig. 5.11: The riser solids outflow rate ($\dot{m}_{so}$) as a function of BFB airflow rate (Q_{BFB}) and chute airflow rate (Q_{ch}). (Q_{pri} 54 m^3/h; Q_{sec} 324 m^3/h; Q_{ls} 5 m^3/h).

The above results indicate that increasing the BFB airflow increases the amount of solids in the inclined chute, thus improving the gas seal efficiency of the chute. However, increasing the BFB airflow in the cold model translates to an increase in steam flow rate to the BFB reactor under high temperature conditions in a DFB biomass gasification plant. High steam flow rate will increase the steam-to-biomass ratio, resulting in a decrease in reaction temperature and gasification efficiency (Lv et al., 2004). Therefore, optimum operation conditions need to be sought by considering the requirements of improved hydrodynamics by ensuring a proper gas seal in the chute through an increase in the BFB steam flow rate while still maintaining a steam-to-biomass ratio that provides high gasification efficiency. Another option is to lower the opening of the chute at the BFB end closer to the BFB airflow distributor to ensure it is submerged by the bed material to provide a better gas seal. A third option is to replace the incline chute with a loop-seal, which provides a good gas seal and a better control of the solids circulation from the BFB to the CFB riser. However, space and geometrical constraints need to be considered if the loop-seal were to be installed in the DFB.

5.3.4 Hydrodynamics of Binary Mixtures in DFB: Effect of Secondary Material Addition on Pressure Drops and Solids Core Flow

Experimental results from the tests in the cold DFB model with mixture of binary solids (MDPE pellets and copper particles) are shown in Figs. 5.12 to 5.19. Fig. 5.12 shows that the measured chute pressure drop increases significantly when MDPE pellets are added into the DFB compared to the corresponding results without the MDPE pellets. It was observed that the MDPE pellets quickly segregate after they are introduced into the DFB, and occupied the upper regions of the chute, leading to a better gas seal and hence a higher chute pressure drop.

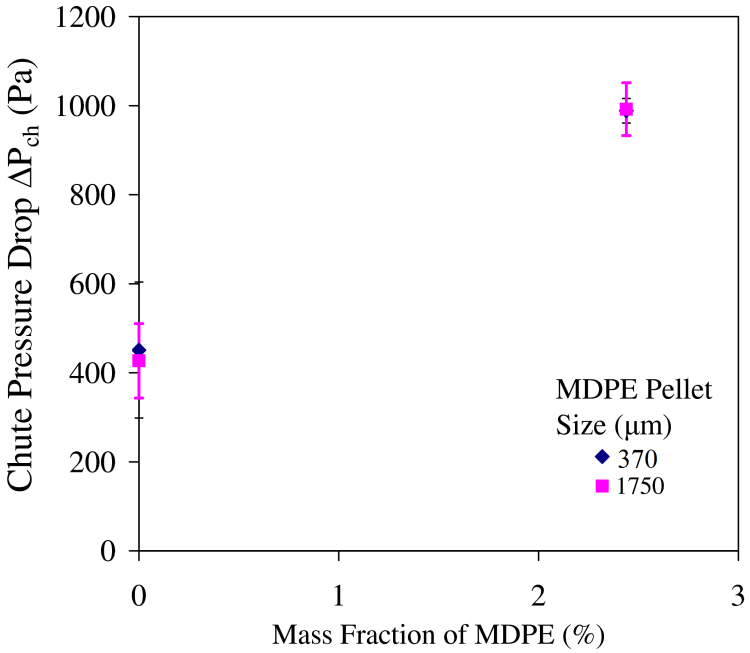

Fig. 5.12: Effects of adding two different sized MDPE pellets in the system on chute pressure drop (Q_{pri} 54 m^3/h; Q_{sec} 324 m^3/h; Q_{BFB} 76 m^3/h; Q_{ls} 5 m^3/h; Q_{ch} 5 m^3/h).

The effect of adding the MDPE pellets on the riser bottom section pressure drop is shown in Fig. 5.13 in which the influence of the MDPE pellet size is also demonstrated. Different trends for the riser bottom section pressure drop in the CFB riser have been observed for two different sizes of the added MDPE pellets. The riser bottom section pressure drop decreases significantly with the addition of 1750 μm MDPE pellets, while this pressure drop remains almost constant when 370 μm MDPE pellets are added to the system.

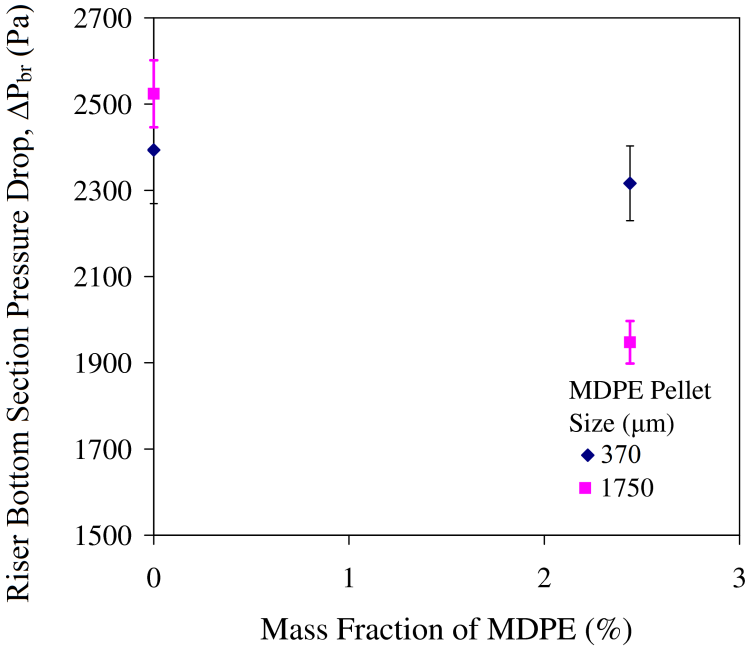

Fig. 5.13: Effects of adding two different sized MDPE pellets on the riser bottom section pressure drop. (Q_{pri} 54 m^3/h; Q_{sec} 324 m^3/h; Q_{BFB} 76 m^3/h; Q_{ls} 5 m^3/h; Q_{ch} 5 m^3/h).

As pointed out above, the MDPE pellets quickly segregated from the copper particles once being introduced into the DFB, occupying the upper regions of the inclined chute due to their lower particle density (941 kg/m^3) compared to copper (8940 kg/m^3). Observations show that the 1750 μm MDPE pellets occupied a larger volume of the chute than the 370 μm pellets. Therefore, the 1750 μm MDPE pellets more effectively obstructed the flow of copper particles from the BFB into the CFB riser than the 370 um pellets did, which significantly decreased the riser bottom section pressure drop. Since the bulk density for the 370 μm MDPE pellets is higher (908 kg/m^3), the volume occupied by the smaller MDPE pellets (for the same amount of mass) is lower such that the smaller pellets did not obstruct the flow of copper to the same extent as the larger pellets (688 kg/m^3), and therefore the riser bottom section pressure drop decreased slightly.

Fig. 5.14 shows further evidence of the obstruction by the large MDPE pellets in the chute, indicated by the decrease in the copper solids core flow at a riser height of 2.55 m when 1750 μm MDPE pellets were added. However, when the 370 μm MDPE pellets were added, the copper solids core flow rate increased slightly rather than decreasing. The same trend for the CFB riser upper section pressure drop as that for the CFB bottom

section pressure drop is observed as shown in Fig. 5.15 which shows that the CFB riser upper section pressure drop was reduced after the addition of 1750 μm MDPE pellets, while the riser upper section pressure drop was virtually not changed after addition of 370 μm MDPE pellets.

Fig. 5.16 shows the effect of adding the MDPE pellets on the BFB pressure drop. The significant increase in the BFB pressure drop indicates that the addition of the MDPE pellets effectively increases the steady-state amount of solid particles (mainly copper particles) in the BFB, due to the significant increase in the pressure drop over the BFB. However, the MDPE pellet size did not show noticeable influence on the BFB pressure drop although the MDPE size has substantial effects on the chute pressure drop and the CFB riser pressure drops. Further experiments are required to determine the effects of adding MDPE pellets on the flow hydrodynamics in the loop-seal.

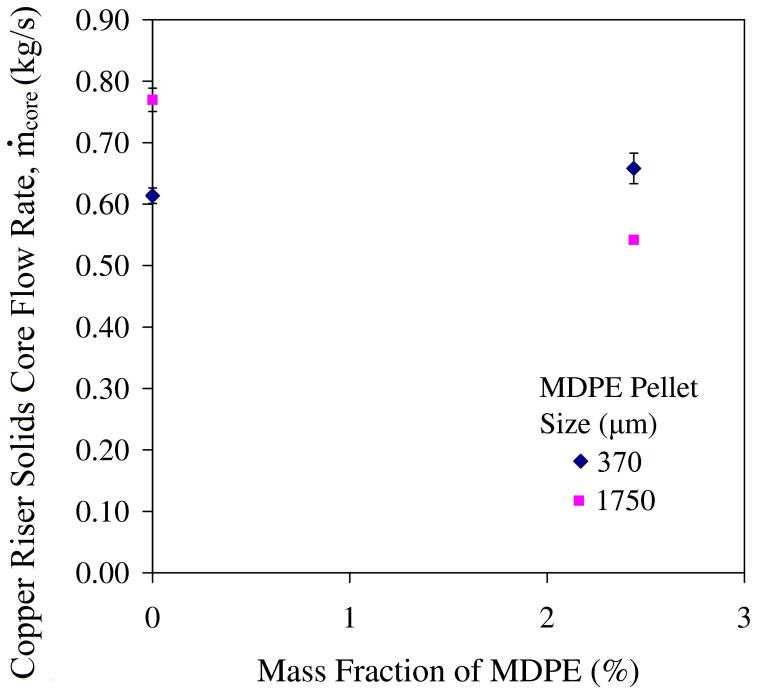

Fig. 5.14: Effects of adding two different sized MDPE pellets on the copper riser solids core flow rate at a riser height of 2.55 m. (Q_{pri} 54 m^3/h; Q_{sec} 324 m^3/h; Q_{BFB} 76 m^3/h; Q_{ls} 5 m^3/h; Q_{ch} 5 m^3/h).

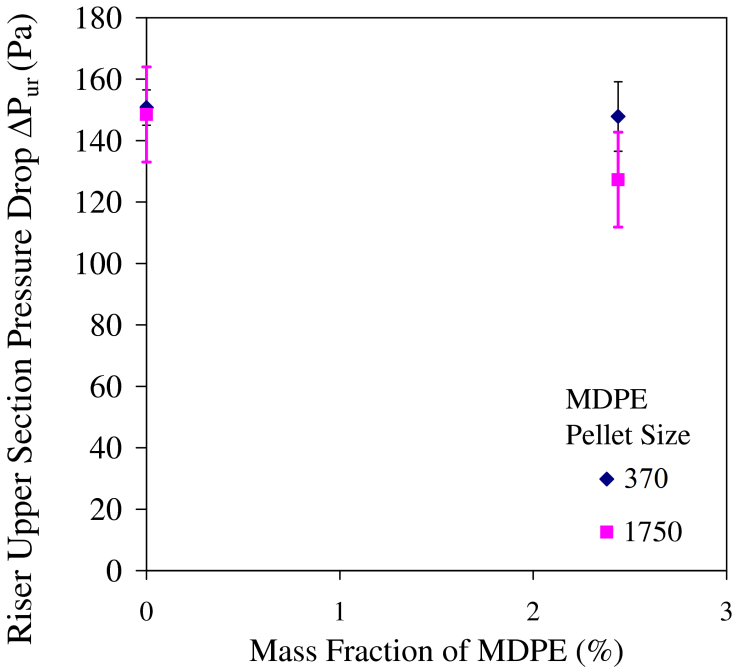

Fig. 5.15: Effects of adding two different sized MDPE pellets on the riser upper section pressure drop. (Q_{pri} 54 m^3/h; Q_{sec} 324 m^3/h; Q_{BFB} 76 m^3/h; Q_{ls} 5 m^3/h; Q_{ch} 5 m^3/h).

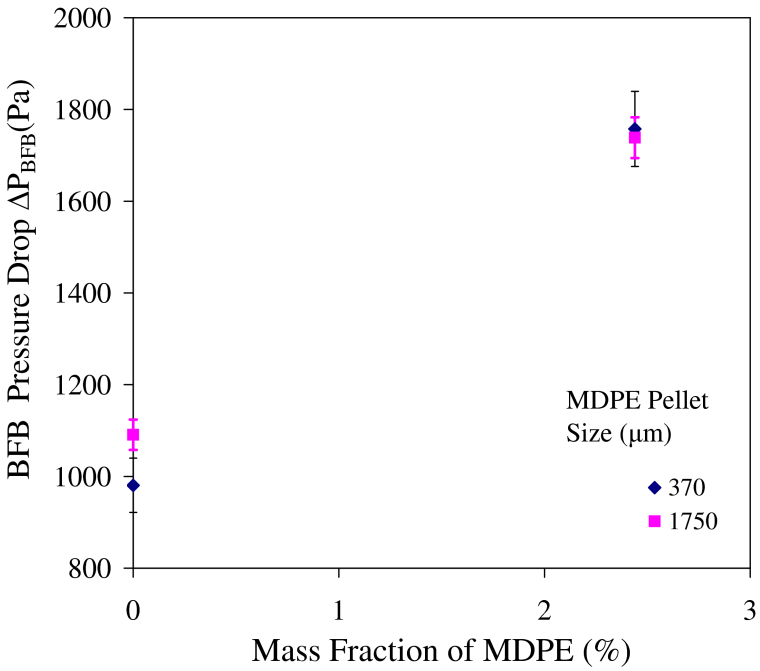

Fig. 5.16: Effects of adding two different sized MDPE pellets on the BFB pressure drop. (Q_{pri} 54 m^3/h; Q_{sec} 324 m^3/h; Q_{BFB} 76 m^3/h; Q_{ls} 5 m^3/h; Q_{ch} 5 m^3/h).

The effects of adding the secondary material into a binary mixture has been reported in previous studies (Chen et al., 2006) in which it was found that the BFB pressure drop was reduced as a result of decreased effective density due to the lower density of one of the materials. However, the observations from the current study that the pressure drop is increased in part of system (chute and BFB) while decreased in the other part of the system (riser bottom section), have not been documented before.

Fig. 5.17 shows the radial profiles of the local upward solids fluxes of 370 μm MDPE pellets and copper particle at a riser height of 2.55 m. The corresponding results for adding the 1750 μm MDPE pellets are shown in Fig. 5.18. In these two figures, the error bars indicate the fluctuation of the measurements. There was a higher level of fluctuation in the local solid flux for the 370 μm MDPE pellet, because the wide size distribution of these particles (from 176 to 704 μm) made it difficult to completely separate them from the copper particles (88 to 249 μm) during the sieving process. Any deviation in mass when sieving the 370 μm MDPE pellets from the copper particles would cause an increased error in the MDPE pellet flux profile. However, the size distribution of the 1750 μm MDPE pellets was much narrower and the size was much larger than copper particles, therefore the 1750 μm MDPE pellets could be effectively separated from the copper particles. Taking into account the fluctuation of the measurements, the local upward solid flux for both sizes of MDPE pellets are comparable (Fig. 5.17 and 5.18).

Fig. 5.17 also shows that both the MDPE and copper solid fluxes increase as the BFB airflow rate increases. With the higher BFB airflow rate, the bed material in the BFB expands to a higher position above the chute, and allows more material to flow into the CFB riser through the chute; thus solids flux in the riser increases. A comparison of Figs. 5.17 and 5.18 shows that the copper solids flux is lower when 1750 μm pellets are used. This is consistent with earlier findings, where the addition of 1750 μm pellets decreases the riser bottom and upper section pressure drop and the copper solids core flow (Figs. 5.13, 5.15, 5.14), as the pellets obstruct the mass flow of copper in the inclined chute.

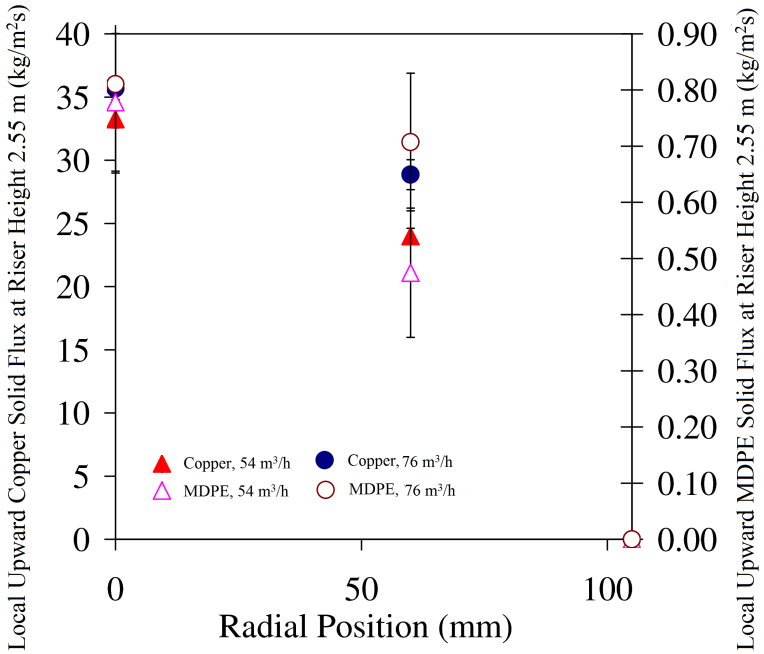

Fig. 5.17: Radial profile of solids flux for copper particles and 370 μm MDPE pellets. Note the different scales for the copper particles (left-hand y-axis) and the MDPE pellets (right-hand y-axis) (Q_{pri} 54 m^3/h; Q_{sec} 324 m^3/h; Q_{ls} 5 m^3/h; Q_{ch} 5 m^3/h).

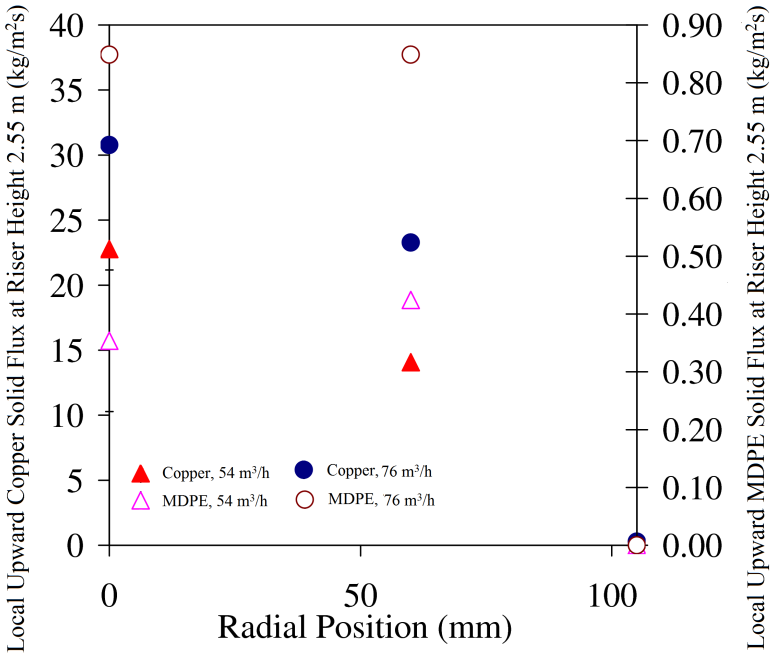

Fig. 5.18: Radial profile of solids flux for copper particles and 1750 m MDPE pellets. Note the different scales for the copper particles (left-hand y-axis) and the MDPE pellets (right-hand y-axis). (Q_{pri} 54 m^3/h; Q_{sec} 324 m^3/h; Q_{ls} 5 m^3/h; Q_{ch} 5 m^3/h).

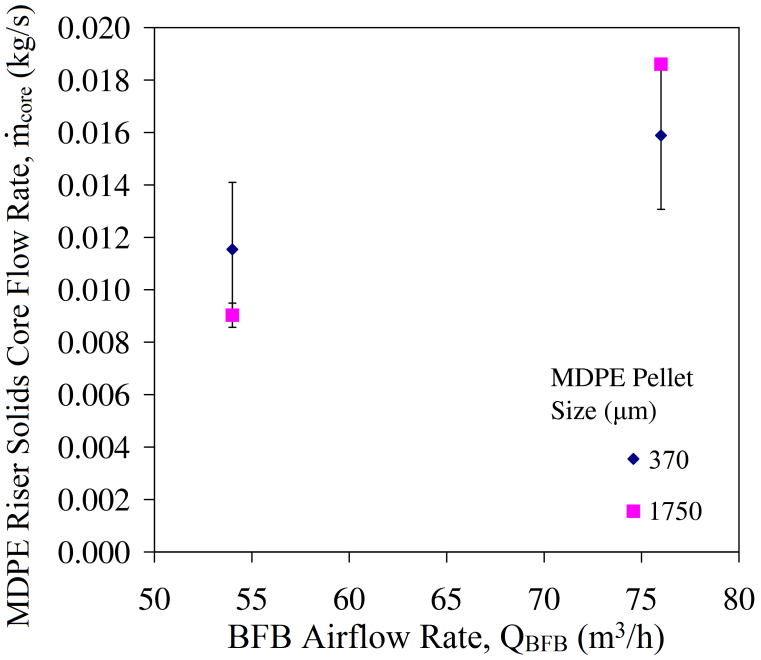

Fig. 5.19: Variation of MDPE pellets solids core flow rate as affected by the BFB airflow rate. (Q_{pri} 54 m^3/h; Q_{sec} 324 m^3/h; Q_{ls} 5 m^3/h; Q_{ch} 5 m^3/h).

Fig. 5.19 shows that the MDPE solids core flow rate in the CFB riser generally increases with increasing BFB airflow rate, which is consistent with the findings that copper particle flow rate also increases with increasing BFB airflow rate.

It should be noted that the terminal velocity for the 1750 μm MDPE pellets is calculated to be 4.55 m/s (from Eqs (4.17) and (4.18)), which is much higher than the average gas superficial velocity of 3.03 m/s in the CFB riser at the DFB operating conditions (Q_{pri} 54 m^3/h; Q_{sec} 324 m^3/h; Q_{BFB} 76 m^3/h; Q_{ls} and Q_{ch} 5 m^3/h). However, it was observed that the 1750 μm MDPE pellets were still conveyed upwards in the CFB, sometimes floating at random heights in the CFB before being either entrained out of the CFB, or being entrained into the downward flowing annular wall layer. The 1750 μm pellets were propelled upwards by the high velocity jets produced by the secondary air injectors. The high velocity jets, coupled with clustering effects, cause a long solid particle acceleration zone in the CFB as mentioned in Chapter 4.

5.4 Conclusions

An operational map for steady state operation of the DFB was plotted to establish boundaries for the CFB primary and the BFB airflows within which steady operation can be achieved. For steady state operation, the chute pressure drop must be sufficiently high to prevent chute airflow bypass from the CFB to the BFB. Such airflow bypass results in pulses of bed material flows within the chute in the direction toward the BFB, leading to large fluctuations in riser bottom section pressure drop and a general unsteady state behavior of the entire system. To improve the gas seal efficiency and reduce or eliminate chute bypass, the chute airflow and BFB airflow rate should be sufficiently high.

From the experiments of binary mixture in the DFB, it was found that the addition of the larger MDPE pellets of size 1750 μm partially obstructed the flow of copper particles from the BFB into the CFB dense zone through the chute, resulting in a decrease of the riser bottom section pressure drop and copper solids core flow rate. The smaller MDPE pellets with particle size 370 μm had less effect. This suggests that there is a limit to the size of biomass particulates that can be added into the BFB in order to avoid chute obstruction. The increase in airflows to the BFB and the chute resulted in an increase of both copper particles and MDPE pellet mass flows through the system.

Chapter 6

Computational Fluid Dynamics Modeling of CFB Cyclone Separator

As part of the dual fluidized bed (DFB) gasification plant, the circulating fluidized bed (CFB) cyclone functions as a separator to separate solids from the gas stream (flue gas). After this, the solids flow down to the standpipe and then into the loop seal before they are re-circulated to the bubbling fluidized bed (BFB). The solids flow rate into the BFB is directly related to the separation efficiency of the cyclone. Thus, the functionality of the CFB cyclone is crucial to the hydrodynamics of the DFB. In this part of the study, the usefulness Computational Fluid Dynamics (CFD) as a design tool was demonstrated to provide confidence about the accuracy of the approach for future performance optimization and design improvement of cyclone separators in industrial DFB plants.

6.1 Introduction

CFD has been used widely to simulate the flow in cyclones (Cortés & Gil, 2007; Utikar et al., 2010). In these simulations, different turbulence models can be adopted. Shalaby et al. (2005) found that the k-ε turbulence model was not accurate in predicting the gas velocity profiles in a cyclone due to the assumption of isotropic eddy viscosity. Therefore this model is not valid for swirling flows due to the limitation placed on the development of anisotropy in the turbulence. Hoekstra et al. (1999) found that the Reynolds Stress Model (RSM), another turbulence model, produced more accurate

simulations of the flow in a cyclone, since this model allows anisotropy in turbulence to develop more realistically. Qian & Wu (2009) performed simulations on the effects of the inlet angle on the separation performance of the cyclone. They validated their simulations by comparing the predicted cyclone pressure drop with experimental measurements. These works show the accuracy of CFD for modelling flows in the cyclone. In view of this, it is the intention of the current study to demonstrate the usefulness of CFD as a design tool for industrial gasifier cyclones. As mentioned earlier in Chapter 2, there is a variation in the modelling approaches used for simulating the flows in the cyclone. The number of nodes for the mesh was found to range from 29000 to 7.7×10^{6} in the literature (Jiao et al., 2007; Karagoz & Kaya, 2007; Wan et al., 2008; Xiang & Lee, 2008; Derksen, 2003). In addition, the time step used by different researchers in transient simulations of a cyclone ranged from 1×10^{-4} to 1×10^{-5} s (Derksen, 2003; Wan et al., 2008), however, some studies did not give information about the time step used (Jiao et al., 2007; Karagoz & Kaya, 2007; Xiang & Lee, 2008). There is an uncertainty surrounding the number of nodes and time step required to obtain an accurate and converging solution for simulating the flows in the cyclone separator. This study aims to address these uncertainties by developing an appropriate mesh and choosing an appropriate time-step to ensure good numerical accuracy in the CFD simulations of flows in a cyclone.

Wang et al. (2006) have simulated particle flows in cyclones. They showed that inter-particle interaction effects occur even at low solids concentrations. The inter-particle effects can be incorporated in an Eulerian-Eulerian modelling approach (also known as the Eulerian model) which treats the solid particulate phase as another continuous phase that coexists and interacts with the gas phase. Initial efforts in this study using the Eulerian model to take into account the inter-particle interactions in the cyclone simulations proved to be difficult due to the high computational time required to ensure numerical stabilities. A simplified approach was eventually adopted by using the Eulerian-Lagrangian model. In the Eulerian-Lagrangian model, particles are modelled individually, with trajectories being obtained by integrating the momentum equation for individual particles. Interactions could not be modelled using the commercial CFD software adopted in this work, and therefore particle separation could not be realistically

simulated. However, these CFD simulations are useful to track particles through the cyclone, thus the simulation results can be used in providing an explanation for erosion in cyclones.

In this study, the value of the CFD cyclone design tool was demonstrated by validating CFD simulations of flow in the cyclone investigated experimentally by Derksen (2003). The work of Derksen (2003) was chosen due to the approximate geometric and dynamic similarity of the cyclone used in that work and the cyclone used in this work. In the development of the CFD model, decisions were made on the appropriate choice of turbulence model to be adopted in the simulations, the number of nodes required for the grid, and the time step necessary for an accurate transient prediction of the fluid flow in the cyclone. Once the CFD model was shown to accurately predict the velocity field within the Derksen cyclone, it was then used to predict the flow in the cold model CFB cyclone separator used in this work. The most accurate turbulence model found in the base-case study was employed in these simulations. A similar mesh as developed in the base case simulations was used as the starting point for a grid-independence check in the CFB cyclone-separator simulations. The pressure drop of the CFB cyclone was compared to the experimental values from the cold model plant for validation. It has been observed and reported by McKinnon (2009) that in the hot gasifier runs carried out in the pilot scale DFB at University of Canterbury, the CFB cyclone separator suffers high erosion near the inlet section (highlighted in Chapter 1). Thus, a preliminary study was performed to relate the impact of particle-wall collisions on erosion of the cyclone walls.

6.2 CFD Theory

6.2.1 Turbulence Modelling

Generally, fluid flows in most engineering applications are turbulent, which implies a random fluctuating state of fluid motion, and hence a continuous change in velocity and pressure with respect to time within the flow (Versteeg & Malalasekera, 2007). The most common method of modelling turbulence is to apply Reynolds averaging to the Navier-Stokes Equations, and use algebraic or transport equations to model the resultant

Reynolds stresses that appear (Chung, 2002; Versteeg & Malalasekera, 2007; Yu et al., 2008). These Reynolds stresses effectively represent the fluctuations in the flow due to turbulent eddies. The turbulence models tested in this work were the k-epsilon (k-ε) model and the Reynolds stress model (RSM). The k-epsilon model uses algebraic expressions for the Reynolds stresses, based on a Boussinesq's eddy-viscosity concept. Two additional transport equations are introduced to represent the kinetic energy of the turbulence and the rate at which turbulence kinetic energy is dissipated (Benyahia et al., 2005; Karagoz & Kaya, 2007). The eddy viscosity is assumed to be isotropic, which limits the development of modelled anisotropy in the turbulent flow. In the RSM model, the Reynolds stresses are modelled using separate transport equations to allow the anisotropy to develop more realistically (Chung, 2002; Wang et al., 2006; Versteeg & Malalasekera, 2007). The RSM model has a pressure-strain correlation that was represented in this work through the Speziale, Sarkar and Gatski (SSG-RSM) model (Speziale et al., 1991).

6.2.2 Gas-Solid Flow Modelling

In this study, the Eulerian-Lagrangian model (or more simply the Lagrangian model) was used to model the gas-solid flow in the cyclone. In this approach, the particles are modelled individually, with trajectories being obtained by integrating the momentum equation for individual particles (Cortés & Gil, 2007). The particle trajectories are influenced by the gravitational, drag, and turbulent dispersion forces, hence these forces were included in the momentum equation. Interaction between the gas and the solid phases is important in a cyclone, however these effects were not modelled here essentially because phase interaction physics was not available for Lagrangian modelling in the commercial CFD software (ANSYS-CFX 11) used. Lagrangian particle tracking was conducted only to determine particle tracks through the cyclone in order to explain why certain regions of a cyclone wall are more prone to erosion than others.

6.3 Base Case Cyclone Separator Simulation

6.3.1 Cyclone Separator Dimensionless Parameters

The following equations represent the important dimensionless parameters that characterize a cyclone (Cortés & Gil, 2007): Euler number (Eu_{cy}), Reynolds number (Re_{cy}), Froude number (Fr_{cy}) and Swirl number (Sw).

$$Eu_{cy} = \frac{\Delta P_{cy}}{0.5\rho_g U_{in}^2} \tag{6.1}$$

$$Re_{cy} = \frac{\rho_g U_{in} D_{cy}}{\mu_g} \tag{6.2}$$

$$Fr_{cy} = \frac{U_{in}^2}{g D_{cy}} \tag{6.3}$$

$$S_w = \frac{\pi}{4} \frac{D_{vf} D_{cy}}{A_{in}} \tag{6.4}$$

where U_{in} is the gas inlet velocity to cyclone; A_{in} is the cross-sectional area of the inlet; D_{cy} is the cyclone diameter; D_{vf} is the diameter of vortex finder, ΔP_{cy} is the pressure drop of the cyclone. Fig. 6.1 shows the geometry of the base case cyclone separator (Derksen, 2003) in which the diameter of the cyclone D_{cy} (= D) is 0.29 m, the cross-sectional area of the inlet A_{in} is $0.1D^2$, and diameter of the exit D_{ex}(=0.5D) is 0.145 m. The gas phase in this study was air at 25°C, and the gas inlet velocity to the cyclone (U_{in}) was taken as 16.1 m/s. The dimensionless numbers were evaluated both for the base case cyclone and for the CFB cold model, as shown in Table 6.1.

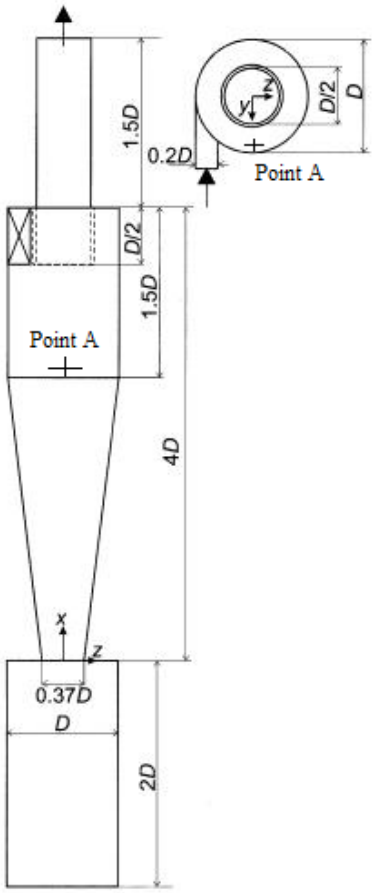

Fig. 6.1: Geometry and coordinate system of the base case cyclone (Derksen, 2003)

Table 6.1: Dimensionless parameters comparison

	Base case cyclone (Derksen, 2003)	Cold model CFB cyclone in this study
Eu	6.37	4.58-5.20
Re_{cy}	280×10^3	$83\text{-}200\times10^3$
Fr_{cy}	91	26-149
S_w	3.93	2.36

As can be seen from Table 6.1, there was a certain level of deviation of the dimensionless numbers between the base case cyclone of Derksen (2003) and the cold model cyclone used in this study. This deviation was unavoidable as it was difficult to match all the dimensionless numbers using only inlet flow as a control parameter. The deviation indicates a difference in flow condition for both cyclones. This implies that it

may not be appropriate to use the same mesh developed in the base-case simulations for the CFB cyclone separator simulations. Therefore, a grid sensitivity check was performed for the cold model cyclone simulations, using the mesh developed in the base-case as a starting point.

In the base case cyclone separator (Derksen, 2003), an obstruction plate was placed just at the upstream of the top outlet (at a distance of $4.84D_{vf}$), with the intention of preventing any subcritical flow at the outlet boundary from interrupting the flow field in the cyclone (Derksen, 2003). This obstruction plate was also included in the CFD simulations carried out in this work.

6.3.2 Set-up for Base Case Cyclone Separator Simulations

The simulations were performed with a commercial CFD software package called ANSYS CFX 11.0. The velocity at the inlet was assumed to have a uniform velocity profile. Derksen (2003) reported that the influence of the inlet velocity profile is not significant on the mean and fluctuating velocities in the cyclone. The outlet (at the top of the vortex finder) was set to an averaged atmospheric pressure boundary. The number of elements for the cyclone was increased from 0.9×10^6 to 1.7×10^6 and 2.7×10^6 respectively, in order to determine whether the solution, using the RSM turbulence model, was grid independent. Due to computer limitations, the number of elements was unable to be increased further significantly above 2.7×10^6. The average length of each element in the cyclone is 1.5mm. Fig. 6.2 shows the top and side view of the 2.7×10^6 mesh.

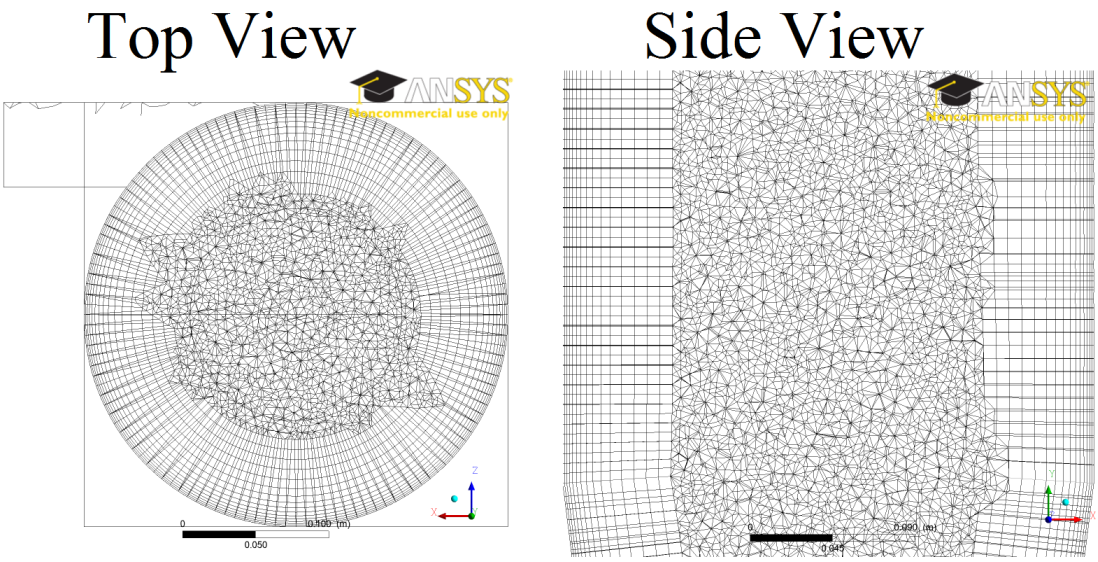

Fig. 6.2: Top and side views of the 2.7×10^{6} mesh for base case cyclone.

As mentioned in Chapter 2, in the cyclone there is a precessing vortex core (PVC) that swings and oscillates across the axis of the cyclone. The fluctuating nature of the PVC is the source of unsteady state behaviour in the cyclone (Cortés & Gil, 2007). Thus, in the CFD simulations, the cyclone was modelled as a transient flow. The simulated unsteady state behaviour of the flow can be seen in Fig. 6.3 showing the velocity fluctuations. In the simulations, a time step of 5×10^{-4} s was used which was believed to be sufficiently small for the unsteady behavior due to the precessing vortex core was properly resolved. For all simulations, the convective flux terms were discretized with the second order upwind high resolution scheme. For the transient term, the second-order-accurate backward differencing scheme was used. Five inner iterations were used within each time step as suggested for non-interacting flows by ANSYS CFX Modelling Guide. The solution was considered to be converged when the normalized residual was below 1×10^{-4}. Scalable wall functions were used to resolve the flow in the near wall region.

Before data was collected for time averaging, an initial period was simulated to allow a pseudo steady state to be reached, in order to exclude the initial start-up effects. This initial period can be seen in Fig. 6.4, which presents the predicted gas velocity variations in the cyclone with time. It can be seen that it took approximately 1.3 s for the flow to reach a pseudo steady state.

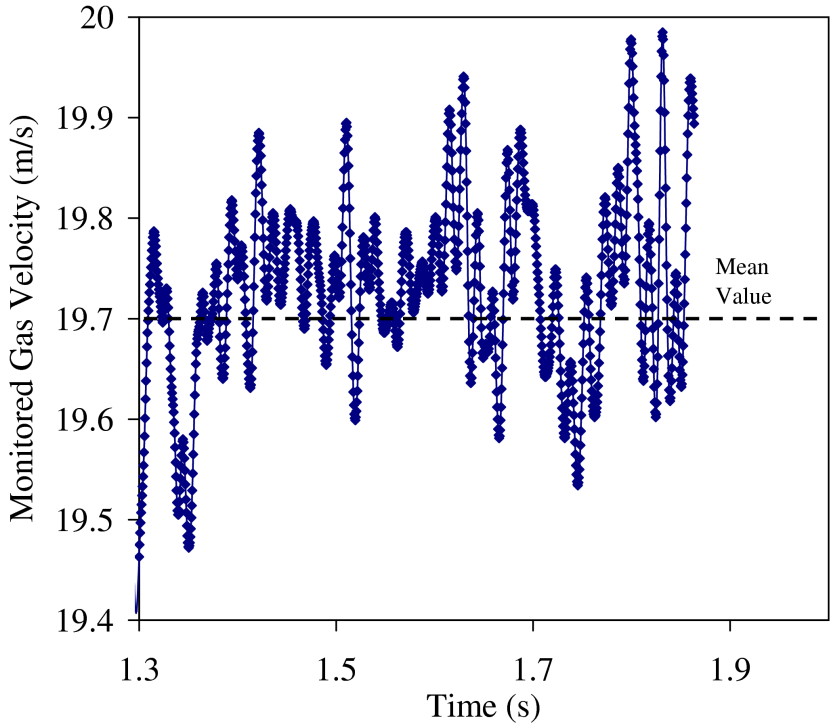

Fig. 6.3: Periodicity of the gas velocity in the cyclone predicted from SSG-RSM turbulence model.

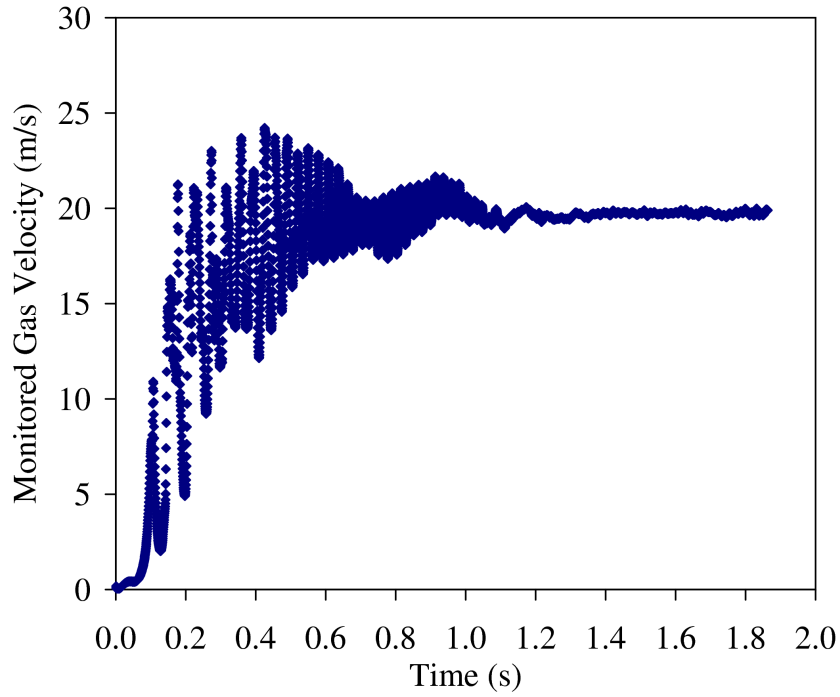

Fig. 6.4: Velocity profile in cyclone with respect to time PREDICTED from SSG-RSM turbulence model.

The simulations were performed either on a desktop PC or, when it was available, on the High Performance Computer (HPC) facility (part of the BlueFern®supercomputer project) in University of Canterbury. Eight processors (IBM POWER5+ CPUs) on the High Performance Computing (HPC) facility were used for the simulations, with the processors running at 1.9 GHz each. The computational time required for the simulations with the 2.7×10^6 mesh to reach a real time of 1.3 s for the different turbulence models are shown in Table 6.2. These computational times are based on simulations using the supercomputer facility.

Table 6.2: Computational times for different turbulence models to reach time of 1.3 s for 2.7×10^6 mesh

Turbulence Model	Computational Time (days)
k-ε	3.33
RSM	5.08

6.3.3 Results and Discussion for Simulation of the Base Case Cyclone Separator

Fig. 6.5 shows the time-averaged, normalized axial velocity (U_{ax}/U_{in}) as a function of the normalized radial position (r/R) at an axial height of x=3.25D (refer to Fig. 6.1) predicted using the SSG-RSM turbulence model. Grid independence was checked using three different meshes with the number of control volumes ranging from 0.9×10^6 to 2.7×10^6 nodes. Fig. 6.5 shows that the solutions still changed as the number of control volumes increased from 1.7×10^6 to 2.7×10^6, which implies that the solution was not completely grid independent at the higher resolution of 2.7×10^6, although it is clear that not much more refinement would be required to achieve grid independence. However, due to computer limitations, the number of control volumes could not be increased significantly above 2.7×10^6. Nevertheless, the predicted results with this mesh are in close agreement with the experimental results of Derksen (2003). Therefore, a grid with 2.7×10^6 control volumes was used in all subsequent CFD simulations of the cyclone.

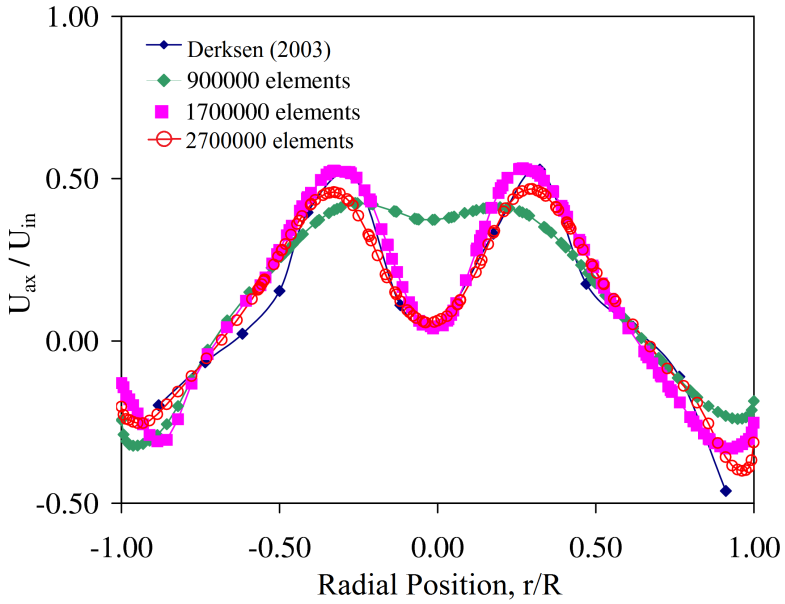

Fig. 6.5: Normalized axial velocity profile of base case cyclone predicted using SSG-RSM as the turbulence model for varying numbers of the elements in the domain.

Figs. 6.6 and 6.7 show the time-averaged, normalized tangential (U_{tan}/U_{in}) and axial velocity profiles in the radial direction at an axial height of x=3.25D predicting using different turbulence models. In Figs. 6.6 and 6.7, U_{tan} is the tangential gas velocity, with a positive sign indicating that the flow is in the same direction as the inlet fluid, U_{ax} is the axial gas velocity with a positive sign indicating an upward flow, U_{in} is the inlet gas velocity, r is the radial position, and R is the radius of the cyclone. It can be seen that the predicted tangential and axial velocity profiles using the SSG-RSM model were in close agreement with the experimental values, with an averaged percentage discrepancies of 16 and 12% respectively. However, the results using the k-ε model showed significant discrepancies from the experimental data, having percentage discrepancies of 98 to 228% respectively. The turbulence eddy viscosity was assumed to be isotropic in the k-ε model (Cortés & Gil, 2007). The results from this study have also confirmed previous findings that the assumption of isotropic viscosity in the k-ε model is not valid for strong swirling flows which are prevalent in the cyclone separator (Cortés & Gil, 2007; Jiao et al., 2007). The SSG-RSM model does not involve this simplification. Rather, each turbulence shear stress in the Reynolds-average Navier Stokes Equations is modelled with a separate transport equation to allow the anisotropy of the turbulence to be modelled more realistically.

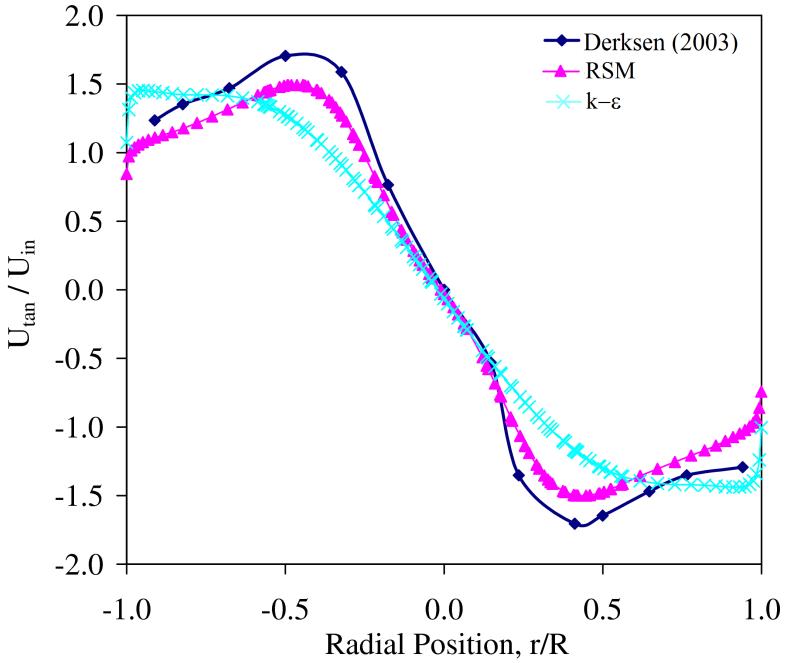

Fig. 6.6: Comparison of predicted velocities in this study from two different turbulence models with experimental results of Derksen (2003) for normalized tangential velocity profile, U_{tan}/U_{in}, in the radial direction, r/R, at an axial height of x=3.25D (refer Fig. 6.1).

Fig. 6.7 shows that the axial gas velocity profile had an M-shaped radial profile which was caused by the arrestment of the swirl by the vortex finder walls. The arrestment of the swirl resulted in the formation of a recirculation bubble in the vortex finder, which decreased the axial and tangential velocity at the axis of the cyclone (Cortés & Gil, 2007). Fig. 6.8 shows the region of the recirculation bubble, which caused a dip in the axial direction momentum.

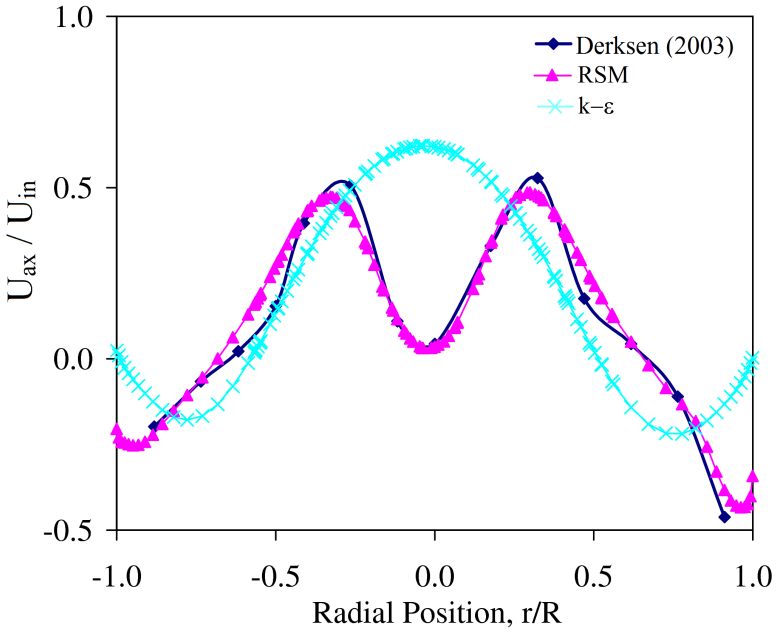

Fig. 6.7: Comparison of predicted results in this study from two different turbulence models with experimental results of Derksen (2003) for normalized axial velocity, U_{ax}/U_{in} profiles in the radial direction, r/R, at an axial height of x=3.25D (refer Fig. 6.1).

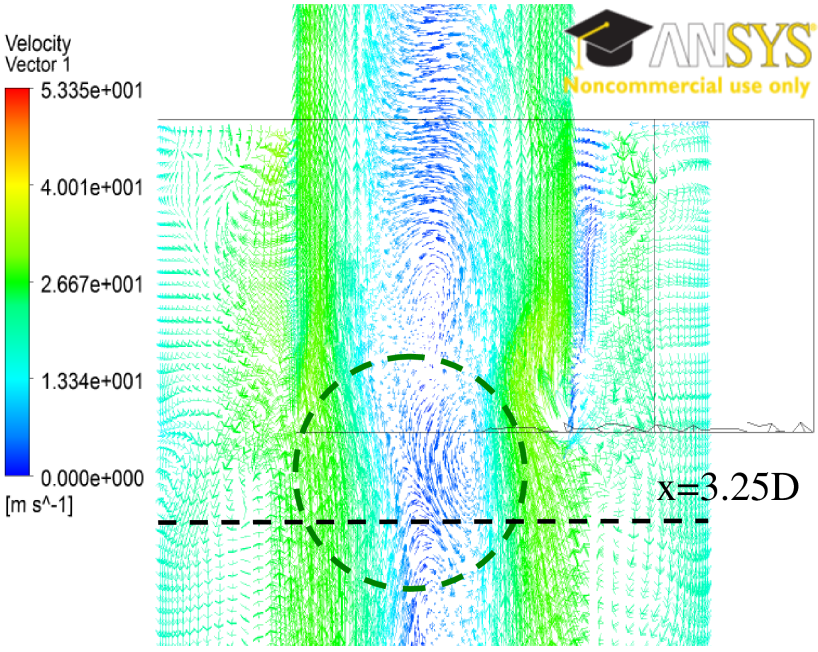

Fig. 6.8: Vector plot of velocities in the CFB cyclone separator. The circled region indicates the recirculation bubble in the vortex finder that causes the dip in the axial velocity at the center of the cyclone.

From the CFD modelling of the base case cyclone, an appropriate modelling approach for the cold model CFB cyclone was obtained which includes several important modelling decisions as listed below:

- The total number of elements for the cold model CFB cyclone mesh should be 2.7×10^{6} or more.
- An assumed uniform inlet velocity profile and an averaged atmospheric pressure at the cyclone outlet have been found to be appropriate.
- The SSG-RSM turbulence model has been chosen to model the strong swirling flows in the cyclone, due to its accuracy compared to the k-ε model.
- A time step of 5×10^{-4} s is suitable for good time resolution of the velocity fluctuations that result from the precessing vortex motion.
- Second order upwind high resolution scheme for the convective flux terms and the second-order-accurate backward differencing scheme for the transient term are required to achieve converged simulations.

6.4 CFD Simulation Set-up of the CFB Cold Model Cyclone Separator

6.4.1 Set-up of Simulations

The CFB cold model cyclone in this study was a Tengbergen-type cyclone with a scrolled and inclined inlet. This cyclone was designed to be geometrically similar to the CFB cyclone in the DFB gasifier at the University of Canterbury. Fig. 6.9 shows the geometry of the cold model cyclone separator where the scroll or barrel diameter D_{ba} is 0.192 m, the cyclone diameter D_{cy} is 0.152 m, the diameter of the vortex finder D_{vf} is equal to the diameter of the exit Dex of 0.08 m. Table 6.3 shows the dimensional relationships for the cyclone.

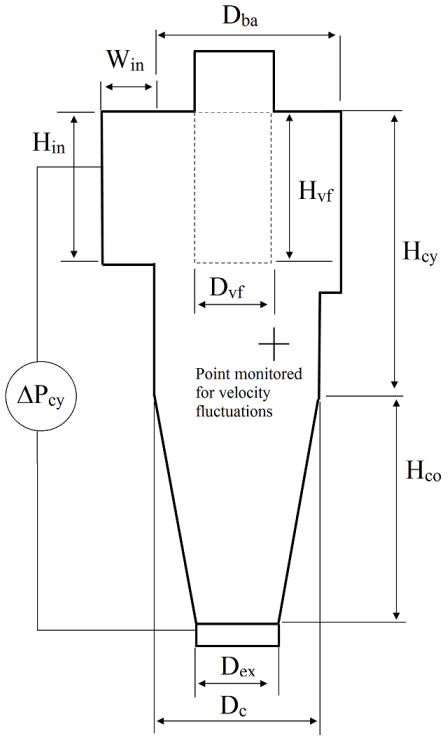

Fig. 6.9: Configuration and dimensions of the CFB cold model cyclone separator

Table 6.3: Dimensional ratios of a CFB Cyclone for gasification and cold model plant

Dimensional Ratios	Values
$\frac{H_{in}}{D_{vf}}$	1.60
$\frac{W_{in}}{D_{vf}}$	0.50
$\frac{D_c}{D_{vf}}$	1.88
$\frac{H_{vf}}{D_{vf}}$	2.00
$\frac{D_{ex}}{D_{vf}}$	1.00
$\frac{H_{cy}}{D_{vf}}$	2.89
$\frac{H_{co}}{D_{vf}}$	2.50

Fig. 6.10 shows the front and back views of the CFB cold model cyclone separator geometry used for simulation in CFX software. The extended elbow outlet and the standpipe were also included in the geometry for the simulations. The inlet was inclined at 20° from the horizontal. The bottom of the standpipe was blocked using a blinding

flange during experimental measurements of the pressure drop. Therefore, the bottom of the standpipe in the geometry was set as a wall in the CFD simulations. The gas flowed through the vortex finder in the CFB cold model cyclone and through the elbow that was extended by 0.8 m downstream of the cyclone before exiting through an outlet boundary. The extended outlet was included in the simulations, although it was not present in the experimental cold model, to allow the exit velocity profile to be fully developed, in order to avoid numerical issues that can arise when recirculation zones are present near the exit.

Fig. 6.10: Front and back views of the CFB cold model cyclone separator

A grid independence check was also performed by comparing the velocity profiles simulated using grids with 2.2×10^6 and 3.2×10^6 control volumes. Fig. 6.11 shows the mesh with 3.2×10^6 control volumes. The length of each control volume varies within the location of the cyclone and averages to a value of 1.0mm.

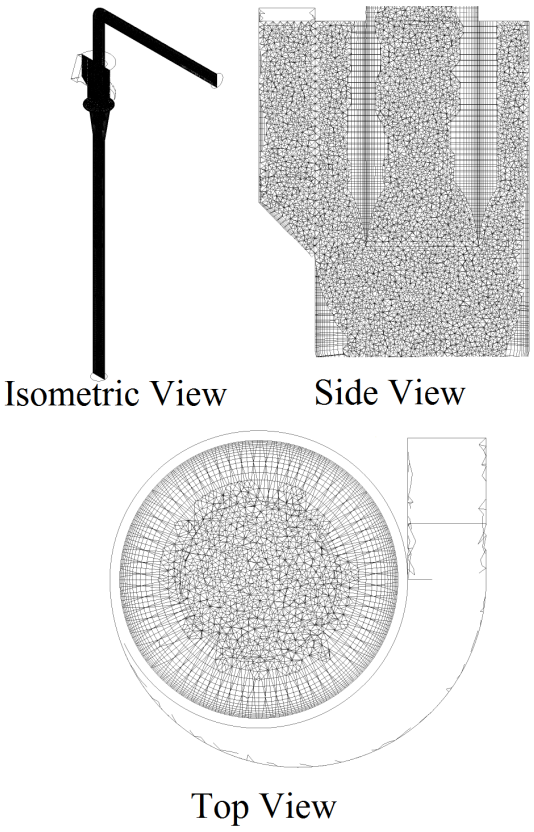

Fig. 6.11: Top and side views of the mesh from the CFB cold model cyclone

After validation, the modelling approach used on the base case cyclone was applied to the CFB cold model cyclone. Fig. 6.12 shows variations in the simulated gas velocity with time at the monitored location as illustrated in Fig. 6.9 from 0.70 s to 1.48 s after the start of the transient simulations. Similar to the simulations for the base case cyclone, the PVC phenomenon caused fluctuation of the gas velocity profile in the cold model cyclone. The data (the axial and tangential velocity profiles, and the pressure drop) were time-averaged after a time of 0.70 s to exclude the start-up effects.

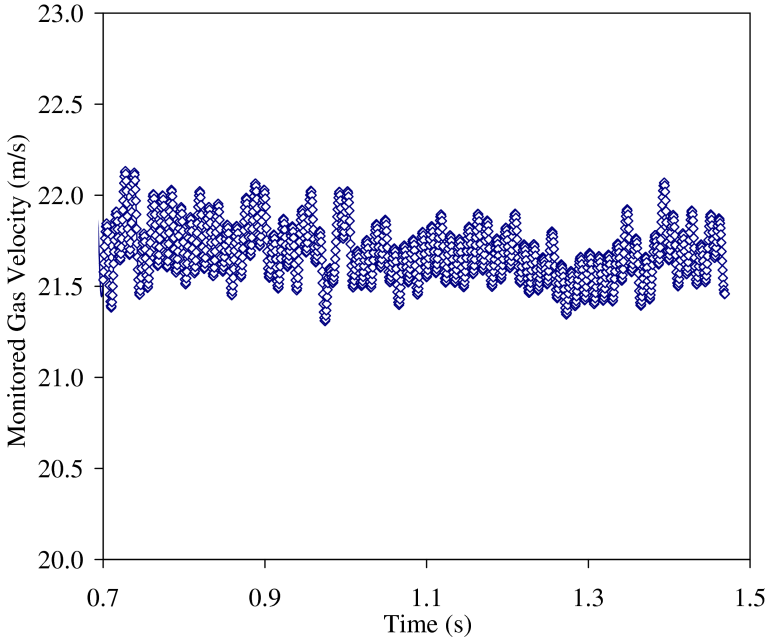

Fig. 6.12: Simulated gas velocity as a function of elapsed time at monitored location in the cold model cyclone using SSG-RSM turbulence model.

The pressure drop across the CFB cyclone, ΔP_{cy}, was predicted for various cyclone inlet velocities, and the results are compared to the experimental results measured at the locations illustrated in Fig. 6.5.

To investigate the cause of the eroded region of the cyclone in the DFB gasifier (Fig. 1.2), spherical copper particles of 83 μm were tracked in the CFD simulations to observe the region of particle impingement on the cyclone. The spherical 83 μm copper particles were equivalent in size to the irregular copper particles used in the cold model, which had a mean particle diameter of 138 μm and a particle circularity of 0.60 ($d_{eff} = \phi d_p$). One-way Lagrangian approach was used to reduce computational time, since the mass loading of particles (0.015 kg_{copper}/kg_{air}) was so low that it would not affect the velocity fields significantly. Particle to wall interaction was modelled by setting the restitution coefficient to a value of 0.90 (Wan et al., 2008).

6.4.2 Results and Discussion: Grid Independence, Velocity Profiles, Pressure Drop, Particle Tracks

Fig. 6.13 shows the time-averaged, normalized axial gas velocity profile (U_{ax}/U_{in}) at a height of 0.18 m from the top of the cyclone. The axial gas velocity profile shows an M-shaped profile, similar to that of the base case cyclone. As mentioned earlier, the dip of the axial velocity at the axis of the cyclone was due to a recirculation bubble in the vortex finder (Cortés & Gil, 2007).

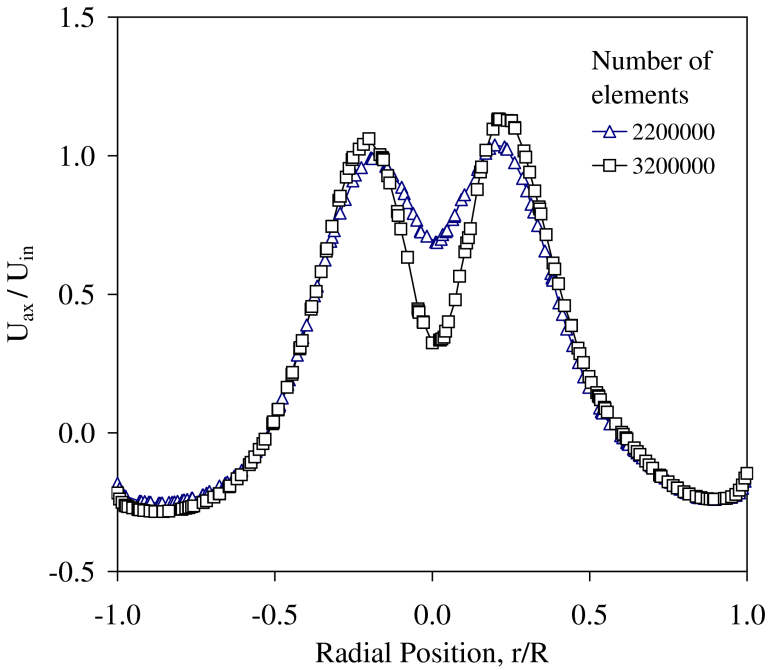

Fig. 6.13: Axial gas velocity profile in the CFB cyclone separator at an axial height of 0.18 m below the top of the cyclone.

Fig. 6.13 also shows the mesh sensitivity for the simulation. It can be seen that the two axial velocity profiles for the two different meshes (with 2.2×10^6 and 3.2×10^6 control volumes, respectively) were nearly similar, except for the axial velocity near the centre line where the predicted axial velocity from the finer mesh (3.2×10^6 elements) was lower than that predicted using the coarser mesh (2.2×10^6 elements). This suggests that the solution was not quite grid independent. However, in this study, the number of elements was limited by the computational memory, and a mesh with more than 3.2×10^6 control volumes could not be generated. Therefore, the simulation results from the finer mesh were used for subsequent simulations.

In this study, experimental velocity profiles were not measured. Therefore, direct validation of the model via comparison of experimental and simulated velocity profiles was not possible. Instead, the CFD model was validated by comparing the modelled pressure drop with experimental values obtained from the cold model cyclone (Fig. 6.14). From Fig. 6.14 a close agreement has been observed between the simulated and measured pressure drop values, with a correlation coefficient R^2 value of 0.7755. The close agreement between the experimental and simulated velocity fields of the Derksen cyclone, together with the agreement between the experiment and simulated pressure drops over the cold model cyclone suggest that the modelling approach applied here is appropriate for use as a design tool for cyclones.

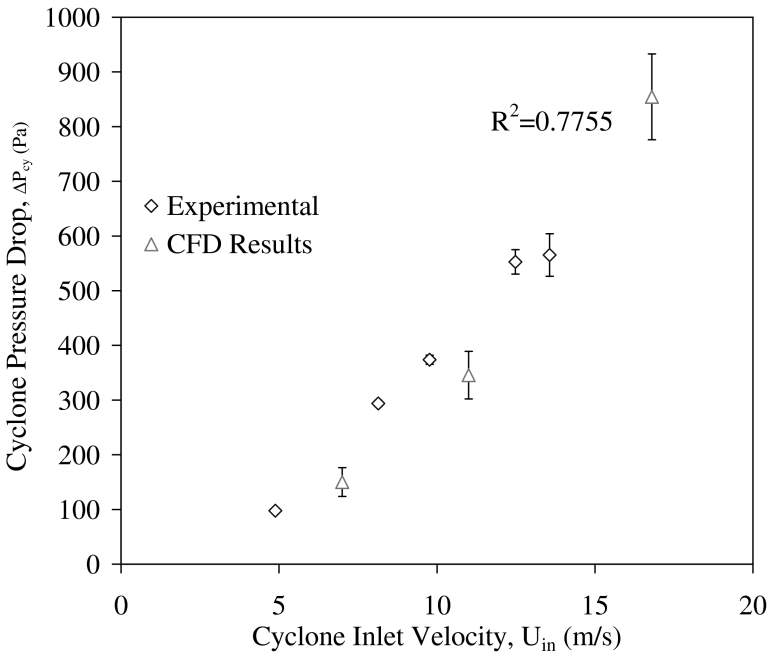

Fig. 6.14: Simulated and measured CFB cyclone pressure drop as a function of inlet velocity, U_{in}.

Fig. 6.15 shows a plan view of the cyclone with the particle tracks of 83 μm copper particles. The circled region A shows where the particles first impinge on the cyclone wall and where the momentum change by the wall is the highest in the cyclone. If the momentum of the particles is sufficiently high in this region, the particles could eventually cause erosion of the cyclone wall at this location. This is believed to be the cause of erosion in this region of the CAPE CFB cyclone, as was shown in Fig. 1.2.

After bouncing off the wall in region A, the particles scatter in various directions, depending on the impact location and angle on the wall. The subsequent secondary impact region is spread out over a wider area on the cyclone wall, identified as region B in Fig. 6.15. The copper particle velocities are also slightly lower due to a loss of momentum upon inelastic collision on the wall in region A. The wider area of the secondary impact region and the lower particle velocity leads to a lower likelihood of erosion in region B. Region A is prone to erosion because the particles collisions are more concentrated over a smaller area.

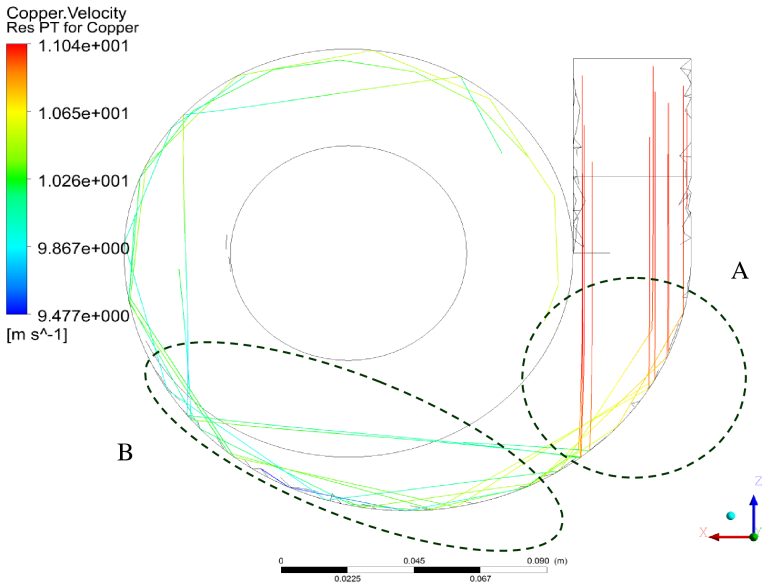

Fig. 6.15: Illustration of locations in the CFB cold model cyclone where particles impact on the cyclone wall.

6.5 Conclusions

This chapter presents a CFD modelling approach for cyclones that can be used as a design tool for optimisation of cyclone separators in industry. The CFD model was first used to simulate a base case cyclone which was validated using experimental velocity data found in the literature. From this base case simulation, it is found that the modelling approach requires the use of the SSG-RSM turbulence model with a mesh of 2.7×10^6 elements or higher and a time step of 5×10^4 s in order to achieve satisfactory accuracy. After this, the above modelling approach was applied to simulations of the flows in the CFB cold model cyclone, and a close match between the predicted and experimentally

measured pressure drop over the cyclone was achieved. Results from Lagrangian particle tracking suggest that concentrated particles collisions of high momentum over a small wall area is the likely cause for observed erosion at the inlet of the DFB biomass gasifier CFB cyclone as reported by McKinnon (2009). Erosion is less likely at other areas of the cyclone wall, due to a continuous loss of momentum after previous inelastic collisions, and because subsequent impact regions are larger in area and therefore collisions are less concentrated.

Chapter 7

Conclusions and Future Work

7.1 Overall Summary

Due to the increasing utilization of fluidized bed gasification technology to convert biomass to energy, there is renewed interest in investigating the hydrodynamics of the fluidized bed. Good understanding and prediction of the hydrodynamics in fluidized bed gasification technologies would facilitate the successful design and optimization of the fluidized beds.

This project is concerned with the hydrodynamics of a cold model of a dual fluidized bed gasification plant, which is a scaled-down model of the Güssing biomass gasification plant in Austria (Löffler et al., 2003; Kaiser et al., 2003). The project was divided into two phases: Phase I and Phase II. In Phase I, a cold model of circulating fluidized bed (CFB) was designed, constructed and tested to experimentally investigate and model the hydrodynamics of the CFB riser. Phase II of the project focused on the hydrodynamics of the dual fluidized bed (DFB), which incorporated both a CFB and a bubbling fluidized bed (BFB). Both a singular bed material representing sand in an industrial gasifier and a bed consisting of a binary mixture of materials representing sand and char in an industrial gasifier were tested in the DFB. CFD modeling of the CFB cyclone separator was also performed to develop a design tool for modelling the fluid flows in the cyclone. A preliminary investigation was performed on the impingement of particles on the internal surfaces of a cyclone and the effect this might have on erosion of the cyclone wall.

From this study, operational maps for both the CFB and DFB systems were established. In developing these operational maps, the primary airflow rate, secondary airflow rate (both for the CFB), and the BFB airflow rate (for the DFB) were varied to determine the operational boundaries for steady state operation of the plant. It was found that the steady state operation of the DFB is determined by the chute pressure drop. A high chute pressure drop implies a high mass loading of particulates in the chute, which is desirable for providing a proper gas seal between the CFB riser and the BFB.

In an actual biomass gasifier, the solid particles transfer heat to the biomass for gasification reactions while circulating around the plant, and therefore the solids mass flow rate directly affects the reaction or gasification rate of the process. In this work, a new correlation was proposed to determine the solids mass flow rate from the CFB riser, which is related to the CFB riser exit width and a newly introduced aerodynamic factor. The aerodynamic factor was introduced in this work to empirically take into account the effect of particle inertia and particle clustering effects on the solids mass flow exiting the CFB riser.

Numerous empirical correlations can be found in literature for modelling the hydrodynamics in the CFB riser. However, it is uncertain whether these correlations are applicable to fluidized bed configurations and operating conditions outside those they were developed for. Therefore, a critical assessment was performed to determine their accuracy by comparing their predictions with measurements from the CFB riser experiments. It was found that the correlations in the literature are, in general, unable to adequately describe the hydrodynamics of the CFB riser for various reasons. First of all, there are differences between the experimental conditions over which the correlations in literature were developed, and the experimental conditions of the current work. This highlights the lack of generality of the empirical correlations. Secondly, the air jets from the secondary airflow cause an extended solids acceleration region, resulting in a higher solids velocity. Solids acceleration is not accounted for in the correlations tested. Finally, particle clustering effects are also not accounted for when predicting the solids velocity. Clustering effects reduce the effective drag force on the particles. The latter two factors can be used to explain why the solids velocity was not accurately predicted. It is clear that the existing model for solids velocity prediction (based on a single particle force

balance) is appropriate only for dilute conditions where inter-particle collisions can be neglected. In predicting the pressure drop using the existing model, the pressure drop due to solids acceleration was neglected, resulting in a lower predicted riser bottom and upper section pressure drops. Future models should include the effect of the solids acceleration. However, experimental measurements of the solids velocity, using for example Laser Doppler Anemometry are required in order to validate such predictions.

From the tests on the dual fluidized bed with a singular type of bed material (copper particles, which represent sand in an industrial gasifier), it was found that chute bypass can be prevented by ensuring that the chute pressure drop is sufficiently high. This can be achieved by increasing the BFB or chute airflow rate so that the chute becomes adequately filled with fluidized solids. The chute pressure drop can be increased by ensuring that the BFB or chute airflow rate is sufficiently high. The results from experiments with a mixture of binary solids showed that the addition of large, low density particles (1750 μm MDPE pellets, which represent char under high temperature condition in an industrial gasifier) into the system causes an obstruction of the mass flow of copper particles through the inclined chute. Consequently the riser bottom and upper section pressure drops, and the solids core flow rate were decreased. Thus, it is expected that chars in an actual biomass gasifier can induce a similar effect on the pressure drop and mass flow rates to that observed in the cold model. This suggests that there is a limit to the size of biomass particles that can be added to into the BFB in order to avoid chute obstruction.

The CFD model of the cold model cyclone was validated by comparing the predicted and measured pressure drops. The CFD model can now be used for further optimization efforts of the cyclone, with focus on reducing the wall erosion rates caused by the impact of particles. Preliminary studies showed a region of highly concentrated particle impingement on the cold model cyclone. This is believed to be the cause for the erosion of the cyclone wall of the CAPE gasifier CFB cyclone.

7.2 Future Work

To verify that the results from the cold model simulate the hydrodynamics of the practical biomass gasification plant, validation of the cold model results is recommended using first hand data from the Güssing biomass gasification plant. This would also allow validation of the scaling laws that were used in designing the cold model.

The way to validate the scaling laws is to measure the solids circulation rate isokineticaly in the actual gasification plant using a suction probe at various heights. These solids flow rates would then be used to determine the dimensionless numbers that characterize the system, which can be compared to those of the cold model. Measuring the solids mass flow rate in the gasification plant under high temperature conditions requires a cooling system incorporated into the suction probe, such as a cooling water jacket. Such a probe has been developed before to sample fly ash in boilers using suction pyrometers (Hansen et al., 1998), and would be useful in future experiments to determine the solids mass flow rate under high temperature conditions.

Besides that, the pressure fluctuations can also be used for comparison between the hydrodynamics of the cold model and those of the gasification plant (Sanderson & Rhodes, 2005; Gallucci & Gibilaro, 2005). This would also provide another means to validate the scaling laws, but this would require the sampling frequency of the both the cold model and the gasification plant to be sufficiently high to capture the pressure fluctuations.

As mentioned in Chapter 4, the effect of the secondary air jets and the formation of particle clusters invalidate the solids velocity model used, which is based on a force balance over a single particle. Further work should then be directed towards experimental measurements of the cluster properties in the CFB riser. This would provide information on the cluster diameter, the solid fraction within the cluster, the cluster velocity, and the cluster based drag coefficient (Noymer & Glicksman, 1999; Helland et al., 2007). The cluster-based solids velocity in the riser can then be predicted more accurately using existing published theories and correlations of cluster dynamics. The experimental measurements would also contribute to the body of knowledge regarding cluster hydrodynamics, which is of interest to many researchers investigating fluidized beds (Tsukada et al., 1997; Sharma et al., 2000; Zou et al., 2008; Helland et al.,

2007).

The experimental work on clusters should also be extended to the downward cluster flows at the annular wall. This is because CFB boilers usually comprise of water tubes at the wall, and therefore the heat transfer to the water tubes is governed by the solids flow dynamics in the annular wall flow (Ebert et al., 1993; Noymer & Glicksman, 1999). Specifically, the heat transfer from the downward cluster flows to the wall is dependent on the contact time of clusters with the wall, the concentration of solids in the clusters, and the fraction of the wall covered by the clusters (Noymer & Glicksman, 1999). The investigation of these cluster properties provides valuable information in predicting the solids to wall heat transfer rates for scale-up or design purposes of a CFB boiler. Similar work has been performed before, with each study focusing on different aspects of the clusters (Noymer & Glicksman, 1999; Guenther & Breault, 2007).

The riser upper section pressure drop was under-predicted in Chapter 4, due to the assumption that the pressure drop component due to solids acceleration was negligible, which was based on findings from Nieuwland et al. (1997) (refer to Chapter 2). Further work could be expanded in this area to investigate the models that account for the solids acceleration pressure drop in the transport zone (Bai & Kato, 1995; Guan et al., 2010).

The results from the binary mixture experiments showed a decreased in solids mass flow rate when larger, less dense particles were added to the system. However, the BFB pressure drop did not show a clear indication of the blocking effect caused by the larger MDPE pellets. Measurements of the solid mass flow rate from the loop seal into the BFB could be performed to investigate the effect of the MDPE pellets on the BFB pressure drop.

Future work on the CFD model of the cyclone can be extended to model higher solid mass loadings by using the two-way coupled Lagrangian model to account for the effect of particle drag on the airflow patterns. Issues such as numerical instabilities associated with the two-way coupled model could be addressed as well. For even higher mass loadings, the Eulerian-Eulerian model could be used to take into account particle-particle interactions, and the model could be validated by comparing the predicted cyclone pressure drop (with solids laden gas flows in the cyclone) with experimental measurements.

Bibliography

Adánez, J., Gayán, P., García-Labiano, F., & de Diego, L. F. (1994). Axial voidage profiles in fast fluidized beds. *Powder Technology*, *81*(3), 259–268.

Allen, T. (1968). *Particle Size Measurement*. Germany: Chapman and Hall Ltd.

Almendros-Ibáñez, J. A., Sánchez-Delgado, S., Sobrino, C., & Santana, D. (2009). Experimental observations on the different mechanisms for solid ejection in gas-fluidized beds. *Chemical Engineering and Processing: Process Intensification*, *48*(3), 734–744.

Apergis, N., & Payne, J. E. (2010). Renewable energy consumption and economic growth: Evidence from a panel of oecd countries. *Energy Policy*, *38*(1), 656–660.

Azadi, M., Azadi, M., & Mohebbi, A. (2010). A CFD study of the effect of cyclone size on its performance parameters. *Journal of Hazardous Materials*, *182*(1-3), 835–841.

Babu, S. P., Shah, B., & Talwalkar, A. (1978). Fluidization correlations for coal gasification materials - minimum fluidization velocity and fluidized bed expansion ratio. *AIChE Symp Ser*, *74*(176), 176–186.

Bai, D., & Kato, K. (1995). Saturation carrying capacity of gas and flow regimes in CFB. *Journal of Chemical Engineering of Japan*, *28*(2), 179–185.

Barry, D., Chan, C., & Williams, G. (2009). Morphological quantification of filamentous fungal development using membrane immobilization and automatic image analysis. *Journal of Industrial Microbiology & Biotechnology*, *36*(6), 787–800.

Benyahia, S., Syamlal, M., & O'Brien, T. J. (2005). Evaluation of boundary conditions used to model dilute, turbulent gas/solids flows in a pipe. *Powder Technology*, *156*(2-3), 62–72.

Berruti, F., Pugsley, T. S., Godfroy, L., Chaouki, J., & Patience, G. S. (1995). Hydrodynamics of circulating fluidized bed risers: A review. *The Canadian Journal of Chemical Engineering*, *73*(5), 579–602.

Bi, H. T., Ellis, N., Abba, I. A., & Grace, J. R. (2000). A state-of-the-art review of gas-solid turbulent fluidization. *Chemical Engineering Science*, *55*(21), 4789–4825.

Biagini, E., Simone, M., & Tognotti, L. (2009). Characterization of high heating rate chars of biomass fuels. *Proceedings of the Combustion Institute*, *32*(2), 2043–2050.

Blazek, J. (2005). *Computational fluid dynamics: principles and applications*. Elsevier.

Brandani, S., & Zhang, K. (2006). A new model for the prediction of the behaviour of fluidized beds. *Powder Technology*, *163*(1-2), 80–87.

Bricout, V., & Louge, M. Y. (2004). A verification of glicksman's reduced scaling under conditions analogous to pressurized circulating fluidization. *Chemical Engineering Science*, *59*, 2633–2638.

Bull, D. (2008). Performance improvements to a fast internally circulating fluidized bed (FICFB) biomass gasifier for combined heat and power plants.

Charitos, A., Hawthorne, C., Bidwe, A. R., Korovesis, L., Schuster, A., & Scheffknecht, G. (2010). Hydrodynamic analysis of a 10kwth calcium looping dual fluidized bed for post-combustion CO_2 capture. *Powder Technology*, *200*(3), 117–127.

Chen, L. H., & Wen, C. Y. (1982). Model of solid gas reaction phenomena in the fluidized bed freeboard. *AIChE Journal*, *28*(6), 1019–1027.

Chen, Y.-g., Tian, Z.-p., & Miao, Z.-q. (2006). Analysis of the pressure fluctuations in binary solids circulating fluidized bed. *Energy Conversion and Management*, *47*(5), 611–623.

Cheng, L., & Basu, P. (1999). Effect of pressure on loop seal operation for a pressurized circulating fluidized bed. *Powder Technology*, *103*(3), 203–211.

Chung, T. (2002). *Computational Fluid Dynamics*. Cambdrige University Press.

Colakyan, M., & Levenspiel, O. (1984). Elutriation from fluidized beds. *Powder Technology*, *38*(3), 223–232.

Cortés, C., & Gil, A. (2007). Modeling the gas and particle flow inside cyclone separators. *Progress in Energy and Combustion Science*, *33*(5), 409–452.

Cui, J., Chen, X., Gong, X., & Yu, G. (2010). Numerical study of gas-solid flow in a radial-inlet structure cyclone separator. *Industrial & Engineering Chemistry Research*, *49*(11), 5450–5460.

Davidson, J. F. (2000). Circulating fluidised bed hydrodynamics. *Powder Technology*, *113*(3), 249–260.

Derksen, J. J. (2003). Separation performance predictions of a stairmand high-efficiency cyclone. *AIChE Journal*, *49*(6), 1359–1371.

Derksen, J. J., Van Den Akker, H. E. A., & Sundaresan, S. (2008). Two-way coupled large-eddy simulations of the gas-solid flow in cyclone separators. *AIChE Journal*, *54*(4), 872–885.

Ebert, T. A., Glicksman, L. R., & Lints, M. (1993). Determination of particle and gas convective heat transfer components in a circulating fluidized bed. *Chemical Engineering Science*, *48*(12), 2179–2188.

Ersoy, L., Golriz, M., Koksal, M., & Hamdullahpur, F. (2004). Circulating fluidized bed hydrodynamics with air staging: An experimental study. *Powder Technology*, *145*, 25–33.

European Climate Foundation, Sveaskog, Södra, and Vattenfall (2010). Biomass for heat and power: Opportunity and economics.
URL http://www.europeanclimate.org/documents/Biomass_report_-_Final.pdf

European Commission (2008). Energy policy factsheet: Denmark.
URL http://www.energy.eu/renewables/factsheets/2008_res_sheet_denmark_en.pdf

European Renewable Energy Council (2009). Renewable energy policy review: Denmark.

Farrell, P. A. (1996). *Hydrodynamic scaling and solids mixing in pressurized bubbling fluidized bed combustors*. Ph.D. thesis, Massachusetts Institute of Technology.

Foscolo, P. U., Germana, A., Jand, N., & Rapagna, S. (2007). Design and cold model testing of a biomass gasifier consisting of two interconnected fluidized beds. *Powder Technology*, *173*, 179–188.

Fu, X., Dutt, M., Bentham, A. C., Hancock, B. C., Cameron, R. E., & Elliott, J. A. (2006). Investigation of particle packing in model pharmaceutical powders using x-ray microtomography and discrete element method. *Powder Technology*, *167*(3), 134–140.

Gallucci, K., & Gibilaro, L. G. (2005). Dimensional cold-modeling criteria for fluidization quality. *Ind. Eng. Chem. Res.*, *44*(14), 5152–5158.

Geldart, D., Cullinan, J., Georghiades, S., Gilvray, D., & Pope, D. J. (1979). The effect of fines on entrainment from gas fluidised beds. *Transactions of the Institution Chemical Engineering*, *57*, 269–275.

Geldart, D., & Jones, P. (1991). The behaviour of l-valves with granular powders. *Powder Technology*, *67*(2), 163–174.

Gibilaro, L. (2001). *Fludization-dynamics*. Butterwirth-Heinemann.

Glicksman, L. R., Hyre, M., & Woloshun, K. (1993). Simplified scaling relationships for fluidized beds. *Powder Technology*, *77*(2), 177–199.

Gnanapragasam, N. V., & Reddy, B. V. (2009). Numerical modeling of axial bed-to-wall heat transfer in a circulating fluidized bed combustor. *International Journal of Heat and Mass Transfer*, *52*(7-8), 1657–1666.

Gömez-Barea, A., & Leckner, B. (2010). Modeling of biomass gasification in fluidized bed. *Progress in Energy and Combustion Science*, *36*(4), 444–509.

Goo, J. H., Seo, M. W., Park, D. K., Kim, S. D., Lee, S. H., Lee, J. G., & Song, B. H. (2008). Hydrodynamic properties in a cold-model dual fluidized-bed gasifier. *Journal of Chemical Engineering of Japan*, *41*(7), 686–690.

Grace, J. R., Avidan, A. A., & Knowlton, T. M. (1997). *Circulating Fluidized Beds*. Blackie Academic and Professional.

Grieco, E., & Marmo, L. (2006). Predicting the pressure drop across the solids flow rate control device of a circulating fluidized bed. *Powder Technology*, *161*(2), 89–97.

Guan, G., Fushimi, C., & Tsutsumi, A. (2010). Prediction of flow behavior of the riser in a novel high solids flux circulating fluidized bed for steam gasification of coal or biomass. *Chemical Engineering Journal*, *164*(1), 221–229.

Guenther, C., & Breault, R. (2007). Wavelet analysis to characterize cluster dynamics in a circulating fluidized bed. *Powder Technology*, *173*(3), 163–173.

Gungor, A., & Eskin, N. (2007). Hydrodynamic modeling of a circulating fluidized bed. *Powder Technology*, *172*, 1–13. Retrieved July 8, 2008, from ScienceDirect database.

Hahn, Y.-B., Nam, I.-S., Park, D.-G., & Lee, I. I. O. (1995). Hydrodynamic behavior of iron ore particles in a circulating fluidized bed reduction system. *Metals and Materials International*, *1*(2), 99–105.

Hansen, P. F. B., Andersen, K. H., Wieck-Hansen, K., Overgaard, P., Rasmussen, I., Frandsen, F. J., Hansen, L. A., & Dam-Johansen, K. (1998). Co-firing straw and coal in a 150-MW_e utility boiler: in situ measurements. *Fuel Processing Technology*, *54*(1-3), 207–225.

Harris, A. T., Davidson, J. F., & Thorpe, R. B. (2003). The influence of the riser exit on the particle residence time distribution in a circulating fluidised bed riser. *Chemical Engineering Science*, *58*(16), 3669–3680.

Harris, B., & Davidson, J. (1994). *Modelling Options for Circulating Fluidized Beds: A Core/annulus Depositions Model*, vol. IV of *Circulating Fluidized Bed Technology*. New York: AIChE Publications.

Helland, E., Bournot, H., Occelli, R., & Tadrist, L. (2007). Drag reduction and cluster formation in a circulating fluidised bed. *Chemical Engineering Science*, *62*(1-2), 148–158.

Hoekstra, A. J., Derksen, J. J., & Van Den Akker, H. E. A. (1999). An experimental and numerical study of turbulent swirling flow in gas cyclones. *Chemical Engineering Science*, *54*(13-14), 2055–2065.

Huang, W. X., Zhu, J. X., & Pärssinen, J. H. (2006). Comprehensive study on the solids acceleration length in a long CFB riser. *Chemical Engineering & Technology*, *29*(10), 1197–1204.

Jang, H. T., Park, T. S., & Cha, W. S. (2010). Mixing-segregation phenomena of binary system in a fluidized bed. *Journal of Industrial and Engineering Chemistry*, *16*(3), 390–394.

Jiao, J., Liu, Z., & Zheng, Y. (2007). Evaluations and modifications on reynolds stress model in cyclone simulations. *Chemical Engineering & Technology*, *30*(1), 15–20.

Johansson, A., Johnsson, F., & Leckner, B. (2007). Solids back-mixing in cfb boilers. *Chemical Engineering Science*, *62*(1-2), 561–573.

Johnsson, F., Andersson, S., & Leckner, B. (1991). Expansion of a freely bubbling fluidized bed. *Powder Technology*, *68*(2), 117–123.

Kaiser, S., Löffler, G., Bosch, K., & Hofbauer, H. (2003). Novel scaling parameter for circulating fluidized beds. *Chemical Engineering Science*, *58*, 4215–4223.

Karagoz, I., & Kaya, F. (2007). CFD investigation of the flow and heat transfer characteristics in a tangential inlet cyclone. *International Communications in Heat and Mass Transfer*, *34*(9-10), 1119–1126.

Kehlenbeck, R., Yates, J., di Felice, R., Hofbauer, H., & Rauch, R. (2001). Novel scaling parameter for circulating fluidized beds. *AIChE Journal*, *47*, 582–589.

Khan, A. A., de Jong, W., Jansens, P. J., & Spliethoff, H. (2009). Biomass combustion in fluidized bed boilers: Potential problems and remedies. *Fuel Processing Technology*, *90*(1), 21–50.

Kim, S., Namkung, W., & Kim, S. (1999). Solids flow characteristics in loop-seal of a circulating fluidized bed. *Korean Journal of Chemical Engineering*, *16*(1), 82–88.

Kim, S. W., Kim, S. D., & Lee, D. H. (2002). Pressure balance model for circulating fluidized beds with a loop-seal. *Industrial & Engineering Chemistry Research*, *41*(20), 4949–4956.

Knowlton, T. M., Karri, S. B. R., & Issangya, A. (2005). Scale-up of fluidized-bed hydrodynamics. *Powder Technology*, *150*(2), 72–77.

Kolar, A. K., & Leckner, B. (2006). Scaling of CFB boiler hydrodynamics. *Advances in Energy Research*.

Kreuzeder, A., Pfeifer, C., & Hofbauer, H. (2007). Fluid dynamic investigations in a scaled cold model for a dual fluidized bed biomass steam gasification process: Solid flux measurements and optimization of the cyclone. *International Journal of Chemical Reactor Engineering*, *5*.

Kunii, D., & Levenspiel, O. (1991). *Fluidization Engineering*. Soneham: Butterworth-Heinemann, second edition ed.

Kunii, D., & Levenspiel, O. (1995). Effect of exit geometry on the vertical distribution of solids in circulating fluidized beds. part I: solution of fundamental equations; part II: analysis of reported data and prediction. *Powder Technology*, *84*(1), 83–90.

Lackermeier, U., Rudnick, C., Werther, J., Bredebusch, A., & Burkhardt, H. (2001). Visualization of flow structures inside a circulating fluidized bed by means of laser sheet and image processing. *Powder Technology*, *114*(1-3), 71–83. 0032-5910 doi: DOI: 10.1016/S0032-5910(00)00265-5.

Lewis, W. K., E.R., G., & W.C., B. (1949). Characteristics of fluidized particles. *Industrial and Engineering Chemistry*, *41*(6), 1104–1117.

Löffler, G., Kaiser, S., Bosch, K., & Hofbauer, H. (2003). Hydrodynamics of a dual fluidized-bed gasifier–part I: simulation of a riser with gas injection and diffuser. *Chemical Engineering Science*, *58*(18), 4197–4213.

Luo, K. (1987). Dilute, dense phase and maximum solid-gas transport. *Doctoral Dissertation, Illinois Institute of Technology*.

Lv, P. M., Xiong, Z. H., Chang, J., Wu, C. Z., Chen, Y., & Zhu, J. X. (2004). An experimental study on biomass air-steam gasification in a fluidized bed. *Bioresource Technology*, *95*(1), 95–101.

Mabrouk, R., Chaouki, J., & Guy, C. (2008). Exit effect on hydrodynamics of the internal circulating fluidized bed riser. *Powder Technology*, *182*(3), 406–414.

Makkawi, Y. T., & Wright, P. C. (2002). Fluidization regimes in a conventional fluidized bed characterized by means of electrical capacitance tomography. *Chemical Engineering Science*, *57*(13), 2411–2437.

McKinnon, H. (2009). Improved hydrogen production from biomass gasification in a dual fluidized bed reactor.

Microtrac (2000). *Microtrac Software for Windows Operating System: Operations Manual*.

Monazam, E. R., & Shadle, L. J. (2008). Analysis of the acceleration region in a circulating fluidized bed riser operating above fast fluidization velocities. *Industrial & Engineering Chemistry Research*, *47*(21), 8423–8429.

Monazam, E. R., Shadle, L. J., & Mei, J. S. (2007). Impact of the circulating fluidized bed riser on the performance of a loop seal nonmechanical valve. *Industrial & Engineering Chemistry Research*, *46*(6), 1843–1850.

Monazam, E. R., Shadle, L. J., Mei, J. S., & Spenik, J. (2005). Identification and characteristics of different flow regimes in a circulating fluidized bed. *Powder Technology*, *155*(1), 17–25.

Nakamura, K., & Capes, C. E. (1973). Vertical pneumatic conveying: A theoretical study of uniform and annular particle flow models. *Canadian Journal of Chemical Engineering*, *51*(1).

Namkung, W., & Done Kim, S. (1998). Gas backmixing in a circulating fluidized bed. *Powder Technology*, *99*(1), 70–78.

New Zealand Ministry of Economic Development (2010). New zealand's energy outlook 2009/2010: Changing gear.
URL http://www.bioenergy.org.nz/documents/Homepage/Coloured_boxes/eEnergy-Outlook_Changing-Gear-Scenario.pdf

Nieuwland, J. J., Delnoij, E., Kuipers, J. A. M., & van Swaaij, W. P. M. (1997). An engineering model for dilute riser flow. *Powder Technology*, *90*(2), 115–123.

Noymer, P. D., & Glicksman, L. R. (1999). Near-wall hydrodynamics in a scale-model circulating fluidized bed. *International Journal of Heat and Mass Transfer*, *42*(8), 1389–1403.

O'Dea, D. P., Rudolph, V., & Chong, Y. O. (1990a). Gas–solids flow through the bottom restriction of an inclined standpipe. *Powder Technology*, *62*(3), 291–297.

O'Dea, D. P., Rudolph, V., Chong, Y. O., & Leung, L. S. (1990b). The effect of inclination on fluidized beds. *Powder Technology*, *63*(2), 169–178.

Paiva, J. M., Pinho, C., & Figueiredo, R. (2004). The influence of the distributor plate on the bottom zone of a fluidized bed approaching the transition from bubbling to turbulent fluidization. *Chemical Engineering Research and Design*, *82*(1), 25–33.

Pallarés, D., & Johnsson, F. (2006). Macroscopic modelling of fluid dynamics in large-scale circulating fluidized beds. *Progress in Energy and Combustion Science*, *32*(5-6), 539–569.

Pang, S. (2009). Overview of up to date progress and challenges in biomass gasification. In *Workshop of Biomass Gasification Technology and Biomass Energy*.

Pfeifer, C., Puchner, B., & Hofbauer, H. (2009). Comparison of dual fluidized bed steam gasification of biomass with and without selective transport of CO_2. *Chemical Engineering Science*, *64*(23), 5073–5083.

Prakongkep, N., Suddhiprakarn, A., Kheoruenromne, I., & Gilkes, R. J. (2010). Sem image analysis for characterization of sand grains in thai paddy soils. *Geoderma*, *156*(1-2), 20–31.

Proll, T., Rupanovits, K., Kolbitsch, P., Bolhàr-Nordenkampf, J., & Hofbauer, H. (2009). Cold flow model study on a dual circulating fluidized bed (DCFB) system for chemical looping processes. *Chemical Engineering & Technology*, *32*(3), 418–424.

Pugsley, T. S., & Berruti, F. (1996). A predictive hydrodynamic model for circulating fluidized bed risers. *Powder Technology*, *89*(1), 57–69.

Qian, F., & Wu, Y. (2009). Effects of the inlet section angle on the separation performance of a cyclone. *Chemical Engineering Research and Design*, *87*(12), 1567–1572. Doi: DOI: 10.1016/j.cherd.2009.05.001.

Rasul, M. G., & Rudolph, V. (2000). Fluidized bed combustion of australian bagasse. *Fuel*, *79*(2), 123–130.

Raub, C. B., Unruh, J., Suresh, V., Krasieva, T., Lindmo, T., Gratton, E., Tromberg, B. J., & George, S. C. (2008). Image correlation spectroscopy of multiphoton images correlates with collagen mechanical properties. *Biophysical Journal*, *94*(6), 2361–2373.

Ravelli, S., Perdichizzi, A., & Barigozzi, G. (2008). Description, applications and numerical modelling of bubbling fluidized bed combustion in waste-to-energy plants. *Progress in Energy and Combustion Science*, *34*(2), 224–253.

Rawle, A. (2009). Particle sizing: An introduction. *Silver Colloids*. Http://www.silver-colloids.com/Tutorials/psintro.html.

Reh, L. (1999). Challenges of circulating fluid-bed reactors in energy and raw materials industries. *Chemical Engineering Science*, *54*(22), 5359–5368.

Reh, L. (2003). Development potentials and research needs in circulating fluidized bed combustion. *China Particuology*, *1*(5), 185–200.

Rhodes, M. J., Wang, X. S., Cheng, H., Hirama, T., & Gibbs, B. M. (1992). Similar profiles of solid flux in circulating fluidized-bed risers. *Chemical Engineering Science*, *47*(7), 1635–1643.

Richtberg, M., Richter, R., & Wirth, K. E. (2005). Characterization of the flow patterns in a pressurized circulating fluidized bed. *Powder Technology*, *155*(2), 145–152.

Sanderson, J., & Rhodes, M. (2005). Bubbling fluidized bed scaling laws: Evaluation at large scales. *AIChE Journal*, *51*(10), 2686–2694.

Sau, D. C., Mohanty, S., & Biswal, K. C. (2008). Critical fluidization velocities and maximum bed pressure drops of homogeneous binary mixture of irregular particles in gas-solid tapered fluidized beds. *Powder Technology*, *186*(3), 241–246.

Scala, F., Chirone, R., & Salatino, P. (2006). Combustion and attrition of biomass chars in a fluidized bed. *Energy & Fuels*, *20*(1), 91–102.

Schlichthaerle, P., & Werther, J. (1999). Axial pressure profiles and solids concentration distributions in the cfb bottom zone. *Chemical Engineering Science*, *54*(22), 5485–5493.

Schoenfelder, H., Kruse, M., & Werther, J. (1996). Two-dimensional model for circulating fluidized-bed reactors. *AIChE Journal*, *42*(7), 1875–1888.

Schut, S. B., van der Meer, E. H., Davidson, J. F., & Thorpe, R. B. (2000). Gas-solids flow in the diffuser of a circulating fluidised bed riser. *Powder Technology*, *111*(1-2), 94–103.

Senior, R. C., & Brereton, C. (1992). Modelling of circulating fluidised-bed solids flow and distribution. *Chemical Engineering Science*, *47*(2), 281–296.

Shalaby, H., Pachler, K., Wozniak, K., & Wozniak, G. (2005). Comparative study of the continuous phase flow in a cyclone separator using different turbulence models. *International Journal for Numerical Methods in Fluids*, *48*(11), 1175–1197.

Sharma, A. K., Tuzla, K., Matsen, J., & Chen, J. C. (2000). Parametric effects of particle size and gas velocity on cluster characteristics in fast fluidized beds. *Powder Technology*, *111*(1-2), 114–122.

Smolders, K., & Baeyens, J. (2001). Hydrodynamic modelling of the axial density profile in the riser of a low-density circulating fluidized bed. *The Canadian Journal of Chemical Engineering*, *79*(3), 422–429.

Speziale, C. G., Sarkar, S., & Gatski, T. B. (1991). Modelling the pressure-strain correlation of turbulence: an invariant dynamical systems approach. *Journal of Fluid Mechanics*, *227*, 245–272.

Sternéus, J., Johnsson, F., & Leckner, B. (2002). Characteristics of gas mixing in a circulating fluidised bed. *Powder Technology*, *126*(1), 28–41.

Ståhl, K., & Neergaard, M. (1998). IGCC power plant for biomass utilisation, Värnamo, Sweden. *Biomass and Bioenergy*, *15*(3), 205–211.

Svensson, A., Johnsson, F., & Leckner, B. (1996). Fluidization regimes in non-slugging fluidized beds: the influence of pressure drop across the air distributor. *Powder Technology*, *86*(3), 299–312.

Taghipour, F., Ellis, N., & Wong, C. (2005). Experimental and computational study of gas-solid fluidized bed hydrodynamics. *Chemical Engineering Science*, *60*(24), 6857–6867.

Takeshita, T., & Yamaji, K. (2008). Important roles of fischer-tropsch synfuels in the global energy future. *Energy Policy*, *36*(8), 2773–2784.

Tanaka, I., Shinohara, H., Hirosue, H., & Y., T. (1972). Elutriation of fines from fluidized bed. *Journal of Chemical Engineering of Japan*, *5*(1), 51–57.

Tsukada, M., Ito, M., Kamiya, H., & Horio, M. (1997). Three-dimension imaging of particle clusters in dilute gasŮsolid suspension flow. *The Canadian Journal of Chemical Engineering*, *75*(2), 466–470.

Utikar, R. D., Tade, N., Li, M., Evans, Q., Glenny, G., & Pareek, V. (2010). *Hydrodynamic simulation of cyclone separators*. InTech.

van der Meer, E. H., Thorpe, R. B., & Davidson, J. F. (2000). Flow patterns in the square cross-section riser of a circulating fluidised bed and the effect of riser exit design. *Chemical Engineering Science*, *55*(19), 4079–4099.

Versteeg, H., & Malalasekera, W. (2007). *An Introduction to Computational Fluid Dynamics: The Finite Volume Method*. Pearson Education.

Wan, G., Sun, G., Xue, X., & Shi, M. (2008). Solids concentration simulation of different size particles in a cyclone separator. *Powder Technology*, *183*(1), 94–104.

Wang, B., Xu, D. L., Chu, K. W., & Yu, A. B. (2006). Numerical study of gas-solid flow in a cyclone separator. *Applied Mathematical Modelling*, *30*(11), 1326–1342.

Werther, J. (2000). Fluidization technology development – the industry/academia collaboration issue. *Powder Technology*, *113*(3), 230–241.

Wu, C., Yin, X., Ma, L., Zhou, Z., & Chen, H. (2008). Design and operation of a 5.5 mwe biomass integrated gasification combined cycle demonstration plant. *Energy and Fuels*, *22*(6), 4259–4264.

Xiang, R. B., & Lee, K. W. (2008). Effects of exit tube diameter on the flow field in cyclones. *Particulate Science and Technology: An International Journal*, *26*(5), 467 – 481.

Xu, G., Murakami, T., Suda, T., Matsuzawa, Y., & Tani, H. (2006). The superior technical choice for dual fluidized bed gasification. *Industrial and Engineering Chemistry Research*, *45*(7), 2281–2286.

Xu, Q., Pang, S., & Levi, T. (2011a). Reaction kinetics and producer gas compositions of steam gasification of coal and biomass blend chars, part 1: Experimental investigation. *Chemical Engineering Science*, *66*(10), 2141–2148.

Xu, Q., Pang, S., & Levi, T. (2011b). Reaction kinetics and producer gas compositions of steam gasification of coal and biomass blend chars, part 2: Mathematical modelling and model validation. *Chemical Engineering Science*, *66*(10), 2232–2240.

Xu, R., Ferrante, L., Briens, C., & Berruti, F. (2009). Flash pyrolysis of grape residues into biofuel in a bubbling fluid bed. *Journal of Analytical and Applied Pyrolysis*, *86*(1), 58–65.

Yan, A., Ball, J., & Zhu, J. (2005). Scale-up effect of riser reactors (3) axial and radial solids flux distribution and flow development. *Chemical Engineering Journal*, *109*(1-3), 97–106.

Yan, A., Pärssinen, J. H., & Zhu, J.-X. (2003). Flow properties in the entrance and exit regions of a high-flux circulating fluidized bed riser. *Powder Technology*, *131*(2-3), 256–263.

Yang, H., Yue, G., Xiao, X., Lu, J., & Liu, Q. (2005). 1D modeling on the material balance in CFB boiler. *Chemical Engineering Science*, *60*(20), 5603–5611.

Yang, S., Yang, H., Zhang, H., Li, J., & Yue, G. (2009). Impact of operating conditions on the performance of the external loop in a CFB reactor. *Chemical Engineering and Processing: Process Intensification*, *48*(4), 921–926.

Yu, J., Yeoh, G., & Liu, C. (2008). *Computational Fluid Dynamics: A Practical Approach*. Burlington, MA, USA: Butterworth-Heinemann.

Zhang, W., Tung, Y., & Johnsson, F. (1991). Radial voidage profiles in fast fluidized beds of different diameters. *Chemical Engineering Science*, *46*(12), 3045–3052.

Zhu, H., & Zhu, J. (2008). Comparative study of flow structures in a circulating-turbulent fluidized bed. *Chemical Engineering Science*, *63*(11), 2920–2927.

Zijerveld, R. C., Johnsson, F., Marzocchella, A., Schouten, J. C., & van den Bleek, C. M. (1998). Fluidization regimes and transitions from fixed bed to dilute transport flow. *Powder Technology*, *95*(3), 185–204.

Zou, L. M., Guo, Y. C., & Chan, C. K. (2008). Cluster-based drag coefficient model for simulating gas-solid flow in a fast-fluidized bed. *Chemical Engineering Science*, *63*(4), 1052–1061.

Appendix A

Scaling Laws

A.1 SEM Analysis of Copper Particles

The copper particles used in the cold model experiments were analysis using scanned Electron Microscopy (SEM) for determination of distributions of particle shape and size. In the SEM analysis, the threshold was adjusted in an imaging software (ImageJ) to give the outline of the particles. The top image in Fig. A.1 shows that most of the particles have a flake structure, and the bottom image in Fig. A.1 is the corresponding threshold, with the boundaries of each particle demarcated. From the boundaries of the particles in the threshold adjusted image, ImageJ was able to calculate the particle circularity for the particles tested based on Eq. (3.5) as mentioned in Chapter 3.

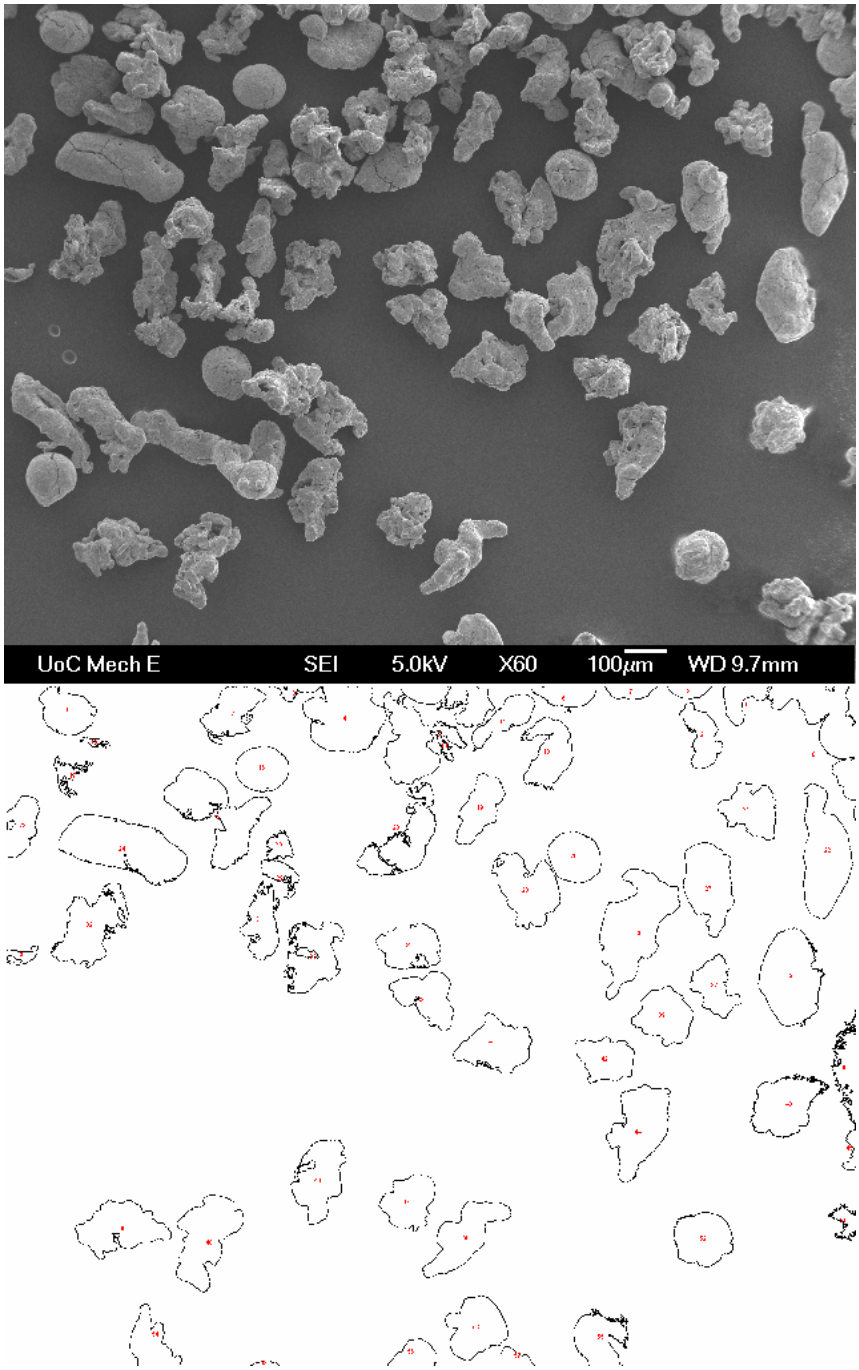

Fig. A.1: Top: SEM image of copper particles; Bottom: Outline of particles for particle circularity determination from ImageJ software.

A.2 Determination of Particle Diameter

A particle size analyzer (Microtrac X100) was used to determine the particle size distribution, using a dynamic light scattering measuring technique. In the analysis, the particles are suspended in a dispersing medium, and light from a laser diode is guided to

the sample through a surface waveguide power shifter. Light scattered from each particle is then compared with a coherent, undisturbed light to create a frequency difference in the audio range. This difference is amplified, filtered, digitized and mathematically analyzed to obtain the particle size distribution in percentage volume (Microtrac, 2000).

From the particle size distribution the particle mean diameter were determined. For determination of the particle mean diameter, several methods are available as presented by Allen (1968). The number mean diameter is a population balance and is simply an average of the size of particles measured. The volume moment mean diameter takes the volume into account and is strongly weighted by coarse particles. The surface volume mean diameter is representative of a particle surface area measurement (Rawle, 2009). Since the particle contact surface area takes part directly in a gasification reaction and has a direct effect on the performance, it is logical to specify the particle diameter which relates to the surface area. Therefore, the surface volume diameter was used throughout this thesis which is also known as the Sauter mean diameter, d_p (Rawle, 2009). Fig. A.2 shows a typical size distribution of the copper particles in volume distribution.

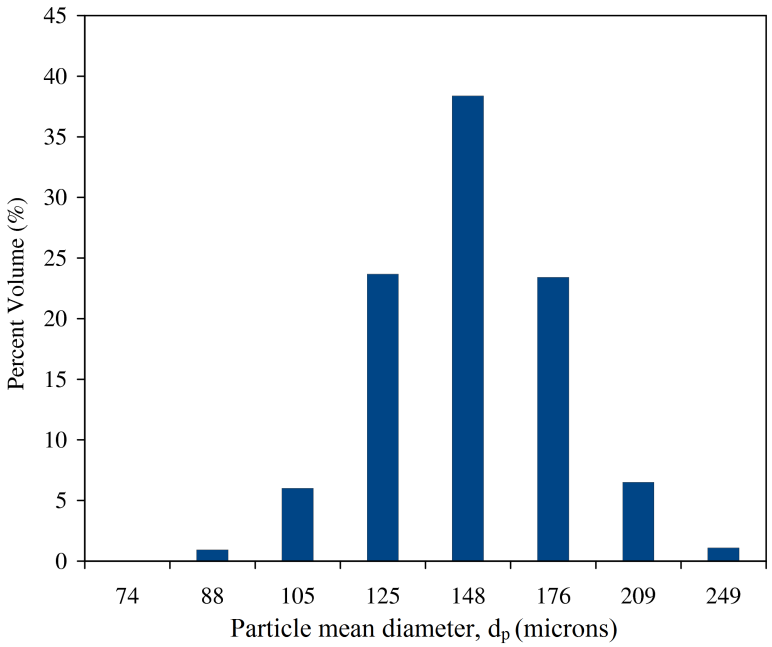

Fig. A.2: Size distribution of copper particles in percent volume

Table A.1: Dimensionless Parameters in Güssing Plant (Kaiser et al., 2003) and DFB cold model in this study.

Parameters	Güssing Plant*	Cold Model**
Density of gas (kg/m^3)	0.30	1.18
Viscosity (Pa.s)	46.82×10^{-6}	19×10^{-6}
Density of particles (kg/m^3)	2500	8940
Particle diameter (μm)	530	138
Density number, De	1.2×10^{-4}	
Density Ratio, De	1.21×10^{-4}	1.35×10^{-4}

* from (Kreuzeder et al., 2007)**from (Kaiser et al., 2003).

A.3 Calculation of Dimensionless Parameters

This section documents the calculation and comparison of the dimensionless parameters of the scaling laws between the cold model and the gasification plant in Güssing gasification plant in Austria. The dimensionless parameters have been listed in Chapter 3. Table A.1 shows the values of parameters in the 8MW$_{th}$ Güssing plant and those of the corresponding parameters in the cold model which are used to calculate the dimensionless parameters in Eqs. A.4 to A.8 are the details for calculating the dimensionless parameters. Using the values given in Table A.1, and with the particle circularity of the bed material measured as 0.70 from ImageJ, the density ratio, De_h, and the Archimedes number, Ar_h for the gasifier (with subscript h denoting dimensionless numbers for gasifier, are calculated first as follows:

$$De_h = \frac{\rho_g}{\rho_s} = 0.3/2500 = 1.21 \times 10^{-4} \tag{A.1}$$

$$Ar_h = \frac{(\phi d_p)^3 \rho_g (\rho_s - \rho_g) g}{\mu^2} = \frac{(0.7 \times 530 \times 10^{-6})^3 (0.3)(2500 - 0.3)(9.8)}{(46.82 \times 10^{-6})^2} = 171 \tag{A.2}$$

In a similar way, the Archimedes number for the cold model, Ar_c (with subscript c denoting dimensionless numbers for the cold model) is calculated for the copper particles as the bed material which has the particle density of 8940 kg/m^3, a particle diameter of 138 μm and a particle circularity ϕ of 0.60.

$$Ar_c = \frac{(0.6 \times 138 \times 10^{-6})^3 (1.2)(8940 - 1.2)(9.8)}{(19 \times 10^{-6})^2} = 163 \tag{A.3}$$

Table A.2: Dimensions of Güssing Plant (Kaiser et al., 2003), cold model (Kaiser et al., 2003) and current proposed dimensions

	Güssing Plant*	Cold Model**	Current Dimensions
Riser top diameter, d_{r1}(mm)	850	175	210
Riser bottom diameter, d_{r2}(mm)	-	150	180
Total Riser height, h_r(mm)	10000	2200	2600
d_{r1} / d_{r2}	-	1.167	1.167
h_r / d_{r1}	11.76	12.57	12.38

from (Kreuzeder et al., 2007) ** from (Kaiser et al., 2003)

The density ratio De_c, was similar to that of the Güssing plant:

$$De_c = \frac{\rho_g}{\rho_s} = 1.205/8940 = 1.35 \times 10^{-4} \tag{A.4}$$

For the above conditions in the Güssing gasification plant, the minimum fluidization velocity, u_{mf}, is calculated from Eq. (A.5) (Kunii & Levenspiel, 1991) to be 0.34 m/s. Then the flow number for the gasification plant, Fl_h, is calculated to be 35 with superficial gas velocity of 12 m/s (Kreuzeder et al., 2007). Using the same flow number and the calculated minimum fluidization velocity, the superficial gas velocity that is estimated required for the bed to fluidize in the cold model, $u_{o,c}$, is determined:

$$u_{mf} = \frac{d_p^2(\rho_s - \rho_g)g}{150\mu_g}\left(\frac{\varepsilon_{mf}^3\phi_s^2}{1-\varepsilon_{mf}}\right) \tag{A.5}$$

$$Fl_h = \frac{u_o}{u_{mf}} = \frac{12}{0.34} = 35 \tag{A.6}$$

$$u_{mf,c} = 0.103 m/s \tag{A.7}$$

$$u_{o,c} = 0.103 Fl_h = 0.103(35) = 3.61 m/s \tag{A.8}$$

Table A.2 gives the dimensions of the scaled-down cold model presented by Kaiser et al. (2003), based on the Güssing plant (Löffler et al., 2003; Kaiser et al., 2003). The dimensions for the proposed scaled down model is also shown.

An exact match between all the dimensionless numbers is impossible, therefore the scaling laws are within a range of accuracy to ensure dynamic similarity. For example, the particle shape varies during the gasification process, and the Archimedes number changes. The variation of the Archimedes number and its effect on the dynamic similarity should

be validated with the actual gasification plant in Güssing, which is an exercise that could be performed in the future.

Appendix B

Instrumentation for the Cold Model

Fig. B.1 shows the cold model of the dual fluidized bed (DFB) gasification plant.

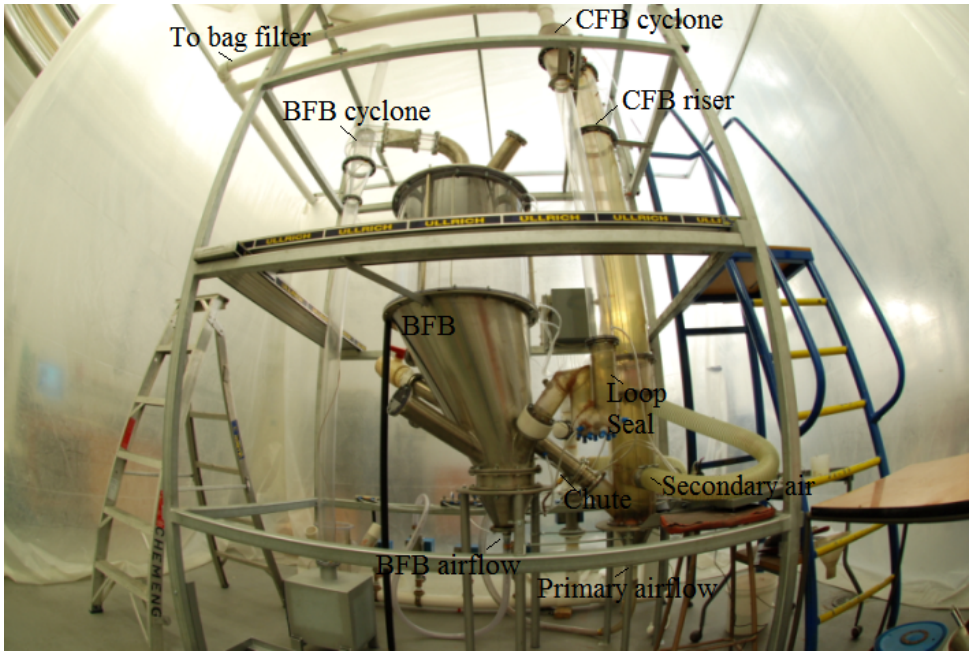

Fig. B.1: Cold model of dual fluidized bed.

The following sections describe the instrumentation used for the plant.

B.1 Description of Instruments

B.1.1 Flow Meters

This section describes the procedure for calibrating the airflow meters. The flow rate in a pipe was determined by measuring the velocity distribution with a Pitot tube velocity meter and multiplying that velocity with the representative areas. The Pitot tube was traversed along the diameter of the pipe, having positions of $x_1, x_2, x_3 ..., x_n$ as depicted in Fig. B.2. The corresponding velocities are $v_1, v_2, v_3 ..., v_n$. These values are then multiplied with the corresponding representative areas of $A_1, A_2, A_3, ...A_n$. The volumetric airflow rate, with the secondary airflow as an example, is then the sum of these product values, given as:

$$\begin{aligned} Q_i &= v_n A_n \\ &= v_1 A_1 + v_2 A_2 + v_3 A_3 \end{aligned} \tag{B.1}$$

Table B.1 shows the measurement positions for calibrating the primary and the secondary airflow meters, with the corresponding calibration curves shown in Figs. B.3 and B.4. From these figures, it is seen that the correlation coefficients for the primary and the secondary airflow measurements are 0.9242 and 0.9479, respectively, thus giving confidence in the measured air flow rates in this study. The BFB, chute and loop seal flow meters were also calibrated using the similar procedure and the results show the similar confidence in the air flow measurements.

Table B.1: Details for Pitot tube measurement of flow rate

	$D_1(mm)$	$D_2(mm)$	$D_3(mm)$
Primary Air Flowmeter (1in. Diameter)	25.0	5.0	-
Secondary Air Flowmeter (3in. Diameter)	75.0	65.0	55.0
	$x_1(mm)$	$x_2(mm)$	$x_3(mm)$
Primary Air Flowmeter (1in. Diameter)	5.0	12.5	-
Secondary Air Flowmeter (3in. Diameter)	5.0	10.0	37.5

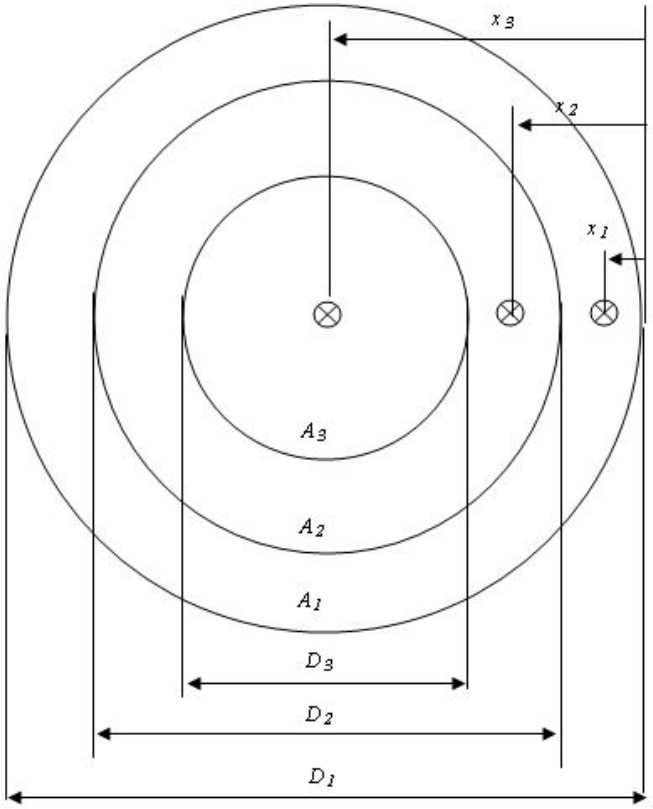

Fig. B.2: Calibration of flowmeter

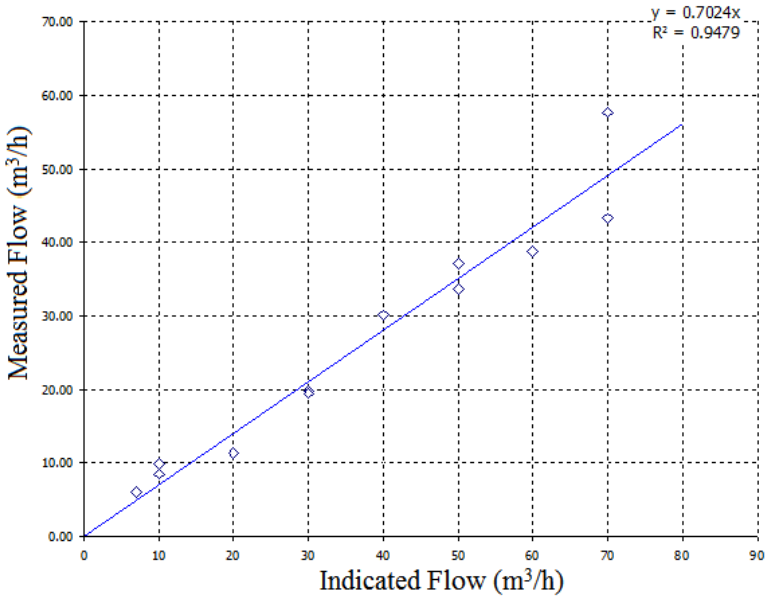

Fig. B.3: Calibration curve for primary air flowmeter

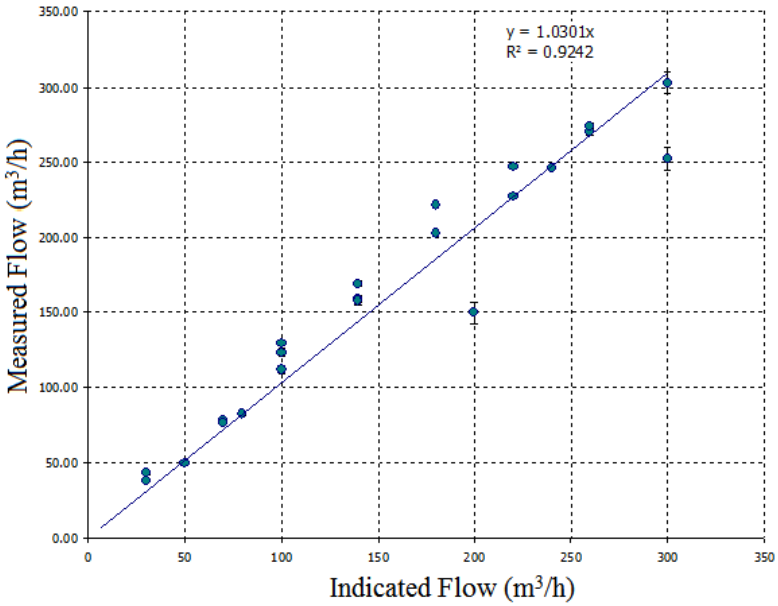

Fig. B.4: Calibration curve for secondary air flowmeter

B.1.2 Temperature Correction for Volumetric Flow Rates

During the operation of the DFB system loaded with bed material, the temperature of the air increases due to an increase in the plant pressure drop and friction incurred from the high density copper. As the temperature increases, the air density decreases, thereby changing the total volumetric airflow through the plant. Therefore, the total airflow has to be corrected to the operating temperature. The volumetric airflow was corrected to the temperature using the following for variable area flow meters:

$$Q_c = Q_o \sqrt{\frac{T_2}{T_1}} \tag{B.2}$$

where Q_c is the corrected volumetric airflow (m^3/s); Q_o is the volumetric flow rate at normal conditions (m^3/s); T_1 is the temperature of air at normal conditions (K); and T_2 is the actual temperature of the air supply (K). It should be noted that the manufacturers of the flow meters calibrated at an air temperature of $20°C$, therefore T_1 is $20°C$ in this case.

B.1.3 Pressure Drop Transducers

The pressure drop was measured using pressure transducers that were purchased from Honeywell, and were connected to a digital display cum data logger. The pressure

sensor data was exported and converted using a dedicated software, TrendServer Pro, also provided by Honeywell. Fig. B.5 shows an example of the recorded pressure data using the logged pressure sensor in TrendServer Pro during an experimental run in the DFB.

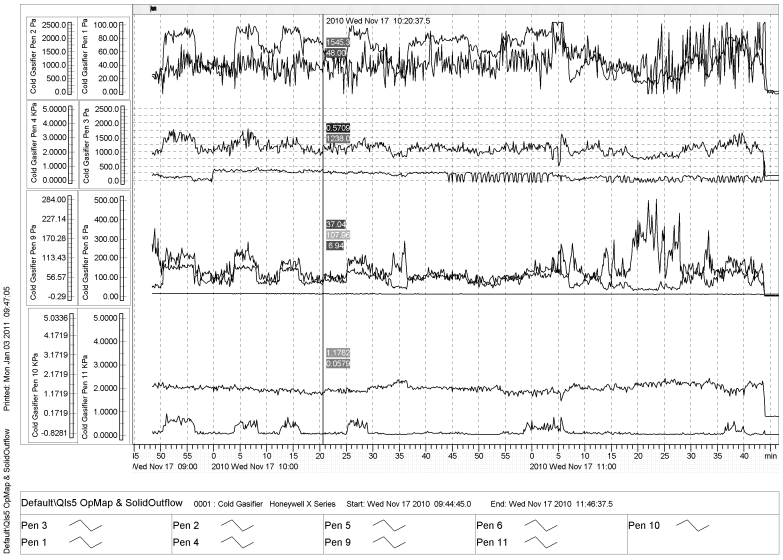

Fig. B.5: Recorded pressure sensor data using digital display and recorder from Honeywell

B.1.4 CFB Riser Gas Velocity Profile

The local gas velocity within the CFB riser was measured using a Pitot tube velocity meter at the same axial heights where the particles were sampled in the suction probe measurements. The measurements of the local gas velocities were used to determine the suction velocity required for iso-kinetic sampling of the particles. A radial profile of the local gas velocity was determined by traversing the Pitot tube across the cross-section of the riser for a superficial gas velocity u_o of 1.20 m/s.

Fig. B.6 shows the radial profile of the gas velocity in the riser for two different measurements, and it indicates that turbulence caused an asymmetrical radial gas velocity profile about the axis of the riser. The flow turbulence causes the local gas velocity across the cross-section of the riser to fluctuate within 30% of the superficial gas velocity of 1.20 m/s although most of the data were within 10% of the average value. Due to this turbulence, an accurate value for the local gas velocity was unable to be attained, and is

even vague when the system is loaded with solids. A similar observation was also made by Werther (2000), who stated that local gas velocity in the CFB riser is unknown, as the flow direction of gas, and even the solids, may reverse instantaneously in the riser.

A reasonable approximation for the suction velocity would then be the superficial gas velocity. The effect of this approximation, and the variation in the suction velocity on the sampled particle mass flow rate, is discussed further in the Section B.1.5.

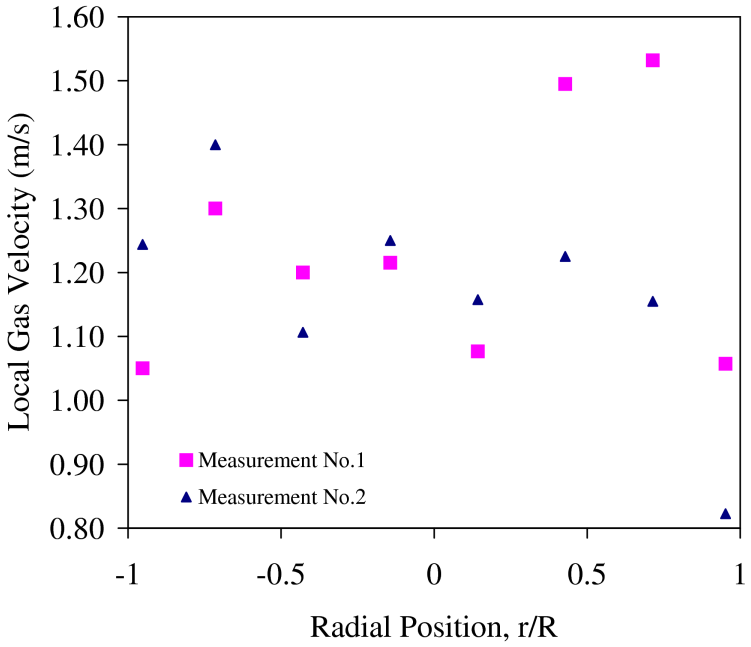

Fig. B.6: Superficial gas velocity profile measured by Pitot tube for total gas flowrate of 150m^3/h (superficial gas velocity=1.20m/s).

B.1.5 Suction Probe and Effect of Suction Velocity

A suction probe was used to measure the local solids volume fraction within circulating fluidized bed at axial locations of 0.95, 1.55 and 2.55 m above the air distributor plate. At each axial location, the suction probe was traversed at three radial positions of 0, 0.060 and 0.105 m from the axis of the riser. Fig. B.7 shows the experimental set-up using the suction probe.

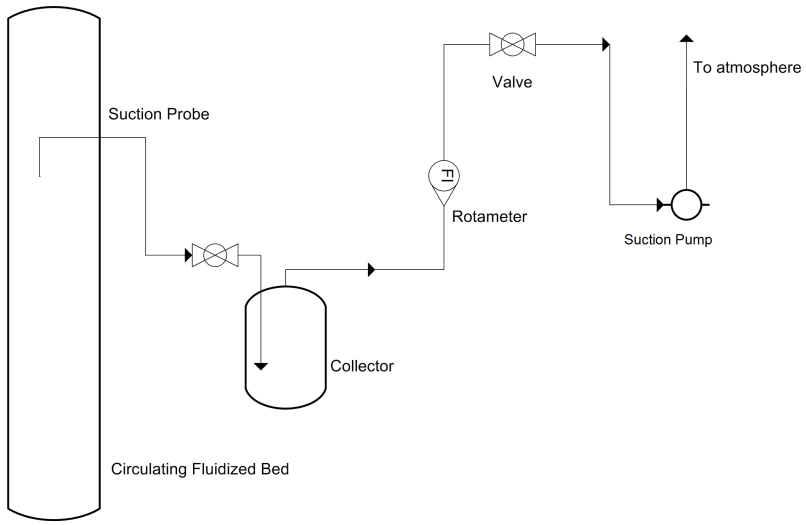

Fig. B.7: Suction probe experimental set-up

In the measurements, a suction pump was firstly switched on to provide a suction velocity through the probe at the superficial gas velocity which allowed for iso-kinetic sampling of the solids. A valve was then opened to allow the solids to flow through to a container where the particles were collected at the bottom of the container while the gas flew through a connecting tube to the suction pump. The sampling time, Δt, was kept constant at two minutes or more before the valve was closed for completing one measurement. The local solids mass flux is determined by:

$$G_s = \frac{\Delta m}{A_{suct} \Delta t} \tag{B.3}$$

where Δm is the mass of the container before and after sampling of the particles; Δt is the measurement time; A_{suct} is the cross-sectional area of the suction probe.

During the measurements, it was noted that the particles flew into the bend of the suction probe and no particles were observed to flow back into the main gas stream upon impact with the elbow section of the probe. After sampling of the particles was done, with the valve was closed and suction pump was turned off, the suction probe was removed from the CFB and was flushed with compressed air to check for accumulation of particles within the connecting tubes. Negligible amount or no particles were found in the probe and connecting pipes. In the container, the copper particles were observed to gush into the container and settled at the bottom, and no loss of particles was observed through the top outlet of the container. Considering that the density of copper is very

high (8940 kg/m^3) and the particle size is within a range of 60 to 160 μm (with a mean diameter of 138 μm), the particles are large and heavy enough to be collected in the container without re-entrainment into the suction gas stream. From these observations, it can be said that the flux of particles into the suction probe are all captured in the container, and no particles accumulated within the suction probe, while no solids were lost through the gas outlet.

No filter was used in the suction probe system, since a large pressure drop is incurred through the filter due to accumulation of dust particles. The filter is actually a security filter to prevent the particles from damaging the pump. Over the two years of using the suction probe, no loss of pump performance, in terms of the suction flow rate provided, was observed.

The suction velocity was varied within the range of the iso-kinetic sampling velocity to determine the effect on the mass collected in the container. The operational parameters during this experiment include a primary airflow of 53 m^3/h and a secondary airflow of 320 m^3/h, while the loop seal airflow and chute airflow was both controlled at 5 m^3/h. The total airflow within the CFB riser was 373 m^3/h, giving a superficial gas velocity of 2.99 m/s.

Fig. B.8 shows that within 90 to 150% of the iso-kinetic sampling velocity, no significant effect was found on the mass flow rate of the upward flowing particles. The upward momentum of the particles results in a sufficiently high inertia to render the particles tolerant to changes in suction velocity. Similar findings have been found by other researchers. Schut et al. (2000) tested a wider range of the suction velocity, between 0.5 to 2.0 m/s, and found that the suction velocity did not have an effect on the amount of particles collected. Other researchers have tested different range of suction velocities and concluded that precise iso-kinetic sampling is not required for sampling the solid particles (Grace et al., 1997; Werther, 2000; van der Meer et al., 2000; Davidson, 2000; Schut et al., 2000). The same conclusion can be reached in this finding that the suction velocity did not make a difference to the mass of particles collected, and precise iso-kinetic sampling of the particles is not required.

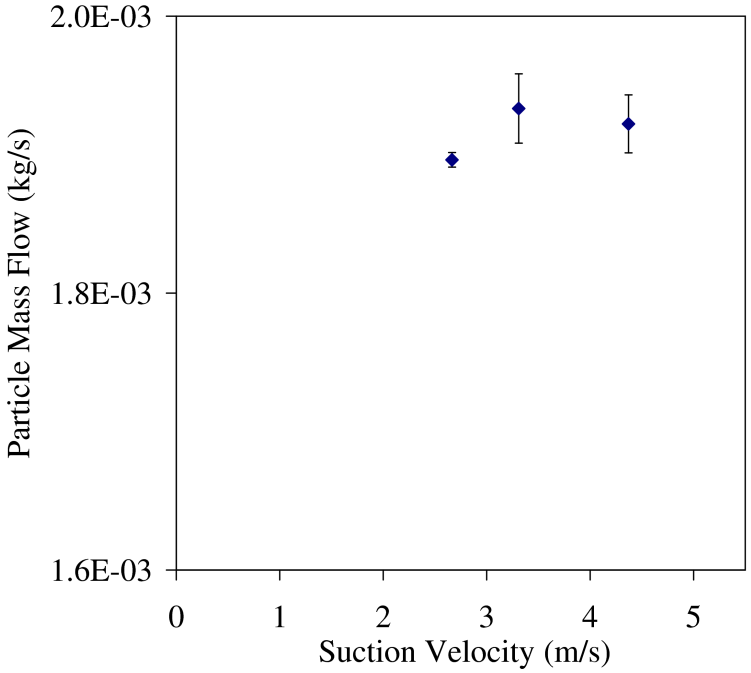

Fig. B.8: Particle mass flow rate of with varying suction velocity. Iso-kinetic sampling at a gas velocity of 2.99m/s

Appendix C

Selected Samples of Experimental Data and Result Analysis

C.1 Phase I

C.1.1 Operational Map for CFB

The corresponding measurement points and the observed operating conditions for deriving Fig. 3.3 are shown in Table C.1.

C.1.2 Radial Profile of Solids Flux

Fig. C.1 shows a five point measurement of the solids flux across the diameter of the riser, compared to a three point measurement, for the same experimental conditions. The five point measurement shows that the radial profile of the solids flux (and correspondingly the solids fraction) is parabolic, and is almost similar to that in profile from that of the three point measurement. Only three radial locations were taken for measurement in this study to reduce the required sampling time.

Table C.1: Corresponding measurement points and observed operating conditions for Fig. 3.3

Primary airflow rate, Q_{pri} (m^3/h)	Secondary airflow rate, Q_{sec}	Observed condition
32	171	Bypass in loop-seal.
53	171	No loop-seal bypass.
75	171	No loop-seal bypass.
96	171	No loop-seal bypass.
32	318	No loop-seal bypass.
96	318	No loop-seal bypass.
32	106	Bypass in loop seal.
53	106	No bypass. Elutriating.
75	106	No bypass. Elutriating.
96	106	No bypass. Elutriating.
53	96	Bypass in loop seal.
96	50	Bypass in loop seal. Elutriating

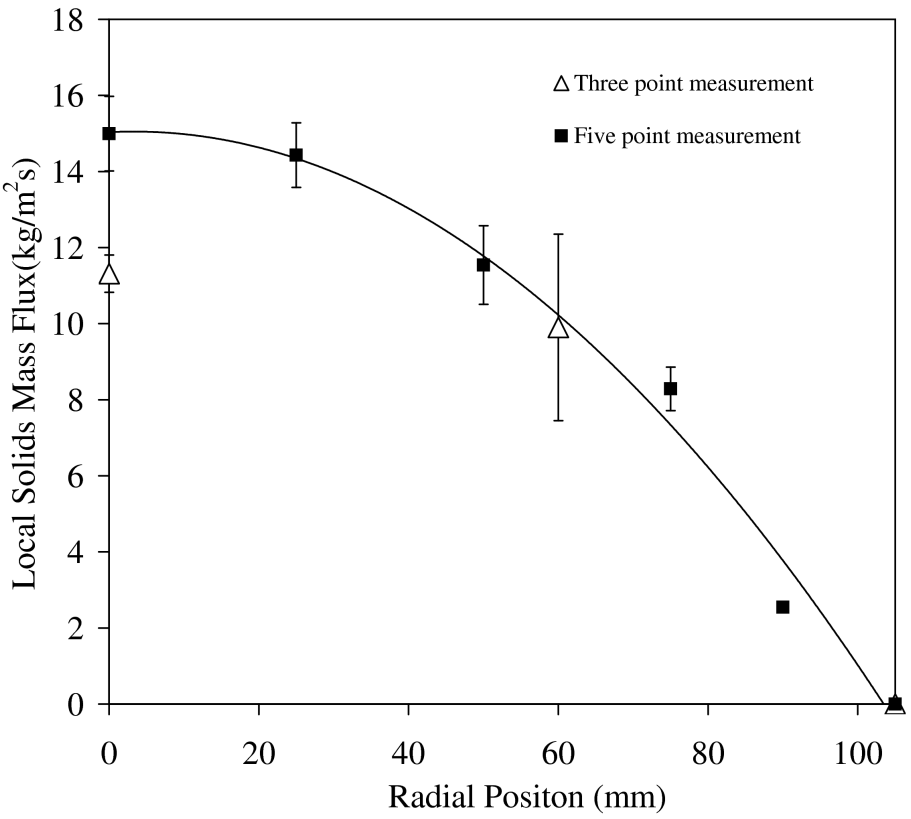

Fig. C.1: Five and three point measurements of the solids flux across the riser.

Table C.2: Corresponding solids mass flux for varying primary airflow rate and radial positions for Phase I (CFB) at a height of 2.55 m. Q_{ls} 6 m^3/h; Q_{sec} 171 m^3/h. This data is sampled from the results in Fig. 3.6

Primary airflow rate, Q_{pri} (m^3/h)	Solids mass flux at distance of 0 mm from center of riser (kg/m^2s)	Solids mass flux at distance of 60 mm from center of riser (kg/m^2s)	Solids mass flux at distance of 105 mm from center of riser (kg/m^2s)
32	1.27	0.85	0.000
53	2.69	1.70	0.000
75	10.13	5.23	0.000
96	16.37	12.10	0.000

Table C.3: Corresponding solids core flow rate and solids outflow rate for calculating aerodynamic factor. Q_{ls} 5 m^3/h; Q_{sec} 171 m^3/h. The standard deviation (SD) was included for the corresponding parameters. This data is sampled from the results shown in Fig. 3.11

Primary airflow rate, Q_{pri} (m^3/h)	Solids core flow rate, $\dot{m}_{core}$ (kg/s)	SD, $\dot{m}_{core}$	Solids outflow rate, $\dot{m}_{so}$ (kg/s)	SD, $\dot{m}_{so}$	Aerodynamic factor, Φ_d
32	0.023	0.0053	0.026	0.0035	10.60
53	0.074	0.0051	0.040	0.0050	5.08
75	0.150	0.0051	0.080	0.0091	5.02
96	0.293	0.0051	0.120	0.0134	3.86

C.1.3 Solids Circulation Rate

The corresponding local solids flux for Fig. 3.6 in Chapter 3 is shown in Table C.2 for Phase I only. Table C.3 shows the solids core flow rate and solids outflow rate, which were used to calculate the corresponding aerodynamic factor as shown in Fig. 3.11,

C.1.4 Pressure Drop

The pressure drop of the plant was time-averaged over a certain time period of 2 to 9 min. As the pressure drop sampling frequency of the TrendServer Pro was 1 s^{-1}, the total number of data points used for time-averaging of the pressure drop was at least 120. Table C.5 shows the time-averaged pressure drops for various locations in the CFB riser at various primary airflow rates that were used in Figs. 3.13, 3.14 and 3.15.

Table C.4: Pressure drop across various locations for Phase I (CFB riser). Q_{ls} 5 m^3/h; Q_{sec} 171 m^3/h. The standard deviation (SD) was included for the corresponding parameters. This data was used for compiling results shown in Figs. 3.13, 3.14, and 3.15

Primary airflow rate, Q_{pri} (m^3/h)	Riser upper section, ΔP_{ur} (Pa)	Loop seal, ΔP_{ls} (kPa)	Riser bottom section, ΔP_{br} (Pa)	SD, ΔP_{ur} (Pa)	SD, ΔP_{ls} (Pa)	SD, ΔP_{br} (Pa)
32	16.52	2.03	1096.68	1.67	0.07	26.44
53	24.37	2.28	953.86	3.17	0.08	22.87
75	43.12	2.43	816.76	6.28	0.07	38.22
96	70.08	2.52	675.14	7.33	0.07	46.26

C.1.5 Hydrodynamic Modelling of Phase I

Fig. C.2 shows a sample of the predicted results from the hydrodynamic model developed in Microsoft Excel, which results are presented in Chapter 4. The hydrodynamic model predicts the parameters (solid fraction, solid mass flow rate, and pressure drop) in a discretized height element of 0.001 m, starting from the dense zone at 0.18 m from the distribution plate, up to the top of the riser at 2.60 m. Table C.5 shows a sample of the measured and predicted solid fraction at the height of 2.55 m in the riser.

Length (m)	Us (m/s)	Re	CD	Fgravity	Fdrag	Del Us (m/s)	Voidage in core ()	Solid Fraction ()	Core Upward Flow (kg/s)
0.18	2.915	5.52E-07	43478261	-2.61E-08	1.40467E-15	-3.37E-03	0.97337	0.02663	17.65426158
0.181	2.91E+00	1.86E-02	1292	-2.61E-08	4.72713E-11	-3.36E-03	0.97350	0.02650	17.55147794
0.182	2.91E+00	3.71E-02	646	-2.61E-08	9.45129E-11	-3.36E-03	0.97362	0.02638	17.44928787
0.183	2.90E+00	5.57E-02	431	-2.61E-08	1.41723E-10	-3.36E-03	0.97375	0.02625	17.347688
0.184	2.90E+00	7.42E-02	323	-2.61E-08	1.88902E-10	-3.36E-03	0.97387	0.02613	17.24667501
0.185	2.90E+00	9.28E-02	259	-2.61E-08	2.3605E-10	-3.35E-03	0.97399	0.02601	17.14624555
0.186	2.89E+00	1.11E-01	223	-2.61E-08	2.92564E-10	-3.35E-03	0.97411	0.02589	17.04639633
0.187	2.89E+00	1.30E-01	192	-2.61E-08	3.42415E-10	-3.35E-03	0.97423	0.02577	16.94713122
0.188	2.89E+00	1.48E-01	168	-2.61E-08	3.92513E-10	-3.35E-03	0.97435	0.02565	16.84844184
0.189	2.88E+00	1.67E-01	150	-2.61E-08	4.42847E-10	-3.34E-03	0.97447	0.02553	16.75032512
0.19	2.88E+00	1.85E-01	136	-2.61E-08	4.93404E-10	-3.34E-03	0.97459	0.02541	16.65277802
0.191	2.88E+00	2.04E-01	124	-2.61E-08	5.44175E-10	-3.34E-03	0.97471	0.02529	16.55579748
0.192	2.87E+00	2.22E-01	114	-2.61E-08	5.95152E-10	-3.33E-03	0.97483	0.02517	16.45938046
0.193	2.87E+00	2.40E-01	105	-2.61E-08	6.46326E-10	-3.33E-03	0.97495	0.02505	16.36352393
0.194	2.87E+00	2.59E-01	98	-2.61E-08	6.9769E-10	-3.33E-03	0.97506	0.02494	16.26822487
0.195	2.86E+00	2.77E-01	92	-2.61E-08	7.49238E-10	-3.33E-03	0.97518	0.02482	16.17348026
0.196	2.86E+00	2.96E-01	86	-2.61E-08	8.00964E-10	-3.32E-03	0.97530	0.02470	16.0792871
0.197	2.86E+00	3.14E-01	82	-2.61E-08	8.52863E-10	-3.32E-03	0.97541	0.02459	15.98564241
0.198	2.85E+00	3.32E-01	77	-2.61E-08	9.04929E-10	-3.32E-03	0.97553	0.02447	15.8925432
0.199	2.85E+00	3.51E-01	73	-2.61E-08	9.57157E-10	-3.31E-03	0.97564	0.02436	15.79998651
0.2	2.85E+00	3.69E-01	70	-2.61E-08	1.00954E-09	-3.31E-03	0.97575	0.02425	15.70796938
0.201	2.84E+00	3.87E-01	67	-2.61E-08	1.06208E-09	-3.31E-03	0.97587	0.02413	15.61648886
0.202	2.84E+00	4.05E-01	64	-2.61E-08	1.11477E-09	-3.30E-03	0.97598	0.02402	15.52554203
0.203	2.84E+00	4.24E-01	61	-2.61E-08	1.16761E-09	-3.30E-03	0.97609	0.02391	15.43512597
0.204	2.83E+00	4.42E-01	59	-2.61E-08	1.22058E-09	-3.30E-03	0.97620	0.02380	15.34523777
0.205	2.83E+00	4.60E-01	57	-2.61E-08	1.2737E-09	-3.30E-03	0.97631	0.02369	15.25587453
0.206	2.83E+00	4.78E-01	55	-2.61E-08	1.32695E-09	-3.29E-03	0.97642	0.02358	15.16703338
0.207	2.82E+00	4.96E-01	53	-2.61E-08	1.38033E-09	-3.29E-03	0.97653	0.02347	15.07871144
0.208	2.82E+00	5.15E-01	51	-2.61E-08	1.43384E-09	-3.29E-03	0.97664	0.02336	14.99090586
0.209	2.82E+00	5.33E-01	49	-2.61E-08	1.48748E-09	-3.28E-03	0.97675	0.02325	14.9036138
0.21	2.81E+00	5.51E-01	48	-2.61E-08	1.54123E-09	-3.28E-03	0.97686	0.02314	14.81683242
0.211	2.81E+00	5.69E-01	46	-2.61E-08	1.59511E-09	-3.28E-03	0.97697	0.02303	14.73055892
0.212	2.81E+00	5.87E-01	45	-2.61E-08	1.64911E-09	-3.27E-03	0.97708	0.02292	14.64479047
0.213	2.80E+00	6.05E-01	44	-2.61E-08	1.70321E-09	-3.27E-03	0.97718	0.02282	14.5595243

Fig. C.2: Sample of predicted results from hydrodynamic model up the axial height of CFB riser.

Table C.5: Predicted and experimental solid fraction at riser height of 2.55 m above the distribution plate. Data was used in Fig. 4.6. Decay constant a_d was calculated from Eq. (4.13) with K_d = 2.5. The voidage at infinity (ε_∞) was estimated from Eq. (4.23) and the dense zone voidage (ε_{dz}) from Eq. (4.2). Experimental conditions: Q_{ls}=5m^3/h; Q_{sec}=171m^3/h

Primary airflow rate, Q_{pri} (m^3/h)	Exp. solid fraction ($\times 10^{-4}$)	Predicted solid fraction ($\times 10^{-4}$)
32	0.40	0.34
53	0.73	0.76
75	2.20	1.75
96	4.25	3.91

Table C.6: Corresponding measurement points and observed operating conditions for Fig. 5.5

Primary airflow rate, Q_{pri} (m^3/h)	BFB airflow rate, Q_{BFB}	Observed condition
32	54	No chute bypass.
32	96	No chute bypass.
54	76	No chute bypass.
76	54	Chute bypass.
76	76	No chute bypass.
96	96	No Chute bypass.
96	76	Chute bypass.

C.2 Phase II

C.2.1 Operational Map for DFB

The corresponding measurement points and the observed operating conditions for deriving Fig. 3.3 are shown in Table C.6.

C.2.2 Pressure Drop

Table C.7 shows the time-averaged pressure drops at various locations in Phase II (DFB) at different chute and BFB airflow rates while the corresponding standard deviations for the pressure drops are given in Table C.8. The data was used to generate Figs. 5.6, 5.7, 5.8, 5.10

Table C.7: Pressure drop across various locations for Phase II (DFB). Q_{pri} 54 m^3/h; Q_{ch} 5 m^3/h; Q_{ls} 5 m^3/h; Q_{sec} 324 m^3/h. The data was sampled from Figs. 5.6, 5.7, 5.8, 5.10

Chute airflow rate, Q_{ch} (m^3/h)	BFB airflow rate, Q_{BFB} (m^3/h)	Chute ΔP_{ch} (kPa)	BFB, ΔP_{BFB} (kPa)	Riser upper section, ΔP_{ur} (Pa)	Riser bottom section, ΔP_{br} (Pa)
0	54	0.02	1.33	36.20	835.46
0	76	0.12	1.24	106.35	2347.43
5	54	0.06	1.03	77.90	1887.05
5	76	0.39	1.06	125.84	2413.58

Table C.8: Corresponding standard deviation (SD) for pressure drop across various locations for Phase II (DFB). Q_{pri} 54 m^3/h; Q_{ch} 5 m^3/h; Q_{ls} 5 m^3/h; Q_{sec} 324 m^3/h. The data was sampled from Figs. 5.6, 5.7, 5.8, 5.10

Chute airflow rate, Q_{ch} (m^3/h)	BFB airflow rate, Q_{BFB} (m^3/h)	Chute ΔP_{ch} (kPa)	BFB, ΔP_{BFB} (kPa)	Riser upper section, ΔP_{ur} (Pa)	Riser bottom section, ΔP_{br} (Pa)
0	54	0.02	0.15	6.04	156.13
0	76	0.02	0.04	14.59	100.05
5	54	0.01	0.06	6.82	86.81
5	76	0.06	0.05	12.54	109.46

Table C.9: Pressure drop across various locations for Phase II (DFB) during binary mixture experiments. Q_{pri} 54 m^3/h; Q_{BFB} 76 m^3/h; Q_{ch} 5 m^3/h; Q_{ls} 5 m^3/h; Q_{sec} 324 m^3/h. Data was used in Figs. 5.12, 5.13, 5.15, and 5.16.

MDPE pellet size (μm)	Mass of MDPE (kg)	Chute, ΔP_{ch} (kPa)	BFB, ΔP_{BFB} (kPa)	Riser bottom section, ΔP_{br} (Pa)	Riser upper section, ΔP_{ur} (Pa)	SD, ΔP_{ch} (kPa)	SD, ΔP_{BFB} (kPa)	SD, ΔP_{br} (Pa)	SD, ΔP_{ur} (Pa)
370	0	0.45	0.98	2394	151	0.15	0.06	124	6
370	2	0.99	1.76	2316	148	0.03	0.08	87	11
1750	0	0.43	1.09	2524	148	0.08	0.03	78	15
1750	2	0.99	1.74	1947	127	0.06	0.11	49	15

C.2.3 Binary Mixture Experiments

Table C.9 shows the time-averaged pressure drop at various locations in Phase II cold model (DFB) with the addition of two different sizes of MDPE pellets into the copper bed material. The corresponding standard deviation is also shown.

Appendix D

Additional Information on CFD Modelling

D.1 Additional Results on the CFB Cyclone Separator

Figs. D.1 and D.2 shows a typical normalized residual plot for the continuity and momentum equations for the base case and cold model cyclone simulations. It can be seen that the normalized residuals fluctuate at a level between 1×10^{-5} to 6×10^{-5}.

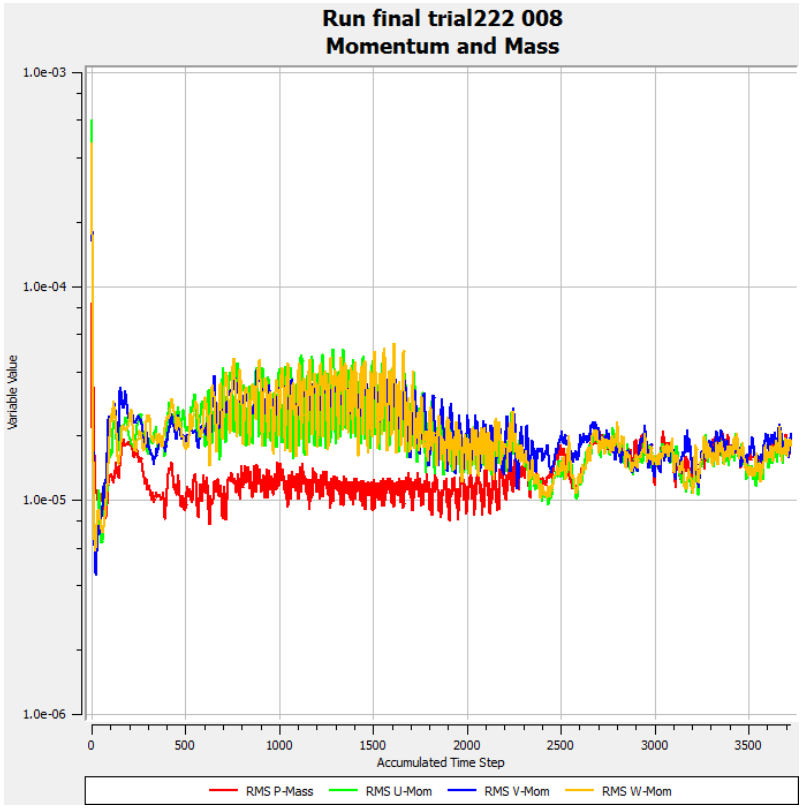

Fig. D.1: Normalized residual plot for base case simulation with SSG-RSM as turbulence model, 2.7×10^{6} mesh elements, time step of $5\times\ 10^{-4}$ s, high resolution scheme for advection terms, and second order backward differencing scheme for the transient terms.

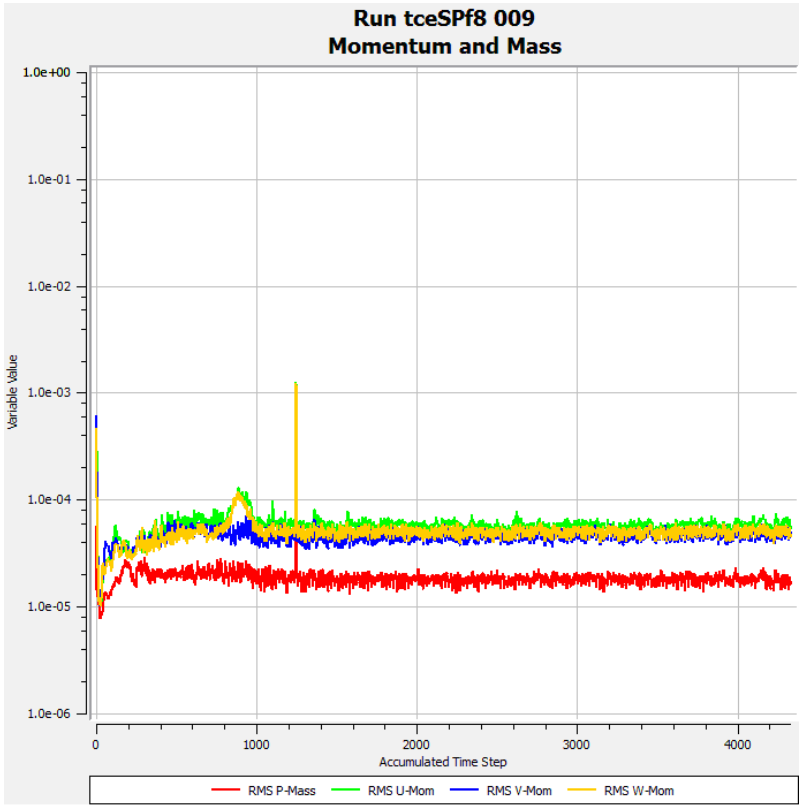

Fig. D.2: Typical residual plot for simulation of CFB cyclone separator with RSM as turbulence model, 3.2×10^6 mesh elements, time step of 5×10^{-4}s, one-way coupling with Lagrangian model for particle transport modelling, high resolution scheme for advection terms, and second order backward differencing scheme for the transient terms.